

Evaluating EAMv2 simulated stratiform mixed-phase cloud properties at Northern and Southern high latitudes against ARM measurements

Meng Zhang¹, Shaocheng Xie², Xiaohong Liu³, Damao Zhang⁴, Wuyin Lin⁵, Kai Zhang⁶, Jean-Christophe Golaz⁷, Xue Zheng⁷, and Yuying Zhang⁸

¹Lawrence Livermore National Laboratory

²LLNL

³Texas A&M University

⁴Pacific Northwest National Laboratory

⁵Brookhaven National Laboratory (DOE)

⁶Pacific Northwest National Laboratory (DOE)

⁷Lawrence Livermore National Laboratory (DOE)

⁸Lawrence Livermore National Lab

December 15, 2022

Abstract

This study evaluates high-latitude stratiform mixed-phase clouds (SMPC) in the atmosphere model of the newly released Energy Exascale Earth System Model version 2 (EAMv2) by utilizing one-year-long ground-based remote sensing measurements from the U.S. Department of Energy Atmospheric Radiation and Measurement (ARM) Program. A nudging approach is applied to model simulations for a better comparison with the ARM observations. Observed and modeled SMPCs are collocated to evaluate their macro- and microphysical properties at the ARM North Slope of Alaska (NSA) site in the Arctic and the McMurdo (AWR) site in the Antarctic. We found that EAMv2 overestimates (underestimates) SMPC frequency of occurrence at the NSA (AWR) site nearly all year round. However, the model captures the observed larger cloud frequency of occurrence at the NSA site. For collocated SMPCs, the annual statistics of observed cloud macrophysics are generally reproduced at the NSA site, while at the AWR site, there are larger biases. Compared to the AWR site, the lower cloud boundaries and the warmer cloud top temperature observed at NSA are well simulated. On the other hand, simulated cloud phases are substantially biased at each location. The model largely overestimates liquid water path at NSA, whereas it is frequently underestimated at AWR. Meanwhile, the simulated ice water path is underestimated at NSA, but at AWR, it is comparable to observations. As a result, the observed hemispheric difference in cloud phase partitioning is misrepresented in EAMv2. This study implies that continuous improvement in cloud microphysics is needed for high-latitude mixed-phase clouds.

1 **Evaluating EAMv2 simulated stratiform mixed-phase cloud properties at Northern and**
2 **Southern high latitudes against ARM measurements**

3
4 Meng Zhang¹, Shaocheng Xie¹, Xiaohong Liu², Damao Zhang³, Wuyin Lin⁴, Kai Zhang³,
5 Jean-Christophe Golaz¹, Xue Zheng¹, Yuying Zhang¹

6
7 ¹ Lawrence Livermore National Laboratory, Livermore, CA, USA

8 ² Department of Atmospheric Sciences, Texas A&M University, College Station, Texas, USA

9 ³ Pacific Northwest National Laboratory, Richland, WA, USA

10 ⁴ Brookhaven National Laboratory, Upton, NY, USA

11
12 Corresponding author: Meng Zhang, zhang55@llnl.gov

13
14
15 Key points:

- 16 • Stratiform mixed-phase clouds simulated from nudged EAMv2 simulation are evaluated
17 with ARM ground-based remote sensing retrievals.
- 18 • Cloud macrophysics and their hemispheric difference are better simulated than cloud
19 phase.
- 20 • Cloud phase is largely biased, with underestimated ice water path at the NSA site and
21 underestimated liquid water path at the AWR site.
- 22
23

24
25
26
27
28
29
30
31
32
33
34
35
36
37
38
39
40
41
42
43
44
45
46

Abstract

This study evaluates high-latitude stratiform mixed-phase clouds (SMPC) in the atmosphere model of the newly released Energy Exascale Earth System Model version 2 (EAMv2) by utilizing one-year-long ground-based remote sensing measurements from the U.S. Department of Energy Atmospheric Radiation and Measurement (ARM) Program. A nudging approach is applied to model simulations for a better comparison with the ARM observations. Observed and modeled SMPCs are collocated to evaluate their macro- and microphysical properties at the ARM North Slope of Alaska (NSA) site in the Arctic and the McMurdo (AWR) site in the Antarctic. We found that EAMv2 overestimates (underestimates) SMPC frequency of occurrence at the NSA (AWR) site nearly all year round. However, the model captures the observed larger cloud frequency of occurrence at the NSA site. For collocated SMPCs, the annual statistics of observed cloud macrophysics are generally reproduced at the NSA site, while at the AWR site, there are larger biases. Compared to the AWR site, the lower cloud boundaries and the warmer cloud top temperature observed at NSA are well simulated. On the other hand, simulated cloud phases are substantially biased at each location. The model largely overestimates liquid water path at NSA, whereas it is frequently underestimated at AWR. Meanwhile, the simulated ice water path is underestimated at NSA, but at AWR, it is comparable to observations. As a result, the observed hemispheric difference in cloud phase partitioning is misrepresented in EAMv2. This study implies that continuous improvement in cloud microphysics is needed for high-latitude mixed-phase clouds.

47 **1. Introduction**

48 For decades, mixed-phase clouds that consist of both liquid droplets and ice crystals at
49 temperatures between 0 and -40°C have been ubiquitously observed at high latitudes in both
50 hemispheres (Korolev et al., 2017; McFarquar et al., 2021; Shupe et al., 2011; Zhang et al.,
51 2018). Mixed-phase clouds can impact the regional and global climate by modulating the energy
52 budget at the surface and the top of the atmosphere. Partitioning of cloud liquid and ice is critical
53 for the radiative effect of mixed-phase clouds, which is manifested by the significant difference
54 in optical properties between liquid droplets and ice particles (Curry et al., 1996; Sun & Shine,
55 1994; 1995; Gregory & Morris, 1996). By parameterizing the distinct optical properties of liquid
56 and ice water in general circulation models (GCMs), the simulated cloud phase has been
57 demonstrated to be one of the key factors influencing the predicted future climate (Lohmann &
58 Neubauer, 2018; McCoy et al., 2015). Tan et al. (2016) constrained the model simulated cloud
59 phase using satellite observations to correct the low bias of supercooled liquid fraction (SLF) in
60 the Community Atmosphere Model version 5.1 (CAM5.1), which results in an increase of the
61 equilibrium climate sensitivity (ECS) by 1.3°C compared to the default model. The higher ECS
62 mainly results from the reduced negative cloud phase feedback at high latitudes. Furthermore,
63 the magnitude of Arctic amplification is found to have a considerable sensitivity to the relative
64 abundance of cloud liquid and ice in high-latitude mixed-phase clouds (Middlemas et al., 2020;
65 Tan & Storelvmo, 2019; Tan et al., 2022).

66 However, significant uncertainties exist in the simulated cloud properties of high-latitude
67 mixed-phase clouds, including cloud phase partitioning. The challenges are mainly attributable
68 to the parameterization of unresolved subgrid-scale cloud processes and the gap in fundamental
69 process-level understanding of cloud microphysics (Morrison et al., 2020). Among a variety of

70 GCMs that participate in the Coupled Model Intercomparison Project Phase 5 and Phase 6
71 (CMIP5 and CMIP6), the model predicted cloud phase and associated cloud feedbacks are highly
72 sensitive to the treatments of cloud microphysics (McCoy et al., 2015, 2016; Zelinka et al., 2020;
73 Gettelman et al., 2019). Yip et al. (2021) evaluated the simulated cloud properties from the
74 Community Atmosphere Model version 6 (CAM6) against the remote sensing retrievals during
75 the U.S. Department of Energy (DOE) Atmospheric Radiation Measurement (ARM) West
76 Antarctic Radiation Experiment (AWARE) field campaign. They found that CAM6 largely
77 overestimates cloud fraction above and underestimates it below 3 km. Liquid phase clouds are
78 overestimated, and ice and mixed-phase clouds are underestimated when cloud fraction exceeds
79 0.6. Cloud fraction biases are found to be closely related to the biases in simulated relative
80 humidity and water vapor. Cloud ice water simulated by the U.S. DOE Energy Exascale Earth
81 System Model (E3SM) Atmosphere Model version 1 (EAMv1) was also underestimated, and
82 cloud liquid water was overestimated when compared to the Cloud-Aerosol Lidar and Infrared
83 Pathfinder Satellite Observation (CALIPSO) satellite observations (Y. Zhang et al., 2019) and
84 ARM Mixed-Phase Arctic Cloud Experiment (M-PACE) field campaign data (M. Zhang et al.,
85 2020). Compared with in situ airborne observations from the Southern Ocean Clouds, Radiation,
86 Aerosol Transport Experimental Study (SOCRATES) campaign, Yang et al. (2021) found that
87 both CAM6 and E3SMv1 overestimate cloud liquid and underestimate cloud ice occurrences at
88 temperatures colder than -20°C .

89 Due to the limitations and uncertainties in different instruments and retrieval algorithms,
90 cloud property retrievals used in model validations can vary significantly (Zhao et al., 2012).
91 McErlich et al. (2021) compared the cloud occurrence retrievals from the 2B-CLDCLASS-
92 LIDAR R05 (2BCL5) and the radar/liDAR (DARDAR) satellite products with ground-based

93 measurements during the AWARE field campaign. They found that the 2BCL5 and DARDAR
94 satellite retrievals underestimate cloud occurrence at altitudes lower than 1.5 km, while the
95 AWARE ground-based observations underestimate cloud occurrence higher than 6 km. Liu et al.
96 (2017) also showed that space-borne observations, such as the 2B-GEOPROF-lidar, detect 25%-
97 40% fewer clouds than ground-based lidar below 0.5 km. The discrepancies between satellite-
98 and ground-based retrievals of cloud occurrence are mainly attributed to the attenuation of lidar
99 or radar beams or the uncertainties in retrieval algorithms. The difference between active and
100 passive sensors also contributes to the disagreements between different satellite products. For
101 example, Villanueva et al. (2021) utilized the CALIPSO-GOCCP (GCM-Oriented Cloud Calipso
102 Product), DARDAR, and PM-L2 (MODIS, MODERate resolution Imaging Spectroradiometer,
103 and PARASOL combined product) cloud top phase products to examine the hemispheric contrast
104 in observed cloud phase. The disagreement in the retrieval of ice phase frequency is noticeable
105 among different products, which is mainly caused by the retrieval issues and the limited
106 capability of different instruments in detecting ice particles and liquid droplets. They further
107 suggested that the cloud top phase from the combination of three cloud products is more reliable
108 than individual products when estimating the cloud phase hemispheric difference. Therefore, it is
109 important to understand the uncertainties in observational datasets and, if necessary, utilize
110 different products with complementary capabilities in retrievals when applying them in the
111 model evaluation.

112 In an earlier evaluation of the high-latitude cloud phase in version 2 of the E3SM
113 atmosphere model (EAMv2), M. Zhang et al. (2022) compared model simulated cloud properties
114 from the CALIPSO simulator in EAMv2 with the CALIPSO-GOCCP product. However, like
115 other satellite retrievals, CALIPSO-GOCCP also suffers from the limited capability of detecting

116 low-level clouds and precipitation. Such limitations make the thorough evaluation of cloud
117 properties at high latitudes difficult, considering that precipitating ice is common for high-
118 latitude mixed-phase clouds. In the past years, the ARM program performed multi-year long-
119 term ground-based measurements at the North Slope of Alaska (NSA, Utqiagvik in the Arctic).
120 In 2016, comprehensive ground-based instruments were also deployed at the McMurdo station
121 (AWR, in the Antarctic) to conduct one-year-long measurements during the AWARE field
122 campaign (Lubin et al., 2020; Verlinde et al., 2016). These ARM measurements complement the
123 satellite retrievals and provide reliable and robust atmospheric states, cloud, and precipitation
124 observations at high latitudes, which have been applied in many model evaluation studies (Klein
125 et al., 2009; Ovchinnikov et al., 2014; C. Zhang., 2020).

126 This study aims to evaluate mixed-phase cloud properties from EAMv2 using ARM
127 retrievals at the NSA and AWR sites. Previous studies showed that cloud properties retrieved at
128 the NSA and AWR can largely differ, especially for cloud occurrence, cloud height, and cloud
129 thickness (Lubin et al., 2020; Silber et al., 2018). D. Zhang et al. (2019) illustrated that stratiform
130 mixed-phase clouds (SMPCs, hereafter) at the AWR site can have larger SLF than those at the
131 NSA site for a given temperature between -24°C and -14°C . The larger SLF in the Antarctic is
132 mainly because of the lower ice water path (IWP) compared to the Arctic, while a comparable
133 liquid water path (LWP) is found at that temperature range. Thus, one emphasis of this study is
134 to evaluate whether EAMv2 can simulate the observed hemispheric difference in mixed-phase
135 cloud properties shown in the ARM observations. A novel comparison method is applied in this
136 study to focus only on high-latitude SMPCs. The merit of this method is that the target SMPCs
137 are defined consistently in the model simulation and ARM observation.

138 The paper is organized as follows: section 2 describes the EAMv2 model and model
139 experiments. Section 3 introduces the ARM observational data and retrievals of analyzed SMPC
140 properties. An innovative comparison approach between EAMv2 and ARM data is presented in
141 section 4. Section 5 discusses the comparison results between modeled and observed SMPCs,
142 and the conclusions are summarized in section 6.

143

144 **2. Model Description and Experiments**

145 **2.1. EAMv2 Model**

146 The recently released EAMv2 model is evaluated in this study. Different from EAMv1
147 (Rasch et al., 2019, Xie et al., 2018), EAMv2 runs on a spectral finite element dynamical core
148 with a semi-Lagrangian passive tracer transport method (Bradley et al., 2021). As introduced by
149 Hannah et al. (2021), the parameterized physics and dynamics use separate grids. The dynamics
150 grid has an average grid spacing of 110 km, while the physics grid has an average grid spacing of
151 165 km. In the vertical, it keeps the same 72 vertical layers with a model top at ~ 0.1 hPa as
152 EAMv1. For atmospheric physics, the major changes include a new convective trigger described
153 in Xie et al. (2019) incorporated in the deep convection scheme (Zhang & McFarlane, 1995) to
154 improve the simulation of precipitation and its diurnal cycle. A convective gustiness scheme for
155 subgrid gustiness enhancement is incorporated in EAMv2 to improve the surface exchanges of
156 heat, moisture, and momentum and the representation of tropical clouds and precipitation
157 (Harrop et al., 2018; Ma et al., 2022). EAMv2 also updates the linearized chemistry for
158 stratospheric ozone (Tang et al., 2021) to preserve the sharp cross-tropopause gradient and
159 improve the stratosphere-troposphere exchange flux of ozone. The parameterizations for other
160 processes remain the same as those used in EAMv1. They include the Cloud Layers Unified By

161 Binormals (CLUBB) parameterization (Golaz et al., 2002; Larson, 2017) for subgrid turbulent
162 transport and cloud macrophysics, the second version of Morrison and Gettelman (MG2) cloud
163 microphysics scheme (Gettelman & Morrison, 2014), the Classical Nucleation Theory (CNT)
164 based heterogeneous ice nucleation scheme for mixed-phase clouds (Hoose et al., 2010; Wang et
165 al., 2014), and the four-mode version of the Modal Aerosol Module (MAM4) (Liu et al., 2012,
166 2016; Wang et al., 2020). Following Ma et al. (2022), several tuning parameters in cloud
167 microphysics, CLUBB, and deep convection are recalibrated to improve the cloud and
168 precipitation simulations. More details about the EAMv2 model can be found in the overview
169 paper of Golaz et al. (2022).

170

171 **2.2. Model Experiments**

172 The EAMv2 simulations are run with the nudging approach following Sun et al. (2019).
173 The nudging helps to constrain the simulated large-scale circulation with reanalysis data so that
174 the synoptic weather events observed during ARM field campaigns can be well captured by
175 nudged simulations (Zhang et al., 2014). With more realistic state variables in our model
176 simulation, we can thus collocate simulated clouds to the measured clouds and then examine the
177 differences between the model and observation at the NSA and AWR sites.

178 In this study, the horizontal wind (U, V) and temperature (T) fields are nudged toward
179 ERA-Interim reanalysis data for 2016 starting from 1st November 2015, with a nudging
180 relaxation time scale of 6 hours. Sea surface temperature and sea ice are prescribed with
181 observed data. Model simulations of the first two months are discarded as the spin-up, and model
182 results for 2016 are evaluated against the ARM SMPC retrievals. EAMv2 results are output
183 every 30 minutes. The model grids that are closest to the NSA site (71°19'22.8" N, 156°36'54"

184 W) and AWR site (77°50'47" S, 166°40'06" E) are used for analysis. Note that the chosen model
185 grid near the NSA represents the coastal environment, and the grid near the AWR is over the
186 ocean. The influence of land and ocean grids on simulated cloud properties has been examined
187 by comparing neighboring grids points, and it has minimal impact on our evaluations (not
188 shown).

189

190 **3. ARM Observations**

191 Over the past three decades, the U.S. DOE ARM program has established long-term
192 observations of cloud, radiation, and large-scale environment at several ARM observation sites.
193 This study utilizes the ARM ground-based remote sensing data at the NSA and AWR sites in
194 2016 to evaluate EAMv2 simulated mixed-phase cloud properties. During that year, the ARM
195 program launched the AWARE field campaign over the West Antarctic Ice Sheet (WAIS) to
196 understand the rapid climate change in the remote Antarctic region. The second ARM Mobile
197 Facility (AMF2), including cloud radar, high spectral resolution lidar, laser ceilometer,
198 microwave radiometer, etc., was deployed at the AWR site from 1 December 2015 to 31
199 December 2016. Measurements with the same suite of instruments were also available at the
200 NSA site in 2016. This allows us to compare the simulated cloud properties between the Arctic
201 and Antarctic sites to examine if the model can reproduce the observed hemispheric differences
202 in cloud properties for similar types of mixed-phase clouds. Detailed descriptions of instruments,
203 meteorological conditions, and summaries of cloud and aerosol measurements at the NSA and
204 AWR sites are presented in Verlinde et al. (2016) and Lubin et al. (2020), respectively.

205 For observed SMPCs, we use: (1) the high spectral resolution lidar (HSRL) and Ka-band
206 ARM zenith radar (KAZR) measurements in cloud structure detections and cloud property

207 retrievals; (2) the ARM INTERPSONDE value-added product (VAP,
208 <https://www.arm.gov/capabilities/vaps/interpsonde>) for atmosphere environmental conditions
209 including pressure, temperature, water vapor, and relative humidity; and (3) the ARM MWRRET
210 VAP (<https://www.arm.gov/capabilities/vaps/mwrret>) for cloud LWP. Stratiform mixed-phase
211 identification and cloud macrophysical and microphysical property retrievals are described in
212 detail by D. Zhang et al. (2019, DZ19 hereafter). In short, the liquid-dominated layer at the cloud
213 top is determined from the HSRL backscatter coefficient gradient and depolarization profiles,
214 while the ice virga is detected by the KAZR reflectivity (Z_e). Cloud top and cloud base heights
215 and associated cloud layer temperature can then be derived. For ice phase microphysical
216 properties, the ice water content (IWC) profile is retrieved using the IWC-Z (radar reflectivity
217 factor) and temperature relationships following Hogan et al. (2006). The IWP is derived by
218 integrating IWC from the cloud base to the cloud top. For liquid phase microphysical properties,
219 LWP is obtained from the ARM MWRRET VAP.

220 Note that SMPC boundaries determined with the KAZR and HSRL measurements alone
221 are dominated by liquid water in DZ19. In particular, the identified cloud base is the base of
222 liquid dominated layer. However, with precipitating ice hydrometeors frequently observed in
223 high-latitude SMPCs (Morrison et al., 2012), such cloud boundaries are not accurate, and thus
224 they are not used in this study. Instead, the retrieval of the vertical distribution of cloud
225 hydrometeors based on the combined measurements of cloud radar, lidar, and laser ceilometer
226 from the Active Remote Sensing of Clouds (ARSCL) algorithm (Clothiaux et al., 2000) is used
227 in the evaluation since the ARSCL algorithm can more accurately determine the cloud base with
228 precipitating ice included (Clothiaux et al., 2000). Meanwhile, the model calculated cloud
229 vertical distribution also contains layers of ice hydrometeors, consistent with the ARSCL cloud

230 boundary. Therefore, we use the ARSCL retrievals of identified SMPCs to evaluate modeled
 231 cloud boundary properties. Given the common nature of liquid-dominated cloud top in high-
 232 latitude SMPCs, the cloud top retrieved from the ARSCL algorithm and the cloud top of liquid-
 233 dominated layer in DZ19 are overall comparable with each other (not shown). Furthermore,
 234 because cloud properties can largely influence the surface energy budget, surface radiative fluxes
 235 in the ARM Best Estimate product (ARMBE, Xie et al., 2010) are also used to evaluate modeled
 236 cloud radiative effects at the NSA and AWR sites. Table 1 summarizes all the observational data
 237 used in the current model evaluation.

238

239 Table 1. *Summary of Cloud Properties Derived from ARM Measurements.*

Cloud Property	Instrument and Retrieval Method
Cloud top height (CTH)	Cloud boundaries detected with KAZR, MPL, and laser ceilometer from the Active Remote Sensing of Clouds Products using KAZR (KAZRARSCl) VAP (https://www.arm.gov/capabilities/vaps/kazrarscl)
Cloud base height (CBH)	
Cloud thickness (THK)	
Cloud top temperature (CTT)	Using temperature profiles from the ARM INTERPSONDE VAP and KAZRARSCl CTH
Liquid water path (LWP)	From the ARM MWRRET VAP
Ice water path (IWP)	Integrating ice water content (IWC) retrieved using the IWC-Z-T relationship from CBH to CTH (Hogan et al., 2006)
Surface radiative fluxes	From ARMBE VAP (Xie et al., 2010)

240

241

242 4. Evaluation Method

243 An innovative approach is utilized in this study to evaluate EAMv2 simulated cloud
 244 properties against ARM ground-based remote sensing retrievals. The idea behind this approach

245 is to select model simulated clouds with the similar characteristics to those retrieved in DZ19. By
246 doing so, we can consistently compare the properties of the same type of SMPC and thus avoid
247 error and ambiguity in cloud evaluation due to the inconsistent definitions between the model
248 and observation. As SMPCs are prevalent in the Arctic and Antarctic regions and are the focus of
249 DZ19, our sampling also targets SMPCs in the model simulation. We define the target SMPCs
250 by the following criteria: (1) Simulated cloud fraction is greater than 5% to define cloudy
251 conditions; (2) Cloud top temperature is within 0 – -40°C range to ensure a supercooled
252 environment that is suitable for mixed-phase clouds; and (3) If multi-layer clouds exist and also
253 the distance between multiple cloud layers is greater than 2 km, we assume the seeding effect
254 does not affect the lower cloud layer. Thus, we keep the lower cloud layer to exclude the seeding
255 effect from the upper cloud layers. Note that the third criterion is the same as that used in DZ19.
256 Such a criterion not only increases the data amount of SMPC compared to that of single-layer
257 mixed-phase clouds but also keeps the relatively simple structures in the examined clouds, which
258 increases the statistical significance of our data analysis. Although the target cloud samples share
259 similar definitions between the model and observation, inconsistencies cannot be removed
260 entirely in the comparison. For example, given the high temporal resolution (30 s) of ground-
261 based remote sensing instruments (i.e., KAZR and HSRL), stratiform cloud systems are
262 identified if cloud top heights show little variability with standard deviations smaller than 300 m.
263 However, the same criterion is inapplicable to model outputs with the 30-minute time step.
264 Therefore, we assume that the simulated grid-mean clouds are all stratiform if they meet the
265 aforementioned criteria. Meanwhile, we consider vertically continuous cloud layers as the same
266 cloud system in the model. The calculation of cloud properties is then for cloud systems
267 extending over several model vertical layers. We also note that the number of defined SMPC

268 from EAMv2 varies by about 5% if we modify the chosen thresholds of cloud fraction (i.e., 5%
269 changing to 1% or 10%) and the distance between multiple cloud layers (i.e., 2 km changing to
270 1.5 km or 3 km) used in the sampling, which does not significantly affect the evaluation.

271 To further evaluate the SMPC properties in EAMv2, the 30-second retrievals of DZ19 are
272 averaged to the one-hour temporal resolution. The choice of hourly resolution is for consistency
273 with the highest temporal resolution available in the ARMBE product. We also tested the
274 temporal resolution of 30 minutes for ARM data and compared it with the model results. We
275 found that the SMPC data sampling is nearly doubled compared to the one-hour resolution, but
276 the observed cloud properties are generally insensitive to the temporal resolution change.
277 Therefore, the case-by-case examinations of cloud structures and microphysical properties are
278 performed using hourly observations and model outputs (i.e., averaged from 30-minute outputs).

279 Since the selected SMPC samples from the model and observation do not necessarily
280 occur at the same time in 2016, a collocation approach is used to further determine the times
281 when both the model and observation have SMPCs. We collocate the model and observation by
282 comparing the time series of hourly simulated and observed clouds. If SMPCs appear in both the
283 model and observation, we consider the SMPC in this hour is collocated. The collocation allows
284 a case-by-case comparison of SMPC properties between the model and observation. The
285 collocation also links the simulated cloud radiative properties to other ARM measurements for
286 each pair of model and observational data, which benefits the examination of the impact of
287 biased cloud properties on cloud radiative effects. This approach is applied to both the NSA and
288 AWR sites for evaluation purposes.

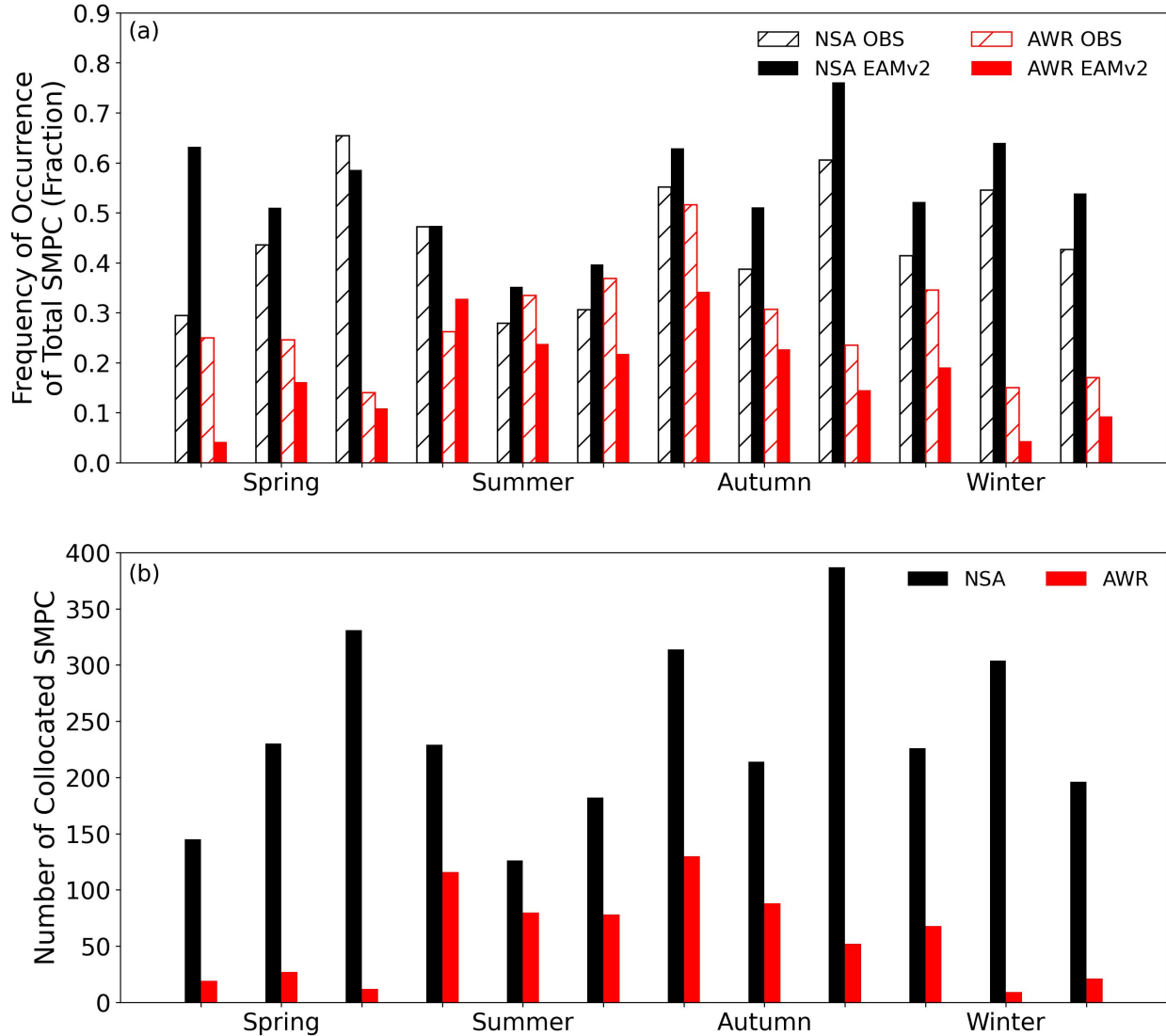
289

290 **5. Results**

291 **5.1. Cloud Occurrence**

292 We first examine the general model behavior in simulating SMPCs during 2016. Figure 1
293 compares the frequency of occurrence of total SMPC samples in EAMv2 with DZ19 at NSA and
294 AWR sites. The monthly frequency of occurrence of SMPC is grouped into four seasons
295 according to their respective months so that the monthly comparison is in phase between two
296 hemispheres. The SMPC frequency of occurrence is calculated by dividing the number of hourly
297 data containing SMPC samples during a month by the number of total hours (i.e., all-sky
298 conditions that include both clear and cloudy skies) during the same month. In the Arctic,
299 observed SMPC exhibits the largest frequency of occurrence in late boreal spring and the lowest
300 SMPC occurrence in boreal summer. A relatively large frequency of occurrence is observed in
301 boreal autumn and winter. Throughout the year, the observed frequency of occurrence of SMPC
302 at the AWR site is substantially lower than at the NSA site, except for summertime. Seasonally,
303 however, SMPCs occur more frequently during the warm season (austral summer and autumn),
304 peaking in early austral autumn at the AWR, while the occurrences become less frequent in
305 austral winter and spring.

306



307

308 Figure 1. Comparison of seasonal frequency of occurrence of total stratiform mixed-phase clouds

309 (SMPC) between EAMv2 simulation and ARM ground-based retrievals at NSA and AWR sites

310 (a). The seasonal variation of the number of collocated SMPCs is shown in (b).

311

312 Compared to the observations, although the model generally simulates the seasonal
 313 variations of the frequency of occurrence of SMPC at both sites, the frequency of occurrence of
 314 EAMv2 simulated SMPC is clearly biased in individual months, with noticeable differences
 315 between the two polar locations. In the Arctic, the model overestimates the frequency of

316 occurrence from boreal mid-summer to mid-spring and underestimates cloud occurrences for the
317 rest of the months. Conversely, the SMPC frequency of occurrence at AWR is largely
318 underestimated across the year except in early austral summer. The observed cold versus warm
319 seasonal contrast is largely captured at AWR. The excessive cloud occurrences in the Arctic and
320 the deficit in cloud occurrences in the Antarctic are consistent with M. Zhang et al. (2022). They
321 also found that EAMv2 overestimates supercooled liquid clouds in the Arctic and substantially
322 underestimates total cloud cover over Antarctica in comparison with the CALIPSO-GOCCP
323 data. It is encouraging that EAMv2 can reasonably simulate the larger frequency of occurrences
324 of total SMPC in the Arctic than in the Antarctic, which is consistent with DZ19. Note that the
325 retrieved frequency of occurrence in Figure 1 represents the largest possible SMPC occurrence
326 because we count the SMPC occurrence in each one-hour window as long as SMPC appears
327 once when degrading the 30-second temporal resolution to one hour. The retrieved frequency of
328 occurrence is largely reduced (by ~28% at NSA and ~50% at AWR annually) if we consider
329 SMPCs to last at least 30 minutes in each one-hour window. However, with a relatively coarse
330 temporal resolution of the hourly data, we keep the largest possible SMPC occurrences to ensure
331 sufficient data in the statistical analysis in the following sections. Regardless of the sensitivity of
332 observed SMPC occurrence to temporal resolutions, the seasonal variation of SMPC frequency
333 of occurrence is not affected at different temporal resolutions (not shown).

334 With the model's capability to capture sufficient occurrences of SMPC at the NSA and
335 AWR sites, modeled SMPCs can be collocated with the observed SMPCs in DZ19. The
336 collocation approach, which was introduced in Section 4, allows the case-by-case evaluations of
337 modeled SMPC properties in two hemispheres at high latitudes. Figure 1b shows the monthly
338 amount of collocated SMPCs in EAMv2. Generally, the number of collocated SMPCs follows

339 the seasonal variation of frequency of occurrence of total SMPCs. For example, more collocated
340 SMPCs appear in boreal late spring and autumn at the NSA site when more SMPCs are
341 observed. Collocated SMPCs also occur more frequently in austral summer and autumn at the
342 AWR site. Similar to the difference in the frequency of occurrence of total SMPCs between NSA
343 and AWR, the number of collocated SMPCs also shows a noticeable hemispheric difference
344 throughout the year. In total, the number of collocated SMPCs is 2888 and 700 at NSA and
345 AWR, respectively, accounting for ~60% and ~45% of total SMPC samples in the model and
346 ~74% and ~29% of SMPC samples in the observation. Although the percentage of collocated
347 SMPCs to total SMPC data is relatively low at the AWR site, the comparison of cloud property
348 statistics between collocated and non-collocated SMPCs indicates that the collocated SMPC data
349 are generally representative of the annual statistics of total SMPCs observed at two sites (not
350 shown). In the following analysis, we will focus on the collocated SMPCs to evaluate simulated
351 cloud properties at two high-latitude ARM locations.

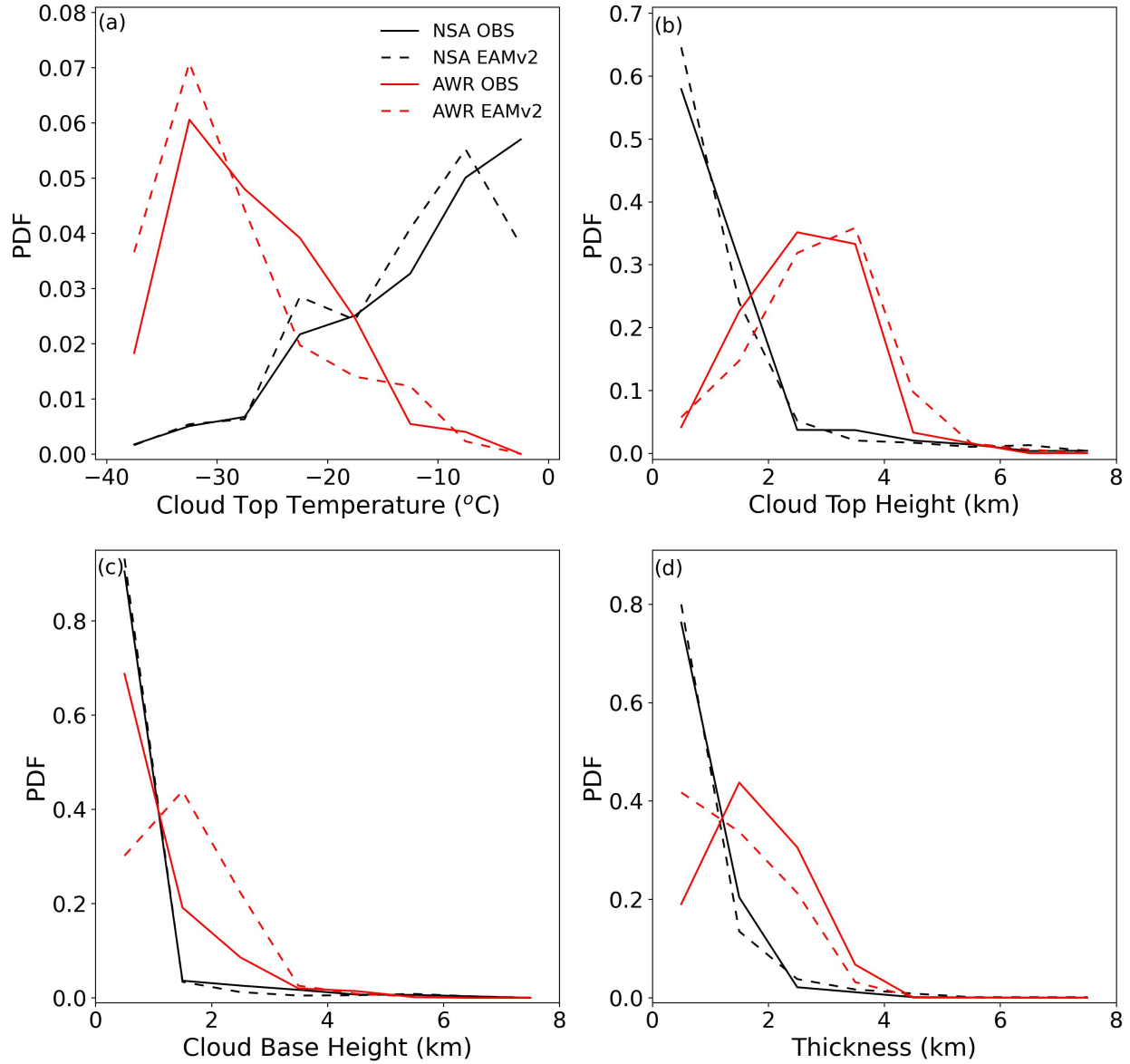
352

353 **5.2. Cloud Macrophysical Properties**

354 Figure 2 compares the probability density function (PDF) of cloud macrophysical
355 properties of collocated SMPCs between EAMv2 and ARM retrievals. The PDF comparison
356 provides an overall evaluation of the modeled cloud top temperature (CTT), cloud top height
357 (CTH), cloud base height (CBH), and cloud thickness (THK) of all collocated SMPCs at the
358 NSA and AWR sites across the year. In EAMv2, cloud top and cloud base are determined as the
359 highest and lowest model levels with cloud fractions greater than 5%. THK is the difference
360 between CTH and CBH, and CTT is the simulated temperature of the model level where the
361 cloud top is located. As introduced in Section 3, the ARM retrieved cloud top and cloud base are

362 based on the ARSCL algorithm. The retrieved CTT is the temperature of liquid-dominated layer
 363 at cloud top.

364



365

366 Figure 2. PDFs of observed and modeled cloud top temperature (CTT, a), cloud top height
 367 (CTH, b), cloud base height (CBH, c), and cloud thickness (THK, d) for collocated cloud data
 368 between EAMv2 (dashed line) and ARM retrievals (solid line). Black color represents the NSA
 369 site and red color represents the AWR site.

370

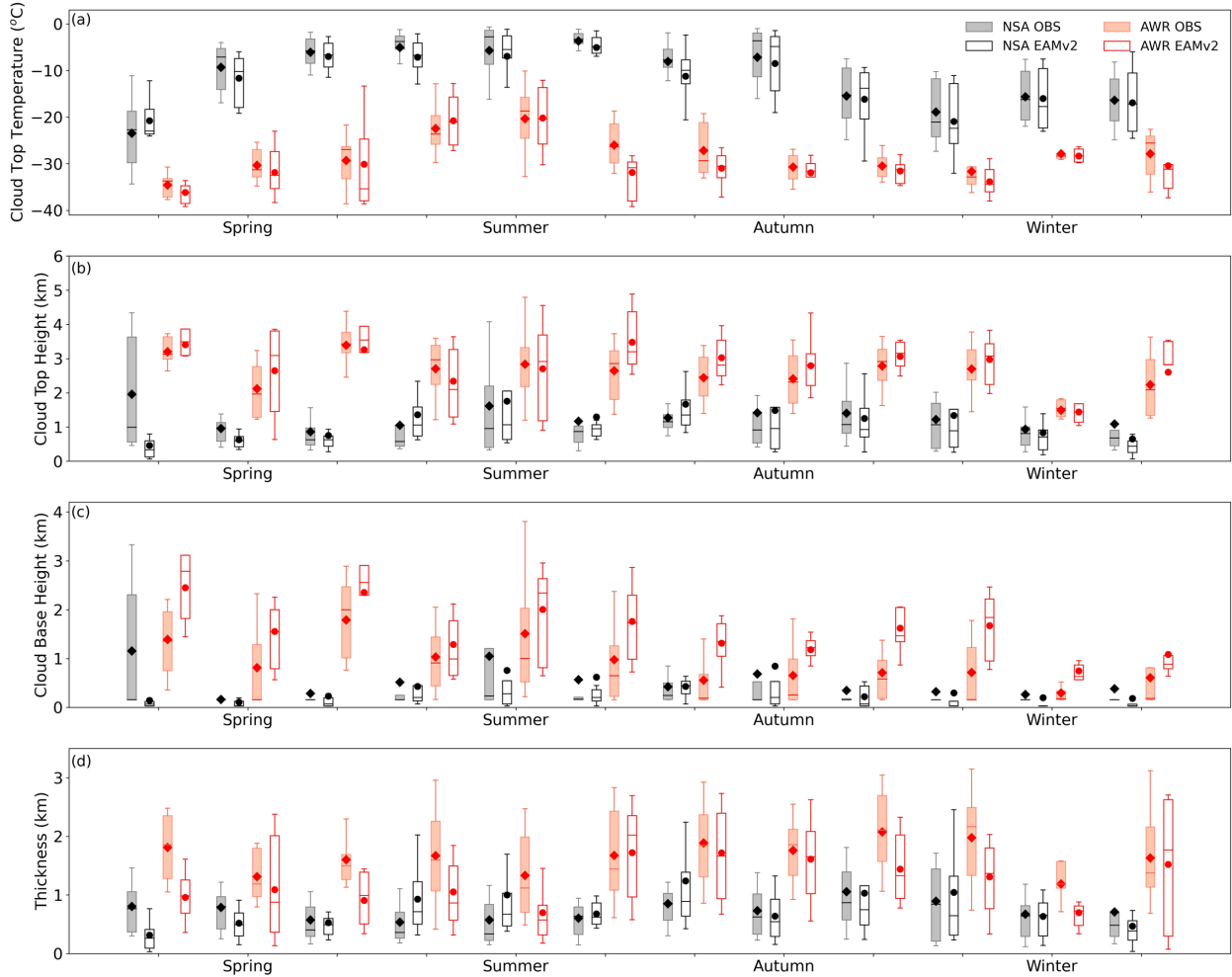
371 In general, EAMv2 simulated SMPCs resemble the features of the annual statistics of
372 cloud properties in the observation, especially for their PDF distributions (Figure 2). For
373 example, the PDF of observed CTT increases monotonically with increasing temperatures at the
374 NSA site, suggesting that most Arctic SMPCs are formed under relatively warm conditions. The
375 monotonic feature at the NSA is reproduced by EAMv2 for CTT colder than -10°C , although the
376 modeled CTT PDF fails to increase further for temperatures warmer than -8°C . On the other
377 hand, observed SMPCs at the AWR site have the largest probability of CTT around -32°C . The
378 peak of observed CTT PDF at the AWR is also captured by EAMv2. Thus, the hemispheric
379 difference in CTT PDF between the NSA and AWR sites is reasonably shown in EAMv2.
380 However, the model underestimates the probabilities for CTT warmer than -8°C and
381 overestimates the probabilities for CTT between -8°C and -25°C at the NSA, and more
382 occurrences of CTT colder than -28°C and fewer occurrences between -15°C and -28°C are
383 simulated at the AWR.

384 For retrieved CTH, CBH, and THK in collocated SMPCs at the NSA site, the PDFs
385 decrease monotonically with increasing cloud boundary heights and thickness, with the
386 maximum probabilities occurring below ~ 1 km for CTH and CBH and thinner than 1 km for
387 THK. It is evident from Figure 2 that EAMv2 reasonably reproduces the PDFs of CTH, CBH,
388 and THK for collocated SMPC cases at the NSA site. The comparable PDFs in cloud boundaries
389 suggest that when large-scale states (i.e., U, V, and T) are constrained by the reanalysis data,
390 EAMv2 has the capability to simulate the annual statistics of these macrophysical cloud
391 properties in the Arctic. Figure 2b shows that the CTH PDF of observed SMPCs at the AWR has
392 a plateau between 2.5 and 4 km. The occurrences of CTH higher than 2 km are substantially

393 greater than those for the Arctic SMPCs. The collocated SMPCs from EAMv2 also exhibit a
 394 similar plateau in their CTH PDF, while the modeled PDF shifts toward higher CTHs. However,
 395 PDF biases are significant for CBH and THK at the AWR site. While the probabilities of
 396 observed CBH decrease monotonically with increasing heights, EAMv2 simulates a peak at
 397 about 1.6 km. Instead of a peak in the observed THK PDF near 1.8 km, the model features a
 398 monotonic decrease in the THK PDF. The model overestimates the occurrences of CBH higher
 399 than 1 km and underestimates the occurrences of THK larger than 1.2 km at the AWR.
 400 Nevertheless, regarding the cloud property difference between the two sites, the statistically
 401 higher cloud base and cloud top and the thicker cloud layer in observed Antarctic SMPCs are
 402 simulated by EAMv2 as compared to the Arctic SMPCs.

403 The monthly statistics of modeled cloud macrophysical properties for collocated SMPCs
 404 are evaluated in Figure 3. Figure 3a shows that the observed CTT of collocated SMPCs at both
 405 polar sites is warmer in summer than in winter. Compared with the retrieved CTT, cold bias as
 406 indicated by the colder mean CTT is simulated from the model at the NSA site from boreal mid-
 407 spring to early winter. A similar cold bias is also simulated at the AWR site except for early to
 408 mid-summer. These cold biases largely contribute to the overestimation of probabilities of
 409 modeled CTT between -8°C and -25°C at the NSA site and CTT colder than -28°C at the AWR
 410 site, as discussed in Figure 2a.

411



412

413 Figure 3. Monthly statistics of stratiform mixed-phase clouds at the NSA (black) and AWR (red)
 414 sites: (a) CTT, (b) CTH, (c) CBH, and (d) THK. The box-and-whisker plots provide 10th, 25th,
 415 50th, 75th, and 90th percentiles of the month statistics. Shaded boxes represent the observations
 416 and clear boxes represent the EAMv2 simulation. Monthly means are shown by diamonds and
 417 circles for the observation and model, respectively.

418

419 The monthly statistics of simulated CTH, CBH, and THK in collocated SMPCs are
 420 shown in Figures 3b-d. At the NSA site, the significant underestimation of CTH in early boreal
 421 spring dominates the biased PDF for CTH lower than 1 km (Figure 2b). Note that the

422 underestimation of CTH in early boreal spring is primarily related to our averaging method. As
423 we averaged 30-second SMPC data to hourly resolution as long as SMPC appears once within
424 that one-hour segment, we found that early spring has a significant amount of data containing
425 target SMPCs for less than 30 minutes during each one-hour time segment at NSA. The biased
426 CTH will be substantially alleviated if a minimum 30-minute criterion is considered in the data
427 processing (not shown). A similar influence is also found for biases in CBH and THK at the
428 NSA site in the same season. Consistent with the PDF analysis, Arctic SMPCs are frequently
429 formed at altitudes close to the surface (CBH below 0.5 km) throughout the year in both model
430 simulation and observation. Compared to the observed THK, the simulated mean THK for
431 collocated SMPCs is thinner from late boreal winter to late spring, but the model overestimates
432 the mean THK in boreal summer and early autumn at the NSA site (Figure 3d). The
433 compensating errors cancel out the biases shown in the annual THK PDF. For simulated cloud
434 boundary properties at the AWR site, EAMv2 overestimates monthly mean CTH from austral
435 late summer to mid-spring. The overestimation leads to statistically more simulated SMPCs with
436 CTH higher than 4 km in austral summer and autumn, shifting the CTH PDF toward higher
437 altitudes (Figure 2b). Moreover, biases in CBH and THK are persistent all year round compared
438 to the observations at the AWR site. The mean cloud base of collocated SMPCs in EAMv2 is
439 substantially higher in all months, and the simulated mean cloud thickness is thinner than the
440 observations except in late austral summer. The high CBH bias and low THK bias primarily
441 result in the overestimated probabilities for cloud bases higher than 2 km and cloud layers
442 thinner than 1 km at the AWR site. By comparing the monthly statistics of cloud macrophysical
443 properties between the two sites, the model well simulates the hemispheric difference in
444 observed cloud macrophysical properties in individual months. These features include colder

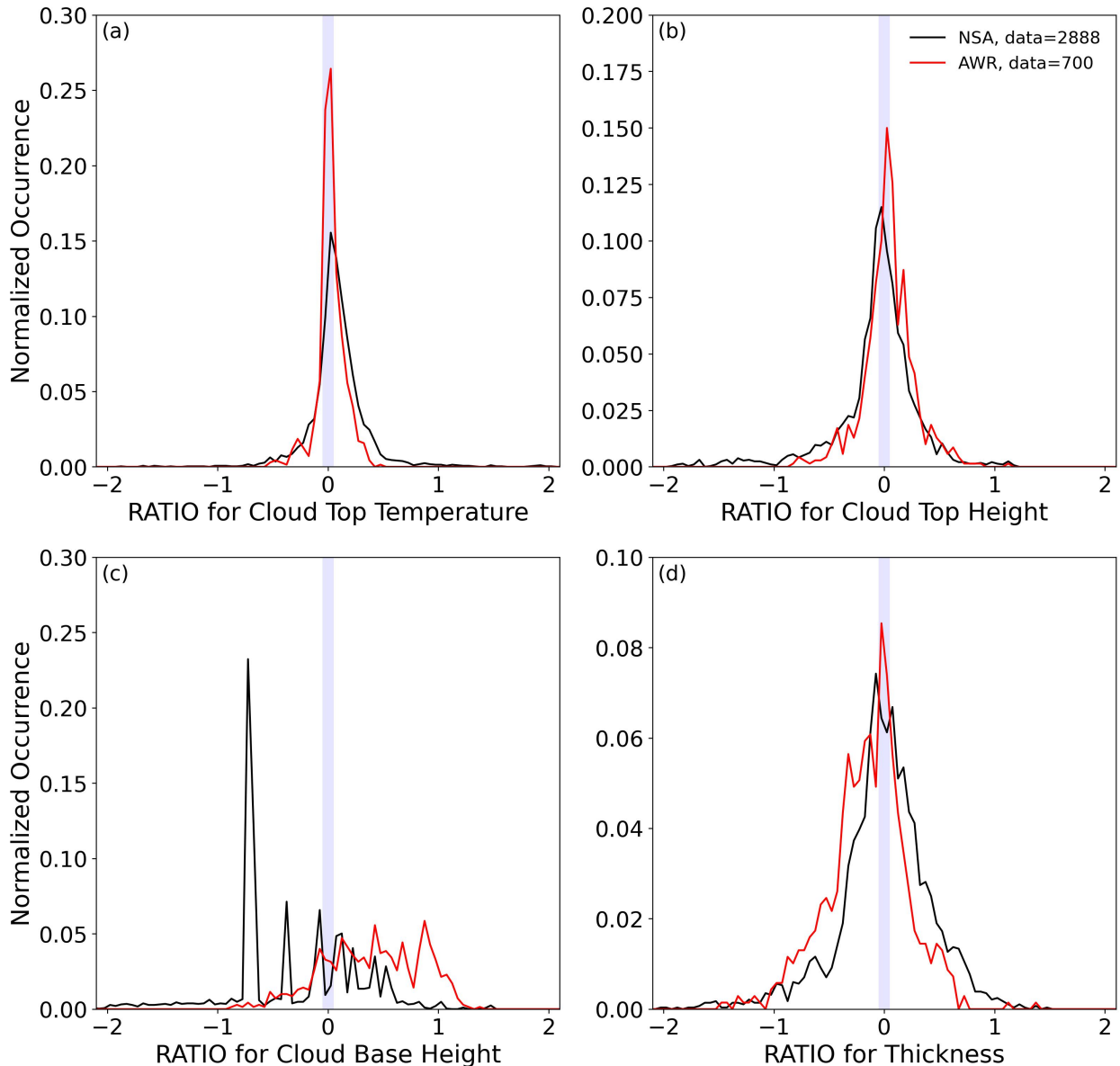
445 CTT, higher CTH, higher CBH, and thicker THK in the Antarctic SMPC compared to the Arctic
 446 clouds.

447 To better quantify model biases in the representation of SMPC properties, we perform
 448 case-by-case comparisons of collocated SMPCs between EAMv2 and DZ19. The case-by-case
 449 evaluation provides details of individual SMPCs that are simultaneously present in the model
 450 and observation under comparable atmospheric conditions with nudged circulation and
 451 temperature in the model. We use “RATIO,” which is the common logarithm of the ratio of an
 452 EAMv2 simulated cloud property over an observed cloud property for each pair of the collocated
 453 data (Equation 1), to describe the errors in simulated SMPC properties. The RATIO value of 0
 454 indicates that the simulated cloud property is the same as the observed value. $RATIO > 0$ (< 0)
 455 suggests that the simulated cloud property is overestimated (underestimated) compared to the
 456 observation. We consider the RATIO range within ± 0.05 as a reasonable model performance,
 457 which represents approximately $\pm 10\%$ differences from the observations.

$$458 \quad RATIO_{Property} = \log_{10} \frac{Property_{EAMv2}}{Property_{ARM}} \quad (1)$$

459 The normalized occurrences of RATIO for CTT, CTH, CBH, and THK are shown in
 460 Figure 4. Normalized occurrence is calculated by dividing the amount of data in each cloud
 461 property bin by the total amount of data. $RATIO_{CTT}$ exhibits a normal distribution pattern at both
 462 NSA and AWR sites with the largest occurrences near 0, indicating that the majority of
 463 simulated CTT is comparable to observed CTT when evaluating SMPCs with the case-by-case
 464 comparison. However, EAMv2 tends to simulate more occurrences of colder CTT than warmer
 465 CTT against the observations, indicated by the long tails on $RATIO_{CTT} > 0$. Normal distribution-
 466 like patterns are also shown for $RATIO_{CTH}$ and $RATIO_{THK}$ at the NSA site. Despite the PDF
 467 peaks around 0, the occurrences of $RATIO_{CTH}$ and $RATIO_{THK}$ beyond ± 0.05 (outside blue boxes)

468 are also relatively large at both sites, suggesting biases in simulated cloud boundaries. Consistent
 469 with earlier discussion, secondary peaks are shown at about 0.2 for $RATIO_{CTH}$ and below 0 for
 470 $RATIO_{THK}$ at AWR, which indicates the too-high CTH and too-thin THK in simulated SMPCs.
 471 Interestingly, even with fewer collocated data, the SMPCs at AWR have larger normalized
 472 occurrences within the ± 0.05 range as compared with the SMPCs at NSA for $RATIO_{CTT}$,
 473 $RATIO_{CTH}$, and $RATIO_{THK}$.
 474



475

476 Figure 4. Normalized occurrence of the RATIO metrics for CTT (a), CTH (b), CBH (c), and
 477 THK (d) at the NSA (black) and AWR (red) sites. RATIO is defined as the common logarithm of
 478 the ratio of EAMv2 modeled cloud properties divided by the observed cloud properties for
 479 collocated stratiform mixed-phase clouds. The blue shaded area shows the region where RATIOS
 480 are between -0.05 and 0.05, which represents approximately $\pm 10\%$ differences from the
 481 observations. Note that the cloud top temperature is in the unit of $^{\circ}\text{C}$.

482

483 $\text{RATIO}_{\text{CBH}}$ differs significantly between the NSA and AWR sites (Figure 4c). There is a
 484 peak occurrence at approximately -0.8 at NSA, and the normalized occurrence shows a
 485 decreasing trend from -0.8 to 0.5. The high occurrence of negative values of $\text{RATIO}_{\text{CBH}}$ is
 486 mostly associated with the early spring cases as shown in Figure 3c, in which the model largely
 487 underestimates cloud bases of SMPC at the NSA. Unlike the NSA site, $\text{RATIO}_{\text{CBH}}$ for SMPCs at
 488 the AWR site is primarily positive. The high occurrence of positive values of $\text{RATIO}_{\text{CBH}}$ is
 489 consistent with the annual and monthly statistical analysis shown in Figures 2 and 3. It is worth
 490 noting that a substantial hemispheric difference is identified in the CBH bias, while biases of
 491 other cloud microphysical properties generally share similar normalized distributions at both
 492 hemispheres.

493

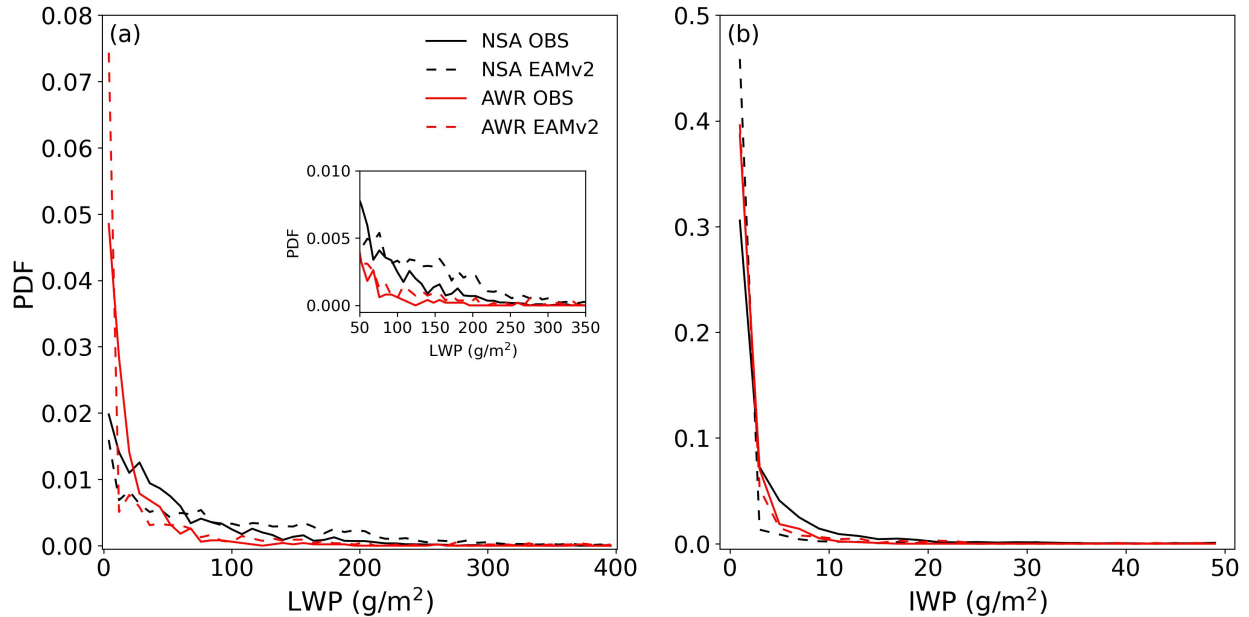
494 **5.3. Cloud Microphysical Properties**

495 In this section, cloud microphysical properties (i.e., LWP and IWP) of collocated SMPCs
 496 in EAMv2 are evaluated against the ARM measurements at the NSA and AWR sites. The PDFs
 497 of LWP and IWP annual statistics are shown in Figure 5. Rain and snow water are included in
 498 the calculation of LWP and IWP in EAMv2 because ground-based remote sensing cannot

499 distinguish them from cloud liquid and ice water. The PDFs of observed LWP and IWP both
500 show the monotonic decreasing features with increasing LWP and IWP. The largest probabilities
501 are at LWP lower than 20 g/m^2 and IWP lower than 5 g/m^2 , respectively. More occurrences of
502 large LWP ($> 20 \text{ g/m}^2$) and IWP ($> 5 \text{ g/m}^2$) are found at the NSA site than at the AWR site in the
503 observation. Compared with DZ19, the probabilities of EAMv2 simulated LWP are larger when
504 LWP is greater than 100 g/m^2 at both NSA and AWR sites. At the same time, lower probabilities
505 of LWP smaller than 50 g/m^2 are simulated at NSA, while simulated Antarctic SMPCs have
506 significantly larger probabilities of LWP close to 0 g/m^2 than the observation. The overestimated
507 occurrences of large LWP in EAMv2 are consistent with M. Zhang et al. (2022) in both
508 hemispheres, in which the CALIPSO simulator-derived cloud liquid covers are substantially
509 overestimated against the CALIPSO-GOCCP data over high-latitude regions. However,
510 inconsistent results are shown in the ice phase evaluation. Although M. Zhang et al. (2022)
511 illustrated that the low bias in cloud ice cover is much improved in Arctic clouds in EAMv2
512 compared to EAMv1, the probabilities of IWP larger than 5 g/m^2 are still underestimated in
513 EAMv2 for the collocated SMPCs at the NSA site (Figure 5b). Meanwhile, even though the
514 simulated IWP PDF is generally comparable to DZ19 at the AWR site, a substantial low bias
515 was shown in ice cloud cover in M. Zhang et al. (2022) in the Antarctic. The different outcome
516 in the ice phase evaluation against DZ19 and CALIPSO-GOCCP is probably a mixed result from
517 differences in the observations (ground-based versus space-borne remote sensing measurements),
518 model simulations (nudged runs vs. climate free runs), and data sampling (collocated cases vs.
519 climatology). For instance, for the Arctic SMPCs, the precipitating ice below supercooled liquid
520 layer is often missed by the CALIPSO lidar due to the strong attenuation of lidar beam by the
521 optically thick liquid water at cloud top. On the other hand, the ground-based radar and lidar

522 combined measurements can more accurately detect these precipitating hydrometeors, leading to
 523 larger amounts of cloud ice water in DZ19.

524



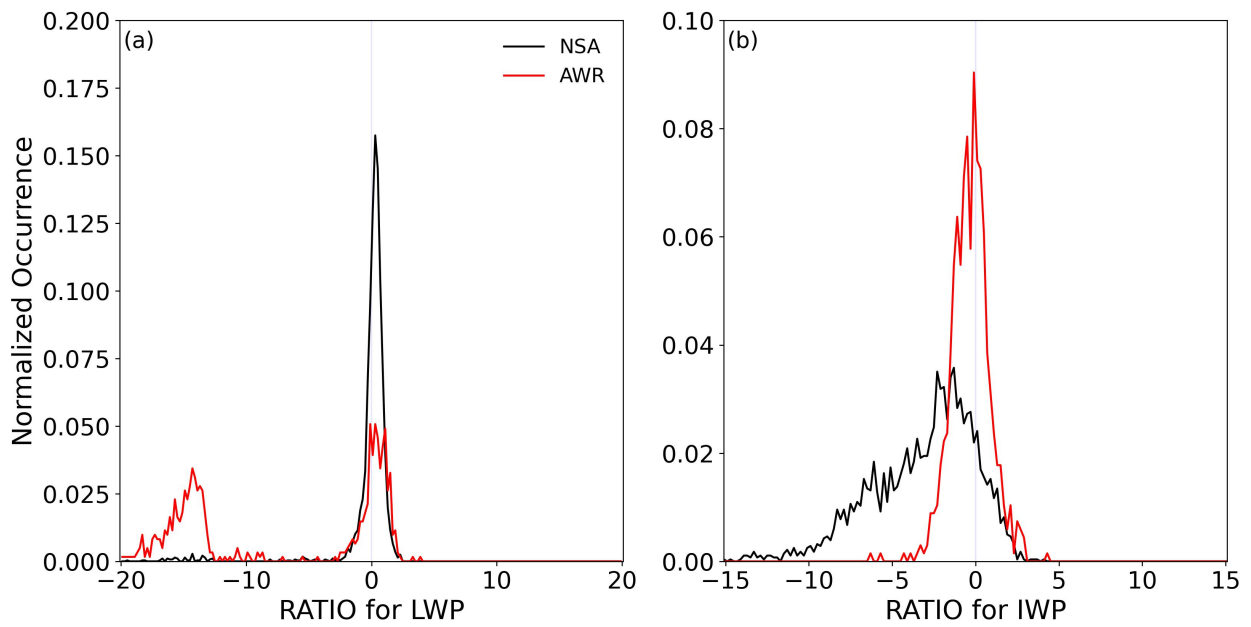
525

526 Figure 5. PDFs of observed and modeled liquid water path (LWP, a) and ice water path (IWP, b)
 527 for collocated stratiform mixed-phase clouds between EAMv2 (dashed line) and ARM retrievals
 528 (solid line). Black color represents the NSA site and red color represents the AWR site. The inlet
 529 figure in (a) is the PDF for LWP ranging from 50 to 350 g/m^2 .

530

531 By evaluating $\text{RATIO}_{\text{LWP}}$ and $\text{RATIO}_{\text{IWP}}$ through case-by-case comparisons of collocated
 532 SMPCs, biases in simulated LWP and IWP are identified under comparable large-scale
 533 conditions. Figure 6 shows that EAMv2 frequently overestimates LWP in collocated SMPCs at
 534 both sites, consistent with the PDF analysis in Figure 5. The distribution of $\text{RATIO}_{\text{LWP}}$ peaks
 535 close to 0.5 at the NSA site. The overestimation of LWP is found in all seasons at the NSA, and
 536 the overestimation is the most substantial in austral summer when analyzing their monthly

537 statistics (not shown). At the AWR site, the highest peak of $RATIO_{LWP}$ is found around 0, but
 538 $RATIO_{LWP}$ also peaks at about -15. We note that the large occurrences of $RATIO_{LWP}$ smaller
 539 than -10 at AWR are associated with simulated clouds dominated by ice water. The dominance
 540 of ice water in simulated SMPC in the Antarctic is probably because of the cold temperature that
 541 effectively favors ice phase microphysical processes. This feature is further suggested by the
 542 large amounts of data located at $RATIO_{IWP}$ between ± 0.5 at the AWR site. On the other hand,
 543 most data are associated with negative $RATIO_{IWP}$ at NSA, with a negative peak close to -2. This
 544 negative peak again indicates insufficient ice water formation in SMPCs at the NSA site. The
 545 underestimation of IWP is found throughout the year at the NSA site (not shown). Negative
 546 biases in IWP compared to the ARM long-term measurements are consistent with M. Zhang et
 547 al. (2020), where EAMv1 was evaluated against the observational data from the ARM M-PACE
 548 field campaign in October 2004. Similar negative ice phase biases in EAMv2 imply that ice-
 549 related microphysics needs further improvements in the future E3SM model development.
 550



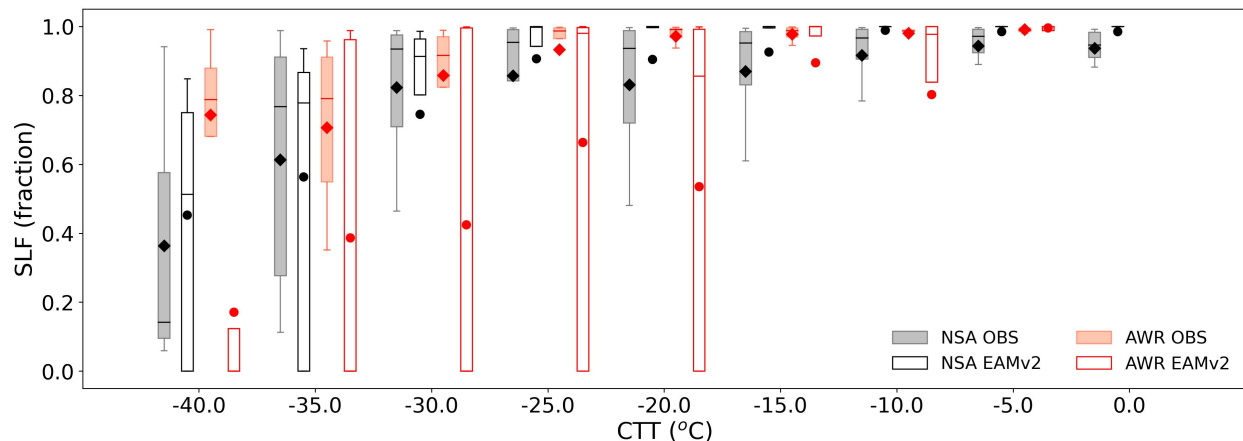
551

552 Figure 6. Normalized occurrence of the RATIO metrics for LWP (a) and IWP (b) at the NSA
553 (black) and AWR (red) sites. The blue shaded area shows the region where RATIOS are between
554 -0.05 and 0.05, which represents approximately $\pm 10\%$ differences from the observations.

555

556 Several studies showed that measured SLF in mixed-phase clouds in the Northern
557 Hemisphere is substantially smaller than in the Southern Hemisphere at a given temperature (Tan
558 et al., 2014; D. Zhang et al., 2019). By examining the SLF statistics of collocated SMPCs in
559 different CTT bins, lower SLF is also observed in collocated SMPCs at the NSA site compared
560 with clouds at the AWR site (Figure 7). However, such a hemispheric difference in SLF is poorly
561 simulated for collocated SMPCs at the two ARM locations in EAMv2. At individual CTT bins
562 from -40°C to -10°C , simulated SLF at the NSA site is consistently larger than at the AWR site.
563 The biased LWP and IWP at both sites together contribute to the biased hemispheric difference
564 of SLF. For example, EAMv2 frequently underestimates IWP while LWP is reasonable at NSA,
565 making simulated SLF too large in most CTT bins compared with DZ19. Meanwhile, simulated
566 LWP in collocated SMPCs is frequently underestimated at the AWR site, but the IWP in these
567 SMPCs is overall comparable to the observation. The biased cloud water in liquid and ice phases
568 at the AWR site results in a much lower SLF than the observation and even lower than that at the
569 NSA, especially at CTT colder than -10°C .

570



571
 572 Figure 7. The box-and-whisker plots of supercooled liquid fraction (SLF) as a function of cloud
 573 top temperature in collocated stratiform mixed-phase clouds at the NSA (black) and AWR (red)
 574 sites. The box-and-whisker plots provide the 10th, 25th, 50th, 75th, and 90th percentiles of the SLF
 575 in each temperature bin. Shaded boxes represent the observations and clear boxes represent the
 576 EAMv2 simulation. The mean SLF for each temperature bin is shown by the diamond and circle
 577 for the observation and model, respectively.

578

579

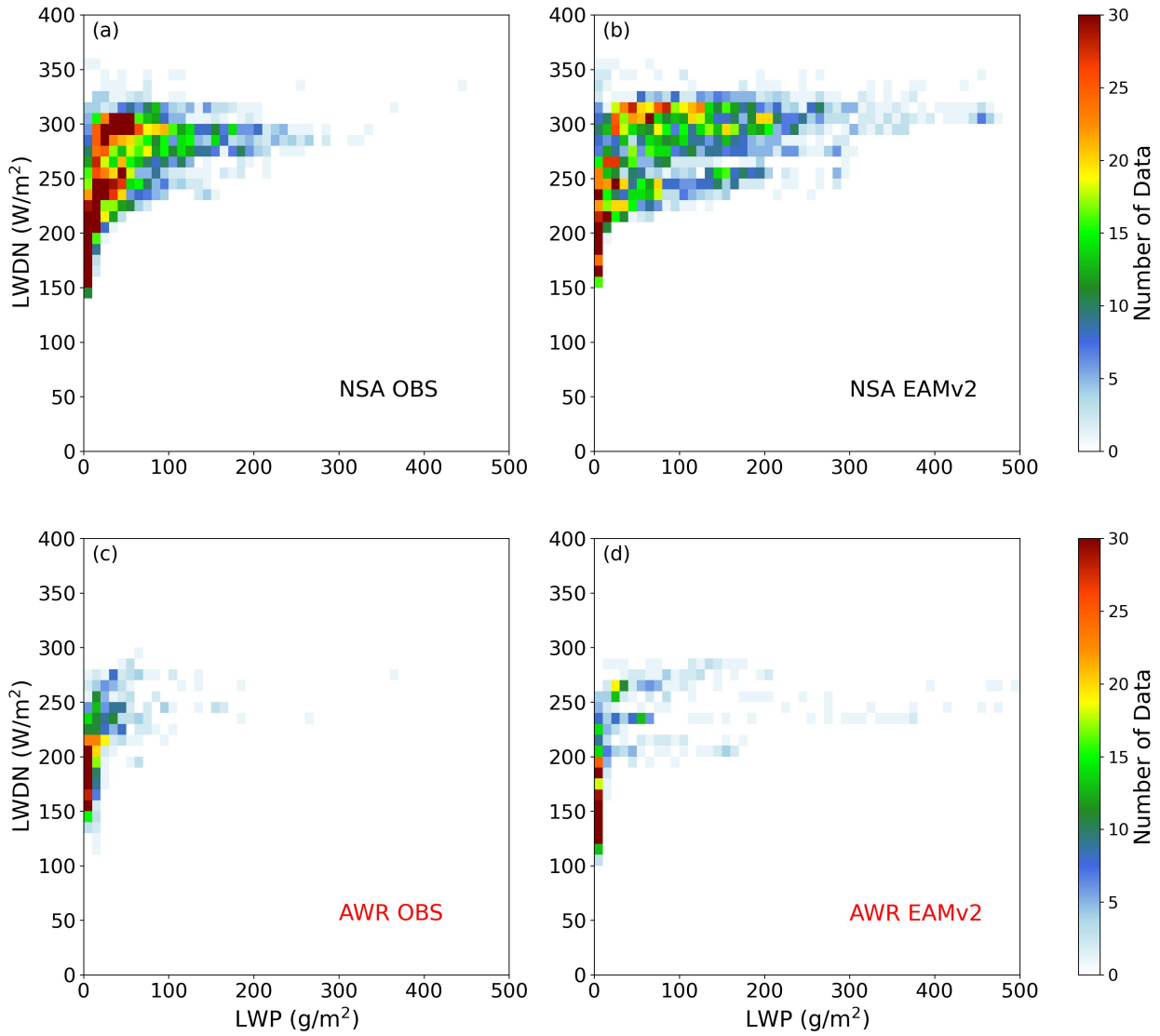
580 **5.4. Cloud Radiative Properties**

581 It is well-known that LWP plays a more critical role in cloud radiative effects than IWP
 582 in mixed-phase clouds (Bennartz et al., 2013; Nicolas et al., 2017). To understand how the model
 583 simulated LWP influences the surface radiation at the NSA and AWR sites, we compare the
 584 surface downwelling longwave (LWDN) radiative fluxes between EAMv2 and ARMBE data for
 585 all collocated SMPCs. The reason for examining LWDN at the surface is because it can directly
 586 reflect the impact of cloud properties on cloud radiative effects. To exclude the effect of multiple
 587 scattering between the bright underneath surface and the low-level SMPCs in high latitude
 588 regions (Xie et al., 2006), surface downwelling shortwave radiation is thus not shown. The two-

589 dimensional histograms between LWP and LWDN are shown in Figure 8. In terms of the
 590 relations between LWP and LWDN, the majority of observed SMPCs have LWP below 130
 591 g/m^2 (90th percentile) at the NSA site. The associated LWDN is observed to range between 150
 592 and 350 W/m^2 for the collocated SMPC samples. At the AWR site, most observed LWP is less
 593 than 50 g/m^2 (90th percentile), and the emitted LWDN is mostly below 280 W/m^2 , both of which
 594 are much lower than those at the NSA site. The colder temperature and lower LWP in observed
 595 SMPCs at AWR can largely explain this hemispheric difference in LWDN. Compared to the
 596 observations, regardless of the large amounts of data with small LWP values ($\text{RATIO}_{\text{LWP}} < -10$)
 597 at the AWR site, the model overestimation of LWP is shown at both sites. The occurrences of
 598 modeled LWP greater than 130 g/m^2 at the NSA and the occurrences of LWP greater than 50
 599 g/m^2 at the AWR are approximately 3.1 times and 2.4 times higher than the observations,
 600 respectively. As expected, this larger LWP in simulated SMPCs leads to stronger LWDN at the
 601 surface. At the NSA in EAMv2, nearly 34% of the collocated SMPCs with LWP greater than
 602 130 g/m^2 have LWDN stronger than 305 W/m^2 (90th percentile of observed LWDN). The
 603 occurrences of these SMPCs with large LWP and LWDN are substantially (6.5 times) more than
 604 the observation. At the AWR site, almost all the collocated SMPCs with LWP larger than 50
 605 g/m^2 have LWDN larger than 200 W/m^2 in EAMv2, contributing to about 63% of the
 606 occurrences of large LWDN ($> 260 \text{ W/m}^2$, 90th percentile of observed LWDN at AWR) in the
 607 model. The occurrence of simulated strong LWDN is thus larger than the observed radiative flux
 608 by a factor of 3.2. Nicolas et al. (2016) suggested that mixed-phase clouds with LWP greater
 609 than 40 g/m^2 can be optically thick enough to attenuate shortwave radiation and emit longwave
 610 radiation as the blackbody. These clouds can remarkably influence the surface energy budget and
 611 lead to extensive melting events over West Antarctica. Therefore, EAMv2 simulated too strong

612 LWDN fluxes at the surface will potentially also result in a biased prediction of the surface
613 energy budget and then impact the model simulation of surface melting events and regional and
614 global climate prediction.

615



616

617 Figure 8. 2-D Histograms of longwave downward radiative flux (LWDN) at the surface and
618 LWP at the NSA (a-b) and AWR (c-d) sites from EAMv2 and ARM observations.

619

620

621 **6. Summary and discussion**

622 This study evaluates the cloud properties of high-latitude SMPCs simulated by EAMv2
623 against the U.S. DOE ARM ground-based remote sensing retrievals at the NSA and AWR sites
624 in 2016. To improve the model-observation comparison, the horizontal wind (U, V) and
625 temperature (T) fields are nudged toward ERA-Interim reanalysis data for 2016 with a nudging
626 relaxation time scale of 6 hours. Simulated clouds are selected with similar characteristics to
627 observed clouds by using the consistent definitions used in the ARM retrievals. In general, the
628 model reproduces the seasonal variation of the frequency of occurrence of observed SMPCs at
629 both sites. The larger SMPC frequency of occurrence at the NSA site than at the AWR site is
630 also well simulated. However, EAMv2 tends to overestimate cloud frequency of occurrence from
631 boreal mid-summer to spring at the NSA while underestimating the frequency of occurrence
632 throughout the year at the AWR, which is consistent with the CALIPSO-GOCCP evaluation by
633 M. Zhang et al. (2022).

634 Under constrained large-scale environments in the nudging simulations, a collocation
635 method is applied to the SMPCs from the model and observations to merit case-by-case
636 comparisons. Collocated evaluation indicates that EAMv2 simulated SMPCs well capture the
637 observed annual statistics in the PDFs of cloud macrophysical properties at the NSA site.
638 Through monthly and case-by-case evaluations, the largest model biases are found in early
639 boreal spring, when the model largely underestimates CTH, CBH, and THK at the NSA. At the
640 AWR site, larger biases are shown in simulated SMPC properties. In particular, simulated CTH
641 and CBH are much higher than observations across the year. The larger magnitude of
642 overestimation in CBH leads to the underestimated THK in the Antarctic clouds. Regardless of
643 the biases in the statistical comparison of cloud macrophysical properties, our collocated SMPCs

644 in EAMv2 well resemble the observed hemispheric differences such as the higher CTH and
645 CBH, larger THK, and colder CTT at the AWR site than those clouds at the NSA site.

646 Model biases in cloud microphysical properties are more noticeable than cloud
647 geometrical properties. At the NSA site, there are substantially more simulated SMPCs with
648 LWP greater than 100 g/m^2 compared with the observation. The frequent overestimated LWP
649 results in positive biases in the simulation of longwave downward radiative fluxes at the surface.
650 By analyzing case-by-case comparisons, we found that EAMv2 tends to simulate SMPCs with
651 significantly underestimated LWP at the AWR site. These extreme SMPC cases are ice water
652 dominated and are primarily associated with the cold environment in the Antarctic region that
653 effectively favors ice microphysical processes. For simulated IWP, although M. Zhang et al.
654 (2022) shows a much-improved ice phase cloud cover in EAMv2 compared to EAMv1, the
655 evaluation in this study still indicates that EAMv2 underestimates cloud ice water as compared
656 with ground-based remote sensing retrievals at the NSA site. Such a discrepancy suggests that
657 different instrument limitations must be considered in the model evaluation. The different
658 capability of instruments to detect precipitating ice below supercooled liquid layers, which is a
659 common feature in high-latitude mixed-phase clouds, probably explains the cloud ice difference
660 in space- and ground-based remote sensing retrievals. In addition, the different types of model
661 simulations (nudged runs vs. climate free runs) and different data sampling methods (collocated
662 cases vs. climatology) also attribute to the discrepancy. The biased cloud water path simulation
663 makes the observed hemispheric difference in SLF poorly simulated in EAMv2, which becomes
664 opposite to the observation.

665 In recent model development studies, secondary ice production (SIP) has received more
666 attention due to its essential role in bridging the gap of orders of magnitude differences between

667 cloud ice number concentration and ice nucleating particle concentrations in high-latitude mixed-
668 phase clouds (Zhao & Liu, 2021, 2022; Zhao et al., 2021). In the current MG2 cloud
669 microphysics, SIP is only represented by the Hallett-Mossop process within the narrow
670 temperature range from -3 to -8°C. Other SIP mechanisms, such as frozen raindrop shattering and
671 ice-ice collisional breakup, are still missing in E3SMv2. By including these mechanisms, Zhao et
672 al. (2021) demonstrated that SIP is the dominant source of ice crystals for Arctic mixed-phase
673 clouds, especially when clouds are formed in a relatively warm temperature range. Meanwhile,
674 enhancing ice phase cloud microphysical processes could alleviate the issue of overestimated
675 liquid cloud water in Arctic mixed-phase clouds. This could also eventually improve the model
676 representation of anthropogenic aerosol forcing, as overestimated LWP was found to lead to
677 larger anthropogenic aerosol effects through aerosol-cloud interactions in the Arctic region (K.
678 Zhang et al., 2022).

679 In conclusion, this study illustrates that the EAMv2 model has the capability to
680 reasonably simulate the annual statistics of SMPC cloud macrophysical property differences
681 between two polar locations. The reproduction of hemispheric differences in cloud structure in
682 the state-of-the-art GCM will be helpful to better understand the formation mechanisms in high-
683 latitude mixed-phase clouds in both hemispheres. However, further efforts are needed in the
684 development of cloud microphysical parameterizations to achieve a reasonable representation of
685 cloud phase over two high-latitude regions.

686

687

688

689 **Acknowledgment:** This research was supported as part of the Energy Exascale Earth System
690 Model (E3SM) project, funded by the U.S. Department of Energy, Office of Science, Office of
691 Biological and Environmental Research. Work at LLNL was performed under the auspices of the
692 U.S. DOE by Lawrence Livermore National Laboratory under contract No. DE-AC52-
693 07NA27344. Xiaohong Liu acknowledges the funding support by the DOE Atmospheric System
694 Research (ASR) Program (grant DE-SC0020510) and the DOE Regional and Global Model
695 Analysis (RGMA) Program (grant DE-SC0022065). The Pacific Northwest National Laboratory
696 (PNNL) is operated for the DOE by the Battelle Memorial Institute under contract DE-AC06-
697 76RLO 1830. This research used resources of the National Energy Research Scientific
698 Computing Center (NERSC), a U.S. Department of Energy Office of Science User Facility
699 located at Lawrence Berkeley National Laboratory, operated under Contract No. DE-AC02-
700 05CH11231.

701
702 **Data Availability Statement:** The U.S. DOE E3SMv2 (E3SM Project, DOE, 2021, September
703 29) model was used in the creation of this manuscript. The model data used in this study can be
704 accessible at [https://portal.nersc.gov/archive/home/m/mengz/www/Zhang-E3SMv2-](https://portal.nersc.gov/archive/home/m/mengz/www/Zhang-E3SMv2-MixedPhaseClouds-ARM)
705 [MixedPhaseClouds-ARM](https://portal.nersc.gov/archive/home/m/mengz/www/Zhang-E3SMv2-MixedPhaseClouds-ARM). The ARM observational data are available online at
706 <https://www.arm.gov/data>.

707 **References**

708 Bennartz, R., Shupe, M. D., Turner, D. D., Walden, V. P., Steffen, K., Cox, C. J., et al. (2013).

709 July 2012 Greenland melt extent enhanced by low-level liquid clouds. *Nature*, 496, 83–86.

710 <https://doi.org/10.1038/nature12002>

711

712 Bradley, A. M., Bosler, P. A., & Guba, O. (2021). Islet: Interpolation semi-Lagrangian element-

713 based transport, *Geoscientific Model Development Discussion*. [https://doi.org/10.5194/gmd-](https://doi.org/10.5194/gmd-2021-296)

714 2021-296

715

716 Clothiaux, E. E., Ackerman, T. P., Mace, G. G., Moran, K. P., Marchand, R. T., Miller, M. A., &

717 Martner, B. E. (2000). Objective Determination of Cloud Heights and Radar Reflectivities Using

718 a Combination of Active Remote Sensors at the ARM CART Sites, *Journal of Applied*

719 *Meteorology*, 39(5), 645–665. [https://doi.org/10.1175/1520-](https://doi.org/10.1175/1520-0450(2000)039<0645:ODOCHA>2.0.CO;2)

720 [0450\(2000\)039<0645:ODOCHA>2.0.CO;2](https://doi.org/10.1175/1520-0450(2000)039<0645:ODOCHA>2.0.CO;2)

721

722 Curry, J. A., Schramm, J. L., Rossow, W. B., & Randall, D. (1996). Overview of Arctic Cloud

723 and Radiation Characteristics. *Journal of Climate*, 9(8), 1731–1764.

724 [https://doi.org/10.1175/1520-0442\(1996\)009<1731:OOACAR>2.0.CO;2](https://doi.org/10.1175/1520-0442(1996)009<1731:OOACAR>2.0.CO;2)

725

726 Gettelman, A., Hannay, C., Bacmeister, J. T., Neale, R. B., Pendergrass, A. G., Danabasoglu, G.,

727 et al. (2019). High climate sensitivity in the Community Earth System Model Version 2

728 (CESM2). *Geophysical Research Letters*, 46, 8329–8337.

729 <https://doi.org/10.1029/2019GL083978>

730

731 Gettelman, A., & Morrison, H. (2014). Advanced two-moment bulk microphysics for global
732 models. Part I: Off-line tests and comparison with other schemes. *Journal of Climate*, 28(3),
733 1268–1287. <https://doi.org/10.1175/JCLI-D-14-00102.1>

734

735 Golaz, J.-C., Larson, V. E., & Cotton, W. R. (2002). A PDF-based model for boundary layer
736 clouds. Part I: Method and model description. *Journal of the Atmospheric Sciences*, 59(24),
737 3540–3551. [https://doi.org/10.1175/1520-0469\(2002\)059<3540:APBMFB>2.0.CO;2](https://doi.org/10.1175/1520-0469(2002)059<3540:APBMFB>2.0.CO;2)

738

739 Golaz, J.-C., Van Roekel, P. L., Zheng, X., Roberts, A., Wolfe, D. J., Lin, W., et al. (2022). The
740 DOE E3SM Model Version 2: Overview of the physical model. *Earth and Space Science Open*
741 *Archive*. <https://doi.org/10.1002/essoar.10511174.1>

742

743 Gregory, D., & Morris, D. (1996). The sensitivity of climate simulations to the specification of
744 mixed phase clouds. *Climate Dynamics*, 12, 641–651. <https://doi.org/10.1007/BF00216271>

745

746 Hannah, W. M., Bradley, A. M., Guba, O., Tang, Q., Golaz, J.-C., & Wolfe, J. (2021).
747 Separating physics and dynamics grids for improved computational efficiency in spectral
748 element earth system models. *Journal of Advances in Modeling Earth Systems*, 13,
749 e2020MS002419. <https://doi.org/10.1029/2020MS002419>

750

751 Harrop, B. E., Ma, P.-L., Rasch, P. J., Neale, R. B., & Hannay, C. (2018). The role of convective
752 gustiness in reducing seasonal precipitation biases in the tropical west pacific. *Journal of*
753 *Advances in Modeling Earth Systems*, 10 (4), 961–970. <https://doi.org/10.1002/2017MS001157>
754

755 Hogan, R. J., Mittermaier, M. P., & Illingworth, A. J. (2006). The retrieval of ice water content
756 from radar reflectivity factor and temperature and its use in evaluating a mesoscale model.
757 *Journal of Applied Meteorology and Climatology*. 45(2), 301–317. [https://doi.org/10.1175/](https://doi.org/10.1175/JAM2340.1)
758 JAM2340.1
759

760 Hoose, C., Kristjánsson, J. E., Chen, J. P., & Hazra, A. (2010). A classical-theory-based
761 parameterization of heterogeneous ice nucleation by mineral dust, soot, and biological particles
762 in a global climate model. *Journal of the Atmospheric Sciences*, 67(8), 2483–2503. [https://doi.](https://doi.org/10.1175/2010JAS3425.1)
763 [org/10.1175/2010JAS3425.1](https://doi.org/10.1175/2010JAS3425.1)
764

765 Klein, S. A., McCoy, R. B., Morrison, H., Ackerman, A. S., Avramov, A., Boer, G. d., et al.
766 (2009). Intercomparison of model simulations of mixed-phase clouds observed during the ARM
767 Mixed-Phase Arctic Cloud Experiment. I: single-layer cloud. *Quarterly Journal of the Royal*
768 *Meteorological Society*, 135, 979–1002. <https://doi.org/10.1002/qj.416>
769

770 Korolev, A., McFarquhar, G., Field, P. R., Franklin, C., Lawson, P., Wang, Z., et al. (2017).
771 Mixed-Phase Clouds: Progress and Challenges. *Meteorological Monographs*. 58, 5.1-5.50.
772 <https://doi.org/10.1175/AMSMONOGRAPHS-D-17-0001.1>
773

- 774 Larson, V. E. (2017). CLUBB-SILHS: A parameterization of subgrid variability in the
775 atmosphere. arXiv preprint arXiv:1711.03675v2
776
- 777 Liu, X., Easter, R. C., Ghan, S. J., Zaveri, R., Rasch, P., Shi, X., et al. (2012). Toward a minimal
778 representation of aerosols in climate models: description and evaluation in the Community
779 Atmosphere Model CAM5, *Geoscientific Model Development*, 5, 709–739.
780 <https://doi.org/10.5194/gmd-5-709-2012>
781
- 782 Liu, X., Ma, P.-L., Wang, H., Tilmes, S., Singh, B., Easter, R. C., et al. (2016). Description and
783 evaluation of a new four-mode version of the Modal Aerosol Module (MAM4) within version
784 5.3 of the Community Atmosphere Model. *Geoscientific Model Development*, 9(2), 505–522.
785 <https://doi.org/10.5194/gmd-9-505-2016>
786
- 787 Liu, Y., Shupe, M. D., Wang, Z., & Mace, G. (2017). Cloud vertical distribution from combined
788 surface and space radar–lidar observations at two Arctic atmospheric observatories. *Atmospheric*
789 *Chemistry and Physics*, 17, 5973–5989, <https://doi.org/10.5194/acp-17-5973-2017>
790
- 791 Lohmann, U. & Neubauer, D. (2018). The importance of mixed-phase and ice clouds for climate
792 sensitivity in the global aerosol–climate model ECHAM6-HAM2. *Atmospheric Chemistry and*
793 *Physics*, 18, 8807–8828. <https://doi.org/10.5194/acp-18-8807-2018>
794
- 795 Lubin, D., Zhang, D., Silber, I., Scott, R. C., Kalogeras, P., Battaglia, A., et al. (2020). AWARE:
796 The Atmospheric Radiation Measurement (ARM) West Antarctic Radiation Experiment, *Bulletin*

797 *of the American Meteorological Society*, 101(7), E1069-E1091. <https://doi.org/10.1175/BAMS->
798 D-18-0278.1

799

800 Ma, P.-L., Harrop, B. E., Larson, V. E., Neale, R., Gettelman, A., Morrison, H., et al. (2022).

801 Better calibration of cloud parameterizations and subgrid effects increases the fidelity of E3SM
802 Atmosphere Model version 1, *Geoscientific Model Development*. 15(7), 2881–2916.

803 <https://doi.org/10.5194/gmd-15-2881-2022>

804

805 McCoy, D. T., Hartmann, D. L., Zelinka, M. D., Ceppi, P., & Grosvenor, D. P. (2015). Mixed-

806 phase cloud physics and Southern Ocean cloud feedback in climate models. *Journal of*

807 *Geophysical Research: Atmospheres*, 120, 9539–9554, <https://doi.org/10.1002/2015JD023603>

808

809 McCoy, D. T., Tan, I., Hartmann, D. L., Zelinka, M. D., & Storelvmo, T. (2016). On the

810 relationships among cloud cover, mixed-phase partitioning, and planetary albedo in GCMs.

811 *Journal of Advances in Modeling Earth Systems*, 8, 650–668.

812 <https://doi.org/10.1002/2015MS000589>

813

814 McErlich, C., McDonald, A., Schuddeboom, A., & Silber, I. (2021). Comparing satellite- and

815 ground-based observations of cloud occurrence over high southern latitude. *Journal of*

816 *Geophysical Research: Atmospheres*, 126, e2020JD033607.

817 <https://doi.org/10.1029/2020JD033607>

818

819 McFarquhar, G. M., Bretherton, C. S., Marchand, R., Protat, A., DeMott, P. J., Alexander, S. P.,
820 et al. (2021). Observations of Clouds, Aerosols, Precipitation, and Surface Radiation over the
821 Southern Ocean: An Overview of CAPRICORN, MARCUS, MICRE, and SOCRATES. *Bulletin*
822 *of the American Meteorological Society*, 102(4), E894–E928. [https://doi.org/10.1175/BAMS-D-](https://doi.org/10.1175/BAMS-D-20-0132.1)
823 20-0132.1

824

825 Middlemas, E. A., Kay, J. E., Medeiros, B. M., & Maroon, E. A. (2020). Quantifying the
826 influence of cloud radiative feedbacks on Arctic surface warming using cloud locking in an Earth
827 system model. *Geophysical Research Letters*, 47, e2020GL089207.
828 <https://doi.org/10.1029/2020GL089207>

829

830 Morrison, H., de Boer, G., Feingold, G., Harrington, J., Shupe, M. D. & Sulia, K. (2012).
831 Resilience of persistent Arctic mixed-phase clouds. *Nature Geoscience*, 5, 11–17.
832 <https://doi.org/10.1038/ngeo1332>

833

834 Morrison, H., van Lier-Walqui, M., Fridlind, A. M., Grabowski, W. W., Harrington, J. Y.,
835 Hoose, C., et al. (2020). Confronting the challenge of modeling cloud and precipitation
836 microphysics. *Journal of Advances in Modeling Earth Systems*, 12, e2019MS001689.
837 <https://doi.org/10.1029/2019MS001689>

838

839 Nicolas, J. P., Vogelmann, A. M., Scott, R. C., Wilson, A. B., Cadeddu, M. P., Bromwich, D. H.,
840 et al. (2017). January 2016 extensive summer melt in West Antarctica favoured by strong El
841 Niño. *Nature Communications*, 8(1), 15,799. <https://doi.org/10.1038/ncomms15799>

842

843 Ovchinnikov, M., Ackerman, A. S., Avramov, A., Cheng, A., Fan, J., Fridlind, A. M., et al.
844 (2014). Intercomparison of large-eddy simulations of Arctic mixed-phase clouds: Importance of
845 ice size distribution assumptions. *Journal of Advances in Modeling Earth Systems*, 6, 223–248.
846 <https://doi.org/10.1002/2013MS000282>

847

848 Rasch, P. J., Xie, S., Ma, P.-L., Lin, W., Wang, H., Tang, Q., et al. (2019). An overview of the
849 atmospheric component of the Energy Exascale Earth System Model. *Journal of Advances in*
850 *Modeling Earth Systems*, 11, 2377–2411. <https://doi.org/10.1029/2019MS001629>

851

852 Shupe, M. D., Walden, V. P., Eloranta, E., Uttal, T., Campbell, J. R., Starkweather, S. M., &
853 Shiobara, M. (2011). Clouds at Arctic Atmospheric Observatories. Part I: Occurrence and
854 Macrophysical Properties. *Journal of Applied Meteorology and Climatology*, 50(3), 626–644.
855 <https://doi.org/10.1175/2010JAMC2467.1>

856

857 Silber, I., Verlinde, J., Eloranta, E. W., & Cadetdu, M. (2018). Antarctic cloud macrophysical,
858 thermodynamic phase, and atmospheric inversion coupling properties at McMurdo Station: I.
859 Principal data processing and climatology. *Journal of Geophysical Research: Atmospheres*, 123,
860 6099–6121. <https://doi.org/10.1029/2018JD028279>

861

862 Sun, J., Zhang, K., Wan, H., Ma, P.-L., Tang, Q., & Zhang, S. (2019). Impact of nudging
863 strategy on the climate representativeness and hindcast skill of constrained EAMv1 simulations.

864 *Journal of Advances in Modeling Earth Systems*, 11, 3911– 3933.

865 <https://doi.org/10.1029/2019MS001831>

866

867 Sun, Z. & Shine, K. P. (1994). Studies of the radiative properties of ice and mixed-phase clouds.

868 *Quarterly Journal of the Royal Meteorological Society*, 120, 111–137.

869 <https://doi.org/10.1002/qj.49712051508>

870

871 Sun, Z., & Shine, K. P. (1995). Parameterization of Ice Cloud Radiative Properties and Its

872 Application to the Potential Climatic Importance of Mixed-Phase Clouds. *Journal of Climate*,

873 8(7), 1874-1888. [https://doi.org/10.1175/1520-0442\(1995\)008<1874:POICRP>2.0.CO;2](https://doi.org/10.1175/1520-0442(1995)008<1874:POICRP>2.0.CO;2)

874

875 Tan, I., Barahona, D., & Coopman, Q. (2022). Potential link between ice nucleation and climate

876 model spread in Arctic amplification. *Geophysical Research Letters*, 49, e2021GL097373.

877 <https://doi.org/10.1029/2021GL097373>

878

879 Tan, I., & Storelvmo, T. (2019). Evidence of strong contributions from mixed-phase clouds to

880 Arctic climate change. *Geophysical Research Letters*, 46, 2894–2902.

881 <https://doi.org/10.1029/2018GL081871>

882

883 Tan, I., Storelvmo, T., & Choi, Y.-S. (2014). Spaceborne lidar observations of the ice-nucleating

884 potential of dust, polluted dust and smoke aerosols in mixed-phase clouds. *Journal of*

885 *Geophysical Research: Atmospheres*, 119, 6653–6665, <https://doi.org/10.1002/2013JD021333>

886

887 Tan, I., Storelvmo, T., & Zelinka, M. D. (2016). Observational constraints on mixed-phase
888 clouds imply higher climate sensitivity. *Science*, 352, 224–227.

889 <https://doi.org/10.1126/science.aad5300>

890

891 Tang, Q., Prather, M. J., Hsu, J., Ruiz, D. J., Cameron-Smith, P. J., Xie, S., & Golaz, J.-C.

892 (2021). Evaluation of the interactive stratospheric ozone (O3v2) module in the E3SM version 1

893 Earth system model, *Geoscientific Model Development*, 14, 1219–1236.

894 <https://doi.org/10.5194/gmd-14-1219-2021>

895

896 Verlinde, J., Zak, B. D., Shupe, M. D., Ivey, M. D., & Stamnes, K. (2016). The ARM North

897 Slope of Alaska (NSA) Sites. *Meteorological Monographs*, 57, 8.1-

898 8.13. <https://doi.org/10.1175/AMSMONOGRAPHS-D-15-0023.1>

899

900 Villanueva, D., Senf, F., & Tegen, I. (2021). Hemispheric and seasonal contrast in cloud

901 thermodynamic phase from A-Train spaceborne instruments. *Journal of Geophysical Research:*

902 *Atmospheres*, 126, e2020JD034322. <https://doi.org/10.1029/2020JD034322>

903

904 Wang, H., Easter, R. C., Zhang, R., Ma, P.-L., Singh, B., Zhang, K., et al. (2020). Aerosols in the

905 E3SM Version 1: New developments and their impacts on radiative forcing. *Journal of Advances*

906 *in Modeling Earth Systems*, 12, e2019MS001851. <https://doi.org/10.1029/2019MS001851>

907

- 908 Wang, Y., Liu, X., Hoose, C., & Wang, B. (2014). Different contact angle distributions for
909 heterogeneous ice nucleation in the Community Atmospheric Model version 5. *Atmospheric*
910 *Chemistry and Physics*, 14, 10411–10430. <https://doi.org/10.5194/acp-14-10411-2014>
911
- 912 Xie, S., Klein, S. A., Yio, J. J., Beljaars, A. C. M., Long, C. N., & Zhang, M. (2006). An
913 assessment of ECMWF analyses and model forecasts over the North Slope of Alaska using
914 observations from the ARM Mixed-Phase Arctic Cloud Experiment. *Journal of Geophysical*
915 *Research: Atmospheres*. 111, D05107. <https://doi.org/10.1029/2005JD006509>
916
- 917 Xie, S., Lin, W., Rasch, P. J., Ma, P.-L., Neale, R., Larson, V. E., et al. (2018). Understanding
918 cloud and convective characteristics in version 1 of the E3SM atmosphere model. *Journal of*
919 *Advances in Modeling Earth Systems*, 10, 2618–2644. <https://doi.org/10.1029/2018MS001350>
920
- 921 Xie, S., McCoy, R. B., Klein, S. A., Cederwall, R. T., Wiscombe, W. J., Jensen, M. P., et al.
922 (2010). CLOUDS AND MORE: ARM Climate Modeling Best Estimate Data. *Bulletin of the*
923 *American Meteorological Society*, 91(1), 13–20. <https://doi.org/10.1175/2009BAMS2891.1>
924
- 925 Xie, S., Wang, Y.-C., Lin, W., Ma, H.-Y., Tang, Q., Tang, S., et al. (2019). Improved diurnal
926 cycle of precipitation in E3SM with a revised convective triggering function. *Journal of*
927 *Advances in Modeling Earth Systems*, 11. <https://doi.org/10.1029/2019MS001702>
928
- 929 Yang, C. A., Diao, M., Gettelman, A., Zhang, K., Sun, J., McFarquhar, G., & Wu, W. (2021). Ice
930 and supercooled liquid water distributions over the Southern Ocean based on in situ observations

931 and climate model simulations. *Journal of Geophysical Research: Atmospheres*, 126,
932 e2021JD036045. <https://doi.org/10.1029/2021JD036045>
933
934 Yip, J., Diao, M., Barone, T., Silber, I., & Gettelman, A. (2021). Evaluation of the CAM6
935 climate model using cloud observations at McMurdo Station, Antarctica. *Journal of Geophysical*
936 *Research: Atmospheres*, 126, e2021JD034653. <https://doi.org/10.1029/2021JD034653>
937
938 Zelinka, M. D., Myers, T. A., McCoy, D. T., Po-Chedley, S., Caldwell, P. M., Ceppi, P., et al.
939 (2020). Causes of higher climate sensitivity in CMIP6 models. *Geophysical Research Letters*,
940 47, e2019GL085782. <https://doi.org/10.1029/2019GL085782>
941
942 Zhang, C., Xie, S., Tao, C., Tang, S., Emmenegger, T., Neelin, J. D., et al. (2020). The ARM
943 Data-Oriented Metrics and Diagnostics Package for Climate Models: A New Tool for Evaluating
944 Climate Models with Field Data, *Bulletin of the American Meteorological Society*, 101(10),
945 E1619-E1627. <https://doi.org/10.1175/BAMS-D-19-0282.1>
946
947 Zhang, D., Wang, Z., Kollias, P., Vogelmann, A. M., Yang, K., & Luo, T. (2018). Ice particle
948 production in mid-level stratiform mixed-phase clouds observed with collocated A-Train
949 measurements. *Atmospheric Chemistry and Physics*, 18, 4317–4327. [https://doi.org/10.5194/acp-](https://doi.org/10.5194/acp-18-4317-2018)
950 [18-4317-2018](https://doi.org/10.5194/acp-18-4317-2018)
951
952 Zhang, D., Vogelmann, A., Kollias, P., Luke, E., Yang, F., Lubin, D., & Wang, Z. (2019).
953 Comparison of Antarctic and Arctic single-layer stratiform mixed-phase cloud properties using

954 ground-based remote sensing measurements. *Journal of Geophysical Research: Atmospheres*,
955 124. <https://doi.org/10.1029/2019JD030673>

956

957 Zhang, G. J., & McFarlane, N. A. (1995). Sensitivity of climate simulations to the
958 parameterization of cumulus convection in the Canadian climate centre general circulation
959 model. *Atmosphere-Ocean*, 33(3), 407–446. <https://doi.org/10.1080/07055900.1995.9649539>

960

961 Zhang, K., Wan, H., Liu, X., Ghan, S. J., Kooperman, G. J., Ma, P.-L., et al. (2014). Technical
962 Note: On the use of nudging for aerosol–climate model intercomparison studies. *Atmospheric*
963 *Chemistry and Physics*, 14, 8631–8645. <https://doi.org/10.5194/acp-14-8631-2014>

964

965 Zhang, K., Zhang, W., Wan, H., Rasch, P. J., Ghan, S. J., Easter, R. C., et al. (2022). Effective
966 radiative forcing of anthropogenic aerosols in E3SM version 1: historical changes, causality,
967 decomposition, and parameterization sensitivities. *Atmospheric Chemistry and Physics*, 22,
968 9129–9160. <https://doi.org/10.5194/acp-22-9129-2022>

969

970 Zhang, M., Xie, S., Liu, X., Lin, W., Zhang, K., Ma, H.-Y., et al. (2020). Toward understanding
971 the simulated phase partitioning of arctic single-layer mixed-phase clouds in E3SM. *Earth and*
972 *Space Science*, 7, e2020EA001125. <https://doi.org/10.1029/2020EA001125>

973

974 Zhang, M., Xie, S., Liu, X., Lin, W., Zheng, X., Golaz, J.-C., & Zhang, Y. (2022). Cloud Phase
975 Simulation at High Latitudes in EAMv2: Evaluation using CALIPSO Observations and

976 Comparison with EAMv1. *Journal of Geophysical Research: Atmospheres*, 127,
977 e2022JD037100. <https://doi.org/10.1029/2022JD037100>

978

979 Zhang, Y., Xie, S., Lin, W., Klein, S. A., Zelinka, M., Ma, P.-L., et al. (2019). Evaluation of
980 clouds in version 1 of the E3SM atmosphere model with satellite simulators. *Journal of*
981 *Advances in Modeling Earth Systems*, 11. <https://doi.org/10.1029/2018MS001562>

982

983 Zhao, C., Xie, S., Klein, S. A., Protat, A., Shupe, M. D., McFarlane, S. A., et al. (2012). Toward
984 understanding of differences in current cloud retrievals of ARM ground-based measurements.
985 *Journal of Geophysical Research: Atmospheres*, 117, D10206.

986 <https://doi.org/10.1029/2011JD016792>

987

988 Zhao, X., & Liu, X. (2021). Global importance of secondary ice production. *Geophysical*
989 *Research Letters*, 48, e2021GL092581. <https://doi.org/10.1029/2021GL092581>

990

991 Zhao, X., & Liu, X. (2022). Primary and secondary ice production: interactions and their relative
992 importance. *Atmospheric Chemistry and Physics*, 22, 2585–2600. [https://doi.org/10.5194/acp-22-](https://doi.org/10.5194/acp-22-2585-2022)
993 [2585-2022](https://doi.org/10.5194/acp-22-2585-2022)

994

995 Zhao, X., Liu, X., Phillips, V. T. J., & Patade, S. (2021). Impacts of secondary ice production on
996 Arctic mixed-phase clouds based on ARM observations and CAM6 single-column model
997 simulations. *Atmospheric Chemistry and Physics*, 21, 5685–5703. [https://doi.org/10.5194/acp-](https://doi.org/10.5194/acp-21-5685-2021)
998 [21-5685-2021](https://doi.org/10.5194/acp-21-5685-2021)

1 **Evaluating EAMv2 simulated stratiform mixed-phase cloud properties at Northern and**
2 **Southern high latitudes against ARM measurements**

3
4 Meng Zhang¹, Shaocheng Xie¹, Xiaohong Liu², Damao Zhang³, Wuyin Lin⁴, Kai Zhang³,
5 Jean-Christophe Golaz¹, Xue Zheng¹, Yuying Zhang¹

6
7 ¹ Lawrence Livermore National Laboratory, Livermore, CA, USA

8 ² Department of Atmospheric Sciences, Texas A&M University, College Station, Texas, USA

9 ³ Pacific Northwest National Laboratory, Richland, WA, USA

10 ⁴ Brookhaven National Laboratory, Upton, NY, USA

11
12 Corresponding author: Meng Zhang, zhang55@llnl.gov

13
14
15 Key points:

- 16 • Stratiform mixed-phase clouds simulated from nudged EAMv2 simulation are evaluated
17 with ARM ground-based remote sensing retrievals.
- 18 • Cloud macrophysics and their hemispheric difference are better simulated than cloud
19 phase.
- 20 • Cloud phase is largely biased, with underestimated ice water path at the NSA site and
21 underestimated liquid water path at the AWR site.
- 22
23

24
25
26
27
28
29
30
31
32
33
34
35
36
37
38
39
40
41
42
43
44
45
46

Abstract

This study evaluates high-latitude stratiform mixed-phase clouds (SMPC) in the atmosphere model of the newly released Energy Exascale Earth System Model version 2 (EAMv2) by utilizing one-year-long ground-based remote sensing measurements from the U.S. Department of Energy Atmospheric Radiation and Measurement (ARM) Program. A nudging approach is applied to model simulations for a better comparison with the ARM observations. Observed and modeled SMPCs are collocated to evaluate their macro- and microphysical properties at the ARM North Slope of Alaska (NSA) site in the Arctic and the McMurdo (AWR) site in the Antarctic. We found that EAMv2 overestimates (underestimates) SMPC frequency of occurrence at the NSA (AWR) site nearly all year round. However, the model captures the observed larger cloud frequency of occurrence at the NSA site. For collocated SMPCs, the annual statistics of observed cloud macrophysics are generally reproduced at the NSA site, while at the AWR site, there are larger biases. Compared to the AWR site, the lower cloud boundaries and the warmer cloud top temperature observed at NSA are well simulated. On the other hand, simulated cloud phases are substantially biased at each location. The model largely overestimates liquid water path at NSA, whereas it is frequently underestimated at AWR. Meanwhile, the simulated ice water path is underestimated at NSA, but at AWR, it is comparable to observations. As a result, the observed hemispheric difference in cloud phase partitioning is misrepresented in EAMv2. This study implies that continuous improvement in cloud microphysics is needed for high-latitude mixed-phase clouds.

47 **1. Introduction**

48 For decades, mixed-phase clouds that consist of both liquid droplets and ice crystals at
49 temperatures between 0 and -40°C have been ubiquitously observed at high latitudes in both
50 hemispheres (Korolev et al., 2017; McFarquar et al., 2021; Shupe et al., 2011; Zhang et al.,
51 2018). Mixed-phase clouds can impact the regional and global climate by modulating the energy
52 budget at the surface and the top of the atmosphere. Partitioning of cloud liquid and ice is critical
53 for the radiative effect of mixed-phase clouds, which is manifested by the significant difference
54 in optical properties between liquid droplets and ice particles (Curry et al., 1996; Sun & Shine,
55 1994; 1995; Gregory & Morris, 1996). By parameterizing the distinct optical properties of liquid
56 and ice water in general circulation models (GCMs), the simulated cloud phase has been
57 demonstrated to be one of the key factors influencing the predicted future climate (Lohmann &
58 Neubauer, 2018; McCoy et al., 2015). Tan et al. (2016) constrained the model simulated cloud
59 phase using satellite observations to correct the low bias of supercooled liquid fraction (SLF) in
60 the Community Atmosphere Model version 5.1 (CAM5.1), which results in an increase of the
61 equilibrium climate sensitivity (ECS) by 1.3°C compared to the default model. The higher ECS
62 mainly results from the reduced negative cloud phase feedback at high latitudes. Furthermore,
63 the magnitude of Arctic amplification is found to have a considerable sensitivity to the relative
64 abundance of cloud liquid and ice in high-latitude mixed-phase clouds (Middlemas et al., 2020;
65 Tan & Storelvmo, 2019; Tan et al., 2022).

66 However, significant uncertainties exist in the simulated cloud properties of high-latitude
67 mixed-phase clouds, including cloud phase partitioning. The challenges are mainly attributable
68 to the parameterization of unresolved subgrid-scale cloud processes and the gap in fundamental
69 process-level understanding of cloud microphysics (Morrison et al., 2020). Among a variety of

70 GCMs that participate in the Coupled Model Intercomparison Project Phase 5 and Phase 6
71 (CMIP5 and CMIP6), the model predicted cloud phase and associated cloud feedbacks are highly
72 sensitive to the treatments of cloud microphysics (McCoy et al., 2015, 2016; Zelinka et al., 2020;
73 Gettelman et al., 2019). Yip et al. (2021) evaluated the simulated cloud properties from the
74 Community Atmosphere Model version 6 (CAM6) against the remote sensing retrievals during
75 the U.S. Department of Energy (DOE) Atmospheric Radiation Measurement (ARM) West
76 Antarctic Radiation Experiment (AWARE) field campaign. They found that CAM6 largely
77 overestimates cloud fraction above and underestimates it below 3 km. Liquid phase clouds are
78 overestimated, and ice and mixed-phase clouds are underestimated when cloud fraction exceeds
79 0.6. Cloud fraction biases are found to be closely related to the biases in simulated relative
80 humidity and water vapor. Cloud ice water simulated by the U.S. DOE Energy Exascale Earth
81 System Model (E3SM) Atmosphere Model version 1 (EAMv1) was also underestimated, and
82 cloud liquid water was overestimated when compared to the Cloud-Aerosol Lidar and Infrared
83 Pathfinder Satellite Observation (CALIPSO) satellite observations (Y. Zhang et al., 2019) and
84 ARM Mixed-Phase Arctic Cloud Experiment (M-PACE) field campaign data (M. Zhang et al.,
85 2020). Compared with in situ airborne observations from the Southern Ocean Clouds, Radiation,
86 Aerosol Transport Experimental Study (SOCRATES) campaign, Yang et al. (2021) found that
87 both CAM6 and E3SMv1 overestimate cloud liquid and underestimate cloud ice occurrences at
88 temperatures colder than -20°C .

89 Due to the limitations and uncertainties in different instruments and retrieval algorithms,
90 cloud property retrievals used in model validations can vary significantly (Zhao et al., 2012).
91 McErlich et al. (2021) compared the cloud occurrence retrievals from the 2B-CLDCLASS-
92 LIDAR R05 (2BCL5) and the radar/liDAR (DARDAR) satellite products with ground-based

93 measurements during the AWARE field campaign. They found that the 2BCL5 and DARDAR
94 satellite retrievals underestimate cloud occurrence at altitudes lower than 1.5 km, while the
95 AWARE ground-based observations underestimate cloud occurrence higher than 6 km. Liu et al.
96 (2017) also showed that space-borne observations, such as the 2B-GEOPROF-lidar, detect 25%-
97 40% fewer clouds than ground-based lidar below 0.5 km. The discrepancies between satellite-
98 and ground-based retrievals of cloud occurrence are mainly attributed to the attenuation of lidar
99 or radar beams or the uncertainties in retrieval algorithms. The difference between active and
100 passive sensors also contributes to the disagreements between different satellite products. For
101 example, Villanueva et al. (2021) utilized the CALIPSO-GOCCP (GCM-Oriented Cloud Calipso
102 Product), DARDAR, and PM-L2 (MODIS, MODERate resolution Imaging Spectroradiometer,
103 and PARASOL combined product) cloud top phase products to examine the hemispheric contrast
104 in observed cloud phase. The disagreement in the retrieval of ice phase frequency is noticeable
105 among different products, which is mainly caused by the retrieval issues and the limited
106 capability of different instruments in detecting ice particles and liquid droplets. They further
107 suggested that the cloud top phase from the combination of three cloud products is more reliable
108 than individual products when estimating the cloud phase hemispheric difference. Therefore, it is
109 important to understand the uncertainties in observational datasets and, if necessary, utilize
110 different products with complementary capabilities in retrievals when applying them in the
111 model evaluation.

112 In an earlier evaluation of the high-latitude cloud phase in version 2 of the E3SM
113 atmosphere model (EAMv2), M. Zhang et al. (2022) compared model simulated cloud properties
114 from the CALIPSO simulator in EAMv2 with the CALIPSO-GOCCP product. However, like
115 other satellite retrievals, CALIPSO-GOCCP also suffers from the limited capability of detecting

116 low-level clouds and precipitation. Such limitations make the thorough evaluation of cloud
117 properties at high latitudes difficult, considering that precipitating ice is common for high-
118 latitude mixed-phase clouds. In the past years, the ARM program performed multi-year long-
119 term ground-based measurements at the North Slope of Alaska (NSA, Utqiagvik in the Arctic).
120 In 2016, comprehensive ground-based instruments were also deployed at the McMurdo station
121 (AWR, in the Antarctic) to conduct one-year-long measurements during the AWARE field
122 campaign (Lubin et al., 2020; Verlinde et al., 2016). These ARM measurements complement the
123 satellite retrievals and provide reliable and robust atmospheric states, cloud, and precipitation
124 observations at high latitudes, which have been applied in many model evaluation studies (Klein
125 et al., 2009; Ovchinnikov et al., 2014; C. Zhang., 2020).

126 This study aims to evaluate mixed-phase cloud properties from EAMv2 using ARM
127 retrievals at the NSA and AWR sites. Previous studies showed that cloud properties retrieved at
128 the NSA and AWR can largely differ, especially for cloud occurrence, cloud height, and cloud
129 thickness (Lubin et al., 2020; Silber et al., 2018). D. Zhang et al. (2019) illustrated that stratiform
130 mixed-phase clouds (SMPCs, hereafter) at the AWR site can have larger SLF than those at the
131 NSA site for a given temperature between -24°C and -14°C . The larger SLF in the Antarctic is
132 mainly because of the lower ice water path (IWP) compared to the Arctic, while a comparable
133 liquid water path (LWP) is found at that temperature range. Thus, one emphasis of this study is
134 to evaluate whether EAMv2 can simulate the observed hemispheric difference in mixed-phase
135 cloud properties shown in the ARM observations. A novel comparison method is applied in this
136 study to focus only on high-latitude SMPCs. The merit of this method is that the target SMPCs
137 are defined consistently in the model simulation and ARM observation.

138 The paper is organized as follows: section 2 describes the EAMv2 model and model
139 experiments. Section 3 introduces the ARM observational data and retrievals of analyzed SMPC
140 properties. An innovative comparison approach between EAMv2 and ARM data is presented in
141 section 4. Section 5 discusses the comparison results between modeled and observed SMPCs,
142 and the conclusions are summarized in section 6.

143

144 **2. Model Description and Experiments**

145 **2.1. EAMv2 Model**

146 The recently released EAMv2 model is evaluated in this study. Different from EAMv1
147 (Rasch et al., 2019, Xie et al., 2018), EAMv2 runs on a spectral finite element dynamical core
148 with a semi-Lagrangian passive tracer transport method (Bradley et al., 2021). As introduced by
149 Hannah et al. (2021), the parameterized physics and dynamics use separate grids. The dynamics
150 grid has an average grid spacing of 110 km, while the physics grid has an average grid spacing of
151 165 km. In the vertical, it keeps the same 72 vertical layers with a model top at ~ 0.1 hPa as
152 EAMv1. For atmospheric physics, the major changes include a new convective trigger described
153 in Xie et al. (2019) incorporated in the deep convection scheme (Zhang & McFarlane, 1995) to
154 improve the simulation of precipitation and its diurnal cycle. A convective gustiness scheme for
155 subgrid gustiness enhancement is incorporated in EAMv2 to improve the surface exchanges of
156 heat, moisture, and momentum and the representation of tropical clouds and precipitation
157 (Harrop et al., 2018; Ma et al., 2022). EAMv2 also updates the linearized chemistry for
158 stratospheric ozone (Tang et al., 2021) to preserve the sharp cross-tropopause gradient and
159 improve the stratosphere-troposphere exchange flux of ozone. The parameterizations for other
160 processes remain the same as those used in EAMv1. They include the Cloud Layers Unified By

161 Binormals (CLUBB) parameterization (Golaz et al., 2002; Larson, 2017) for subgrid turbulent
162 transport and cloud macrophysics, the second version of Morrison and Gettelman (MG2) cloud
163 microphysics scheme (Gettelman & Morrison, 2014), the Classical Nucleation Theory (CNT)
164 based heterogeneous ice nucleation scheme for mixed-phase clouds (Hoose et al., 2010; Wang et
165 al., 2014), and the four-mode version of the Modal Aerosol Module (MAM4) (Liu et al., 2012,
166 2016; Wang et al., 2020). Following Ma et al. (2022), several tuning parameters in cloud
167 microphysics, CLUBB, and deep convection are recalibrated to improve the cloud and
168 precipitation simulations. More details about the EAMv2 model can be found in the overview
169 paper of Golaz et al. (2022).

170

171 **2.2. Model Experiments**

172 The EAMv2 simulations are run with the nudging approach following Sun et al. (2019).
173 The nudging helps to constrain the simulated large-scale circulation with reanalysis data so that
174 the synoptic weather events observed during ARM field campaigns can be well captured by
175 nudged simulations (Zhang et al., 2014). With more realistic state variables in our model
176 simulation, we can thus collocate simulated clouds to the measured clouds and then examine the
177 differences between the model and observation at the NSA and AWR sites.

178 In this study, the horizontal wind (U, V) and temperature (T) fields are nudged toward
179 ERA-Interim reanalysis data for 2016 starting from 1st November 2015, with a nudging
180 relaxation time scale of 6 hours. Sea surface temperature and sea ice are prescribed with
181 observed data. Model simulations of the first two months are discarded as the spin-up, and model
182 results for 2016 are evaluated against the ARM SMPC retrievals. EAMv2 results are output
183 every 30 minutes. The model grids that are closest to the NSA site (71°19'22.8" N, 156°36'54"

184 W) and AWR site (77°50'47" S, 166°40'06" E) are used for analysis. Note that the chosen model
185 grid near the NSA represents the coastal environment, and the grid near the AWR is over the
186 ocean. The influence of land and ocean grids on simulated cloud properties has been examined
187 by comparing neighboring grids points, and it has minimal impact on our evaluations (not
188 shown).

189

190 **3. ARM Observations**

191 Over the past three decades, the U.S. DOE ARM program has established long-term
192 observations of cloud, radiation, and large-scale environment at several ARM observation sites.
193 This study utilizes the ARM ground-based remote sensing data at the NSA and AWR sites in
194 2016 to evaluate EAMv2 simulated mixed-phase cloud properties. During that year, the ARM
195 program launched the AWARE field campaign over the West Antarctic Ice Sheet (WAIS) to
196 understand the rapid climate change in the remote Antarctic region. The second ARM Mobile
197 Facility (AMF2), including cloud radar, high spectral resolution lidar, laser ceilometer,
198 microwave radiometer, etc., was deployed at the AWR site from 1 December 2015 to 31
199 December 2016. Measurements with the same suite of instruments were also available at the
200 NSA site in 2016. This allows us to compare the simulated cloud properties between the Arctic
201 and Antarctic sites to examine if the model can reproduce the observed hemispheric differences
202 in cloud properties for similar types of mixed-phase clouds. Detailed descriptions of instruments,
203 meteorological conditions, and summaries of cloud and aerosol measurements at the NSA and
204 AWR sites are presented in Verlinde et al. (2016) and Lubin et al. (2020), respectively.

205 For observed SMPCs, we use: (1) the high spectral resolution lidar (HSRL) and Ka-band
206 ARM zenith radar (KAZR) measurements in cloud structure detections and cloud property

207 retrievals; (2) the ARM INTERPSONDE value-added product (VAP,
 208 <https://www.arm.gov/capabilities/vaps/interpsonde>) for atmosphere environmental conditions
 209 including pressure, temperature, water vapor, and relative humidity; and (3) the ARM MWRRET
 210 VAP (<https://www.arm.gov/capabilities/vaps/mwrret>) for cloud LWP. Stratiform mixed-phase
 211 identification and cloud macrophysical and microphysical property retrievals are described in
 212 detail by D. Zhang et al. (2019, DZ19 hereafter). In short, the liquid-dominated layer at the cloud
 213 top is determined from the HSRL backscatter coefficient gradient and depolarization profiles,
 214 while the ice virga is detected by the KAZR reflectivity (Z_e). Cloud top and cloud base heights
 215 and associated cloud layer temperature can then be derived. For ice phase microphysical
 216 properties, the ice water content (IWC) profile is retrieved using the IWC-Z (radar reflectivity
 217 factor) and temperature relationships following Hogan et al. (2006). The IWP is derived by
 218 integrating IWC from the cloud base to the cloud top. For liquid phase microphysical properties,
 219 LWP is obtained from the ARM MWRRET VAP.

220 Note that SMPC boundaries determined with the KAZR and HSRL measurements alone
 221 are dominated by liquid water in DZ19. In particular, the identified cloud base is the base of
 222 liquid dominated layer. However, with precipitating ice hydrometeors frequently observed in
 223 high-latitude SMPCs (Morrison et al., 2012), such cloud boundaries are not accurate, and thus
 224 they are not used in this study. Instead, the retrieval of the vertical distribution of cloud
 225 hydrometeors based on the combined measurements of cloud radar, lidar, and laser ceilometer
 226 from the Active Remote Sensing of Clouds (ARSCL) algorithm (Clothiaux et al., 2000) is used
 227 in the evaluation since the ARSCL algorithm can more accurately determine the cloud base with
 228 precipitating ice included (Clothiaux et al., 2000). Meanwhile, the model calculated cloud
 229 vertical distribution also contains layers of ice hydrometeors, consistent with the ARSCL cloud

230 boundary. Therefore, we use the ARSCL retrievals of identified SMPCs to evaluate modeled
 231 cloud boundary properties. Given the common nature of liquid-dominated cloud top in high-
 232 latitude SMPCs, the cloud top retrieved from the ARSCL algorithm and the cloud top of liquid-
 233 dominated layer in DZ19 are overall comparable with each other (not shown). Furthermore,
 234 because cloud properties can largely influence the surface energy budget, surface radiative fluxes
 235 in the ARM Best Estimate product (ARMBE, Xie et al., 2010) are also used to evaluate modeled
 236 cloud radiative effects at the NSA and AWR sites. Table 1 summarizes all the observational data
 237 used in the current model evaluation.

238

239 Table 1. *Summary of Cloud Properties Derived from ARM Measurements.*

Cloud Property	Instrument and Retrieval Method
Cloud top height (CTH)	Cloud boundaries detected with KAZR, MPL, and laser ceilometer from the Active Remote Sensing of Clouds Products using KAZR (KAZRARSCl) VAP (https://www.arm.gov/capabilities/vaps/kazrarscl)
Cloud base height (CBH)	
Cloud thickness (THK)	
Cloud top temperature (CTT)	Using temperature profiles from the ARM INTERPSONDE VAP and KAZRARSCl CTH
Liquid water path (LWP)	From the ARM MWRRET VAP
Ice water path (IWP)	Integrating ice water content (IWC) retrieved using the IWC-Z-T relationship from CBH to CTH (Hogan et al., 2006)
Surface radiative fluxes	From ARMBE VAP (Xie et al., 2010)

240

241

242 4. Evaluation Method

243 An innovative approach is utilized in this study to evaluate EAMv2 simulated cloud
 244 properties against ARM ground-based remote sensing retrievals. The idea behind this approach

245 is to select model simulated clouds with the similar characteristics to those retrieved in DZ19. By
246 doing so, we can consistently compare the properties of the same type of SMPC and thus avoid
247 error and ambiguity in cloud evaluation due to the inconsistent definitions between the model
248 and observation. As SMPCs are prevalent in the Arctic and Antarctic regions and are the focus of
249 DZ19, our sampling also targets SMPCs in the model simulation. We define the target SMPCs
250 by the following criteria: (1) Simulated cloud fraction is greater than 5% to define cloudy
251 conditions; (2) Cloud top temperature is within 0 – -40°C range to ensure a supercooled
252 environment that is suitable for mixed-phase clouds; and (3) If multi-layer clouds exist and also
253 the distance between multiple cloud layers is greater than 2 km, we assume the seeding effect
254 does not affect the lower cloud layer. Thus, we keep the lower cloud layer to exclude the seeding
255 effect from the upper cloud layers. Note that the third criterion is the same as that used in DZ19.
256 Such a criterion not only increases the data amount of SMPC compared to that of single-layer
257 mixed-phase clouds but also keeps the relatively simple structures in the examined clouds, which
258 increases the statistical significance of our data analysis. Although the target cloud samples share
259 similar definitions between the model and observation, inconsistencies cannot be removed
260 entirely in the comparison. For example, given the high temporal resolution (30 s) of ground-
261 based remote sensing instruments (i.e., KAZR and HSRL), stratiform cloud systems are
262 identified if cloud top heights show little variability with standard deviations smaller than 300 m.
263 However, the same criterion is inapplicable to model outputs with the 30-minute time step.
264 Therefore, we assume that the simulated grid-mean clouds are all stratiform if they meet the
265 aforementioned criteria. Meanwhile, we consider vertically continuous cloud layers as the same
266 cloud system in the model. The calculation of cloud properties is then for cloud systems
267 extending over several model vertical layers. We also note that the number of defined SMPC

268 from EAMv2 varies by about 5% if we modify the chosen thresholds of cloud fraction (i.e., 5%
269 changing to 1% or 10%) and the distance between multiple cloud layers (i.e., 2 km changing to
270 1.5 km or 3 km) used in the sampling, which does not significantly affect the evaluation.

271 To further evaluate the SMPC properties in EAMv2, the 30-second retrievals of DZ19 are
272 averaged to the one-hour temporal resolution. The choice of hourly resolution is for consistency
273 with the highest temporal resolution available in the ARMBE product. We also tested the
274 temporal resolution of 30 minutes for ARM data and compared it with the model results. We
275 found that the SMPC data sampling is nearly doubled compared to the one-hour resolution, but
276 the observed cloud properties are generally insensitive to the temporal resolution change.
277 Therefore, the case-by-case examinations of cloud structures and microphysical properties are
278 performed using hourly observations and model outputs (i.e., averaged from 30-minute outputs).

279 Since the selected SMPC samples from the model and observation do not necessarily
280 occur at the same time in 2016, a collocation approach is used to further determine the times
281 when both the model and observation have SMPCs. We collocate the model and observation by
282 comparing the time series of hourly simulated and observed clouds. If SMPCs appear in both the
283 model and observation, we consider the SMPC in this hour is collocated. The collocation allows
284 a case-by-case comparison of SMPC properties between the model and observation. The
285 collocation also links the simulated cloud radiative properties to other ARM measurements for
286 each pair of model and observational data, which benefits the examination of the impact of
287 biased cloud properties on cloud radiative effects. This approach is applied to both the NSA and
288 AWR sites for evaluation purposes.

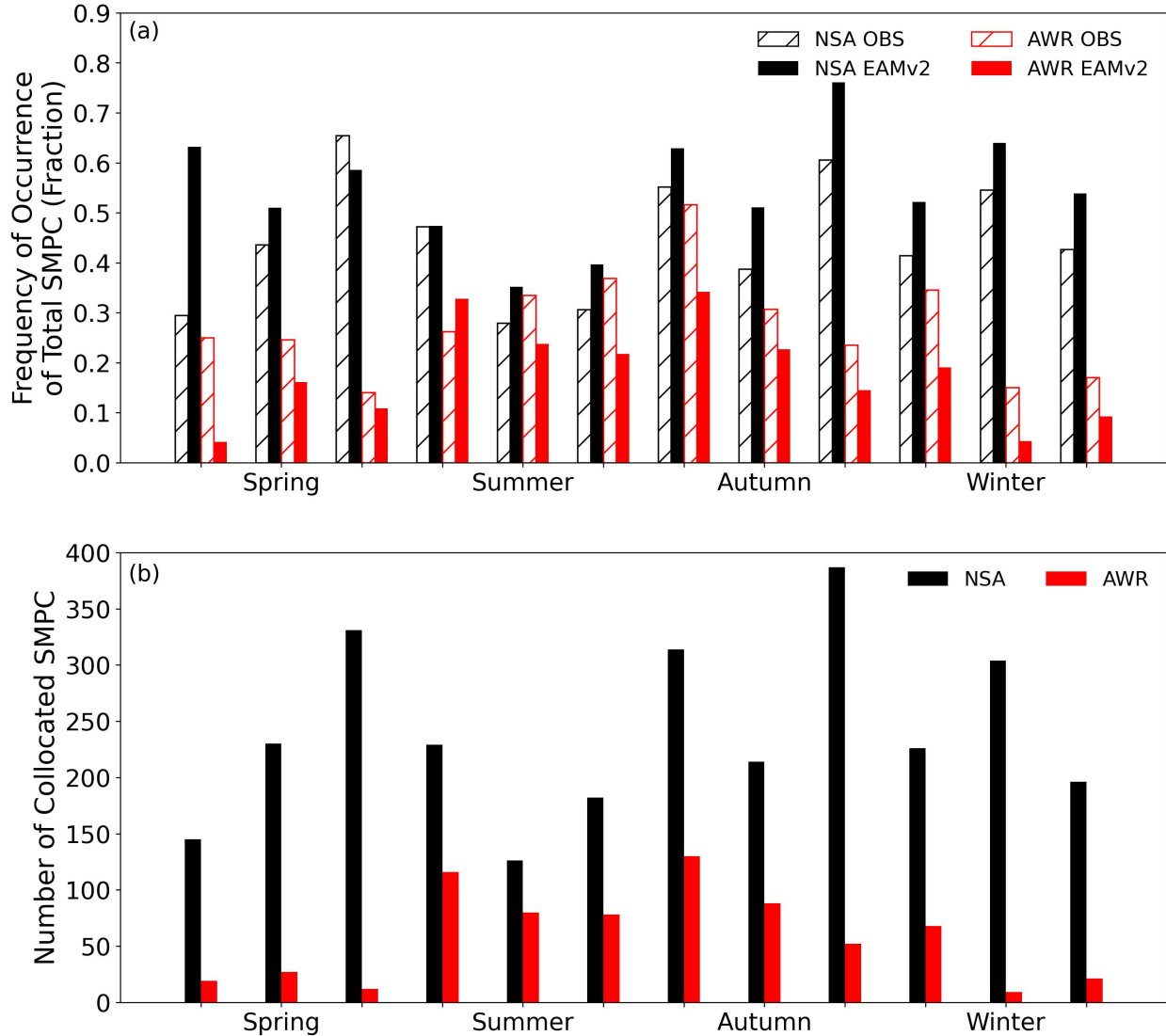
289

290 **5. Results**

291 **5.1. Cloud Occurrence**

292 We first examine the general model behavior in simulating SMPCs during 2016. Figure 1
293 compares the frequency of occurrence of total SMPC samples in EAMv2 with DZ19 at NSA and
294 AWR sites. The monthly frequency of occurrence of SMPC is grouped into four seasons
295 according to their respective months so that the monthly comparison is in phase between two
296 hemispheres. The SMPC frequency of occurrence is calculated by dividing the number of hourly
297 data containing SMPC samples during a month by the number of total hours (i.e., all-sky
298 conditions that include both clear and cloudy skies) during the same month. In the Arctic,
299 observed SMPC exhibits the largest frequency of occurrence in late boreal spring and the lowest
300 SMPC occurrence in boreal summer. A relatively large frequency of occurrence is observed in
301 boreal autumn and winter. Throughout the year, the observed frequency of occurrence of SMPC
302 at the AWR site is substantially lower than at the NSA site, except for summertime. Seasonally,
303 however, SMPCs occur more frequently during the warm season (austral summer and autumn),
304 peaking in early austral autumn at the AWR, while the occurrences become less frequent in
305 austral winter and spring.

306



307

308 Figure 1. Comparison of seasonal frequency of occurrence of total stratiform mixed-phase clouds

309 (SMPC) between EAMv2 simulation and ARM ground-based retrievals at NSA and AWR sites

310 (a). The seasonal variation of the number of collocated SMPCs is shown in (b).

311

312 Compared to the observations, although the model generally simulates the seasonal
 313 variations of the frequency of occurrence of SMPC at both sites, the frequency of occurrence of
 314 EAMv2 simulated SMPC is clearly biased in individual months, with noticeable differences
 315 between the two polar locations. In the Arctic, the model overestimates the frequency of

316 occurrence from boreal mid-summer to mid-spring and underestimates cloud occurrences for the
317 rest of the months. Conversely, the SMPC frequency of occurrence at AWR is largely
318 underestimated across the year except in early austral summer. The observed cold versus warm
319 seasonal contrast is largely captured at AWR. The excessive cloud occurrences in the Arctic and
320 the deficit in cloud occurrences in the Antarctic are consistent with M. Zhang et al. (2022). They
321 also found that EAMv2 overestimates supercooled liquid clouds in the Arctic and substantially
322 underestimates total cloud cover over Antarctica in comparison with the CALIPSO-GOCCP
323 data. It is encouraging that EAMv2 can reasonably simulate the larger frequency of occurrences
324 of total SMPC in the Arctic than in the Antarctic, which is consistent with DZ19. Note that the
325 retrieved frequency of occurrence in Figure 1 represents the largest possible SMPC occurrence
326 because we count the SMPC occurrence in each one-hour window as long as SMPC appears
327 once when degrading the 30-second temporal resolution to one hour. The retrieved frequency of
328 occurrence is largely reduced (by ~28% at NSA and ~50% at AWR annually) if we consider
329 SMPCs to last at least 30 minutes in each one-hour window. However, with a relatively coarse
330 temporal resolution of the hourly data, we keep the largest possible SMPC occurrences to ensure
331 sufficient data in the statistical analysis in the following sections. Regardless of the sensitivity of
332 observed SMPC occurrence to temporal resolutions, the seasonal variation of SMPC frequency
333 of occurrence is not affected at different temporal resolutions (not shown).

334 With the model's capability to capture sufficient occurrences of SMPC at the NSA and
335 AWR sites, modeled SMPCs can be collocated with the observed SMPCs in DZ19. The
336 collocation approach, which was introduced in Section 4, allows the case-by-case evaluations of
337 modeled SMPC properties in two hemispheres at high latitudes. Figure 1b shows the monthly
338 amount of collocated SMPCs in EAMv2. Generally, the number of collocated SMPCs follows

339 the seasonal variation of frequency of occurrence of total SMPCs. For example, more collocated
 340 SMPCs appear in boreal late spring and autumn at the NSA site when more SMPCs are
 341 observed. Collocated SMPCs also occur more frequently in austral summer and autumn at the
 342 AWR site. Similar to the difference in the frequency of occurrence of total SMPCs between NSA
 343 and AWR, the number of collocated SMPCs also shows a noticeable hemispheric difference
 344 throughout the year. In total, the number of collocated SMPCs is 2888 and 700 at NSA and
 345 AWR, respectively, accounting for ~60% and ~45% of total SMPC samples in the model and
 346 ~74% and ~29% of SMPC samples in the observation. Although the percentage of collocated
 347 SMPCs to total SMPC data is relatively low at the AWR site, the comparison of cloud property
 348 statistics between collocated and non-collocated SMPCs indicates that the collocated SMPC data
 349 are generally representative of the annual statistics of total SMPCs observed at two sites (not
 350 shown). In the following analysis, we will focus on the collocated SMPCs to evaluate simulated
 351 cloud properties at two high-latitude ARM locations.

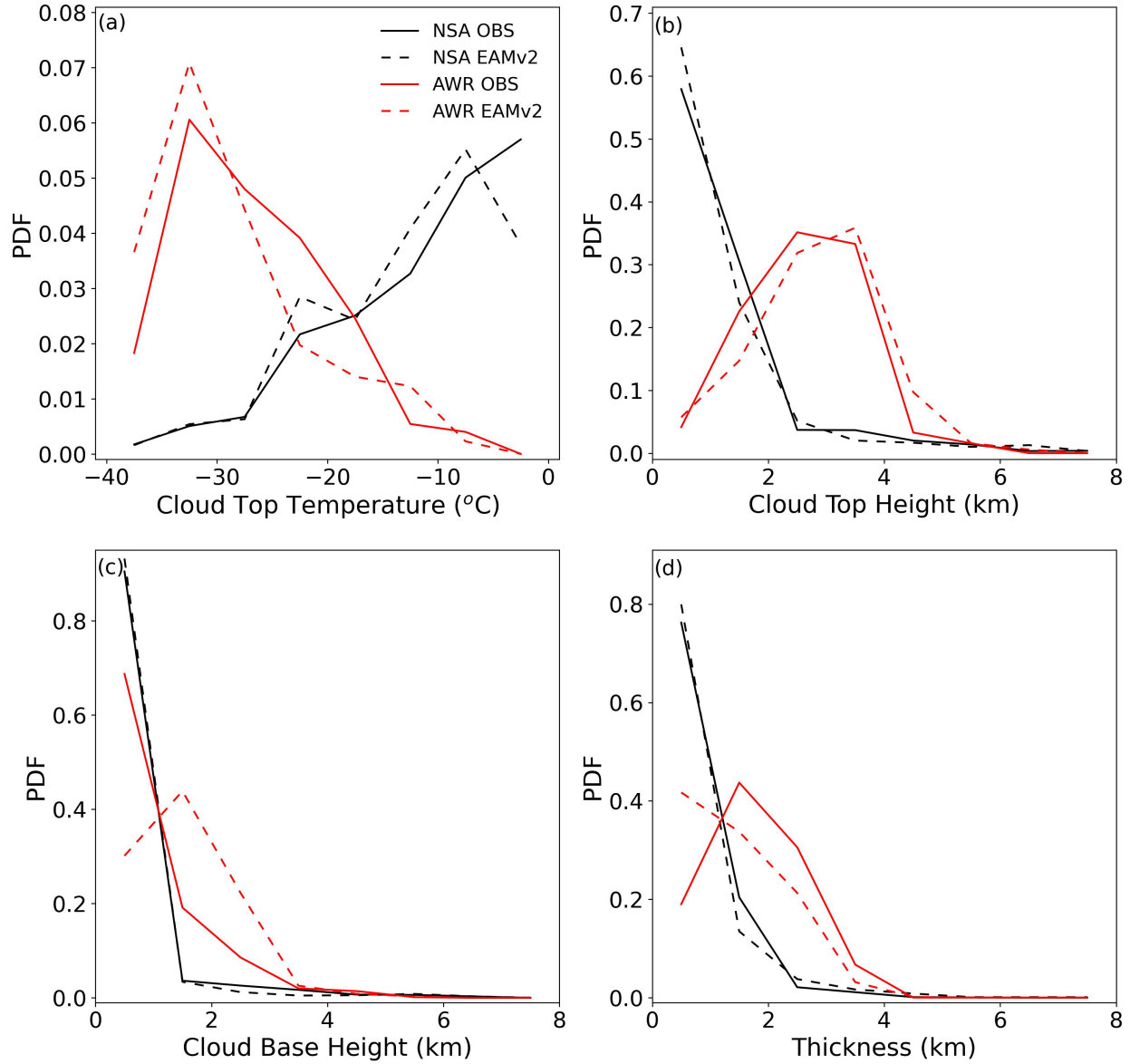
352

353 **5.2. Cloud Macrophysical Properties**

354 Figure 2 compares the probability density function (PDF) of cloud macrophysical
 355 properties of collocated SMPCs between EAMv2 and ARM retrievals. The PDF comparison
 356 provides an overall evaluation of the modeled cloud top temperature (CTT), cloud top height
 357 (CTH), cloud base height (CBH), and cloud thickness (THK) of all collocated SMPCs at the
 358 NSA and AWR sites across the year. In EAMv2, cloud top and cloud base are determined as the
 359 highest and lowest model levels with cloud fractions greater than 5%. THK is the difference
 360 between CTH and CBH, and CTT is the simulated temperature of the model level where the
 361 cloud top is located. As introduced in Section 3, the ARM retrieved cloud top and cloud base are

362 based on the ARSCL algorithm. The retrieved CTT is the temperature of liquid-dominated layer
 363 at cloud top.

364



365

366 Figure 2. PDFs of observed and modeled cloud top temperature (CTT, a), cloud top height
 367 (CTH, b), cloud base height (CBH, c), and cloud thickness (THK, d) for collocated cloud data
 368 between EAMv2 (dashed line) and ARM retrievals (solid line). Black color represents the NSA
 369 site and red color represents the AWR site.

370

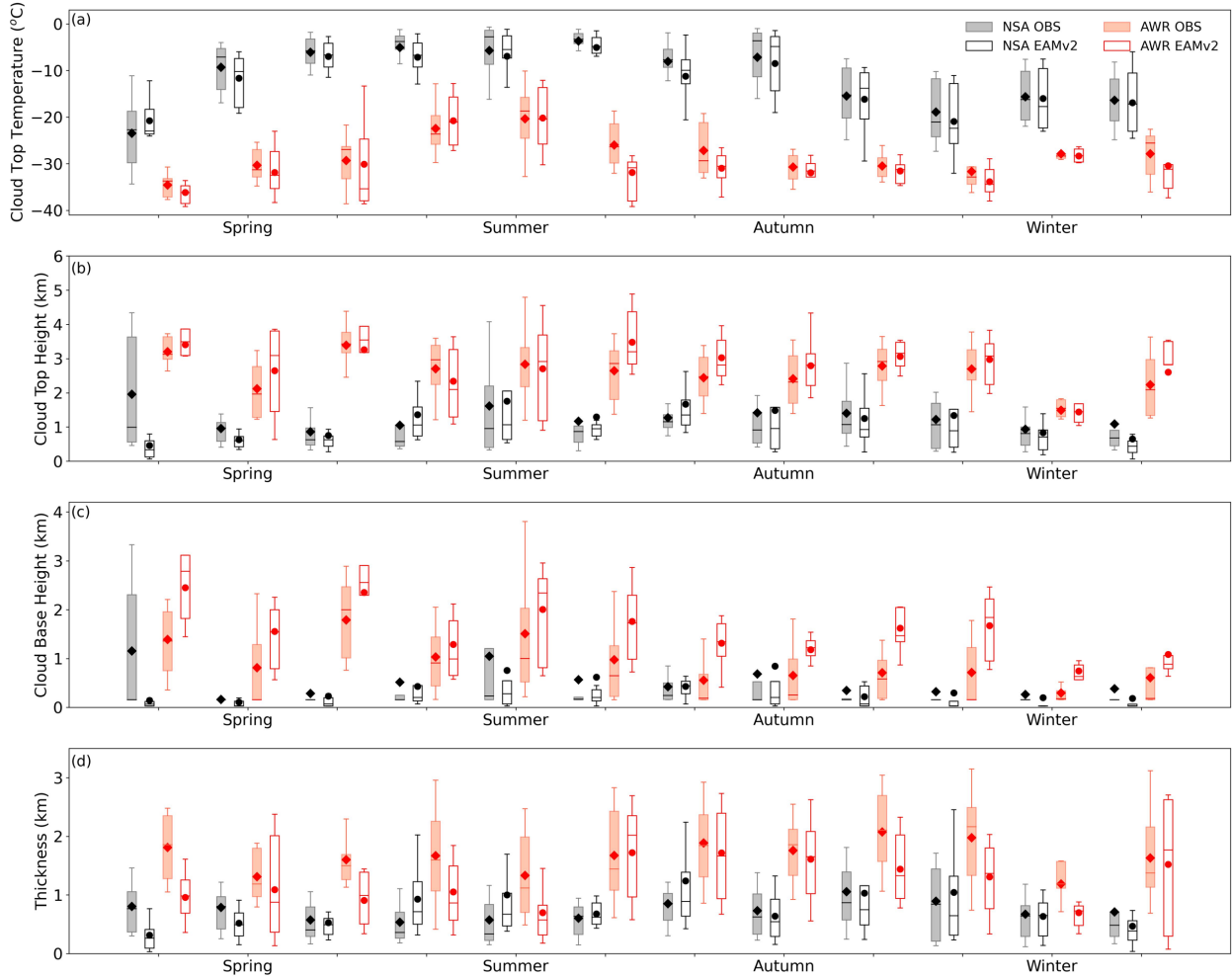
371 In general, EAMv2 simulated SMPCs resemble the features of the annual statistics of
372 cloud properties in the observation, especially for their PDF distributions (Figure 2). For
373 example, the PDF of observed CTT increases monotonically with increasing temperatures at the
374 NSA site, suggesting that most Arctic SMPCs are formed under relatively warm conditions. The
375 monotonic feature at the NSA is reproduced by EAMv2 for CTT colder than -10°C , although the
376 modeled CTT PDF fails to increase further for temperatures warmer than -8°C . On the other
377 hand, observed SMPCs at the AWR site have the largest probability of CTT around -32°C . The
378 peak of observed CTT PDF at the AWR is also captured by EAMv2. Thus, the hemispheric
379 difference in CTT PDF between the NSA and AWR sites is reasonably shown in EAMv2.
380 However, the model underestimates the probabilities for CTT warmer than -8°C and
381 overestimates the probabilities for CTT between -8°C and -25°C at the NSA, and more
382 occurrences of CTT colder than -28°C and fewer occurrences between -15°C and -28°C are
383 simulated at the AWR.

384 For retrieved CTH, CBH, and THK in collocated SMPCs at the NSA site, the PDFs
385 decrease monotonically with increasing cloud boundary heights and thickness, with the
386 maximum probabilities occurring below ~ 1 km for CTH and CBH and thinner than 1 km for
387 THK. It is evident from Figure 2 that EAMv2 reasonably reproduces the PDFs of CTH, CBH,
388 and THK for collocated SMPC cases at the NSA site. The comparable PDFs in cloud boundaries
389 suggest that when large-scale states (i.e., U, V, and T) are constrained by the reanalysis data,
390 EAMv2 has the capability to simulate the annual statistics of these macrophysical cloud
391 properties in the Arctic. Figure 2b shows that the CTH PDF of observed SMPCs at the AWR has
392 a plateau between 2.5 and 4 km. The occurrences of CTH higher than 2 km are substantially

393 greater than those for the Arctic SMPCs. The collocated SMPCs from EAMv2 also exhibit a
 394 similar plateau in their CTH PDF, while the modeled PDF shifts toward higher CTHs. However,
 395 PDF biases are significant for CBH and THK at the AWR site. While the probabilities of
 396 observed CBH decrease monotonically with increasing heights, EAMv2 simulates a peak at
 397 about 1.6 km. Instead of a peak in the observed THK PDF near 1.8 km, the model features a
 398 monotonic decrease in the THK PDF. The model overestimates the occurrences of CBH higher
 399 than 1 km and underestimates the occurrences of THK larger than 1.2 km at the AWR.
 400 Nevertheless, regarding the cloud property difference between the two sites, the statistically
 401 higher cloud base and cloud top and the thicker cloud layer in observed Antarctic SMPCs are
 402 simulated by EAMv2 as compared to the Arctic SMPCs.

403 The monthly statistics of modeled cloud macrophysical properties for collocated SMPCs
 404 are evaluated in Figure 3. Figure 3a shows that the observed CTT of collocated SMPCs at both
 405 polar sites is warmer in summer than in winter. Compared with the retrieved CTT, cold bias as
 406 indicated by the colder mean CTT is simulated from the model at the NSA site from boreal mid-
 407 spring to early winter. A similar cold bias is also simulated at the AWR site except for early to
 408 mid-summer. These cold biases largely contribute to the overestimation of probabilities of
 409 modeled CTT between -8°C and -25°C at the NSA site and CTT colder than -28°C at the AWR
 410 site, as discussed in Figure 2a.

411



412

413 Figure 3. Monthly statistics of stratiform mixed-phase clouds at the NSA (black) and AWR (red)
 414 sites: (a) CTT, (b) CTH, (c) CBH, and (d) THK. The box-and-whisker plots provide 10th, 25th,
 415 50th, 75th, and 90th percentiles of the month statistics. Shaded boxes represent the observations
 416 and clear boxes represent the EAMv2 simulation. Monthly means are shown by diamonds and
 417 circles for the observation and model, respectively.

418

419 The monthly statistics of simulated CTH, CBH, and THK in collocated SMPCs are
 420 shown in Figures 3b-d. At the NSA site, the significant underestimation of CTH in early boreal
 421 spring dominates the biased PDF for CTH lower than 1 km (Figure 2b). Note that the

422 underestimation of CTH in early boreal spring is primarily related to our averaging method. As
423 we averaged 30-second SMPC data to hourly resolution as long as SMPC appears once within
424 that one-hour segment, we found that early spring has a significant amount of data containing
425 target SMPCs for less than 30 minutes during each one-hour time segment at NSA. The biased
426 CTH will be substantially alleviated if a minimum 30-minute criterion is considered in the data
427 processing (not shown). A similar influence is also found for biases in CBH and THK at the
428 NSA site in the same season. Consistent with the PDF analysis, Arctic SMPCs are frequently
429 formed at altitudes close to the surface (CBH below 0.5 km) throughout the year in both model
430 simulation and observation. Compared to the observed THK, the simulated mean THK for
431 collocated SMPCs is thinner from late boreal winter to late spring, but the model overestimates
432 the mean THK in boreal summer and early autumn at the NSA site (Figure 3d). The
433 compensating errors cancel out the biases shown in the annual THK PDF. For simulated cloud
434 boundary properties at the AWR site, EAMv2 overestimates monthly mean CTH from austral
435 late summer to mid-spring. The overestimation leads to statistically more simulated SMPCs with
436 CTH higher than 4 km in austral summer and autumn, shifting the CTH PDF toward higher
437 altitudes (Figure 2b). Moreover, biases in CBH and THK are persistent all year round compared
438 to the observations at the AWR site. The mean cloud base of collocated SMPCs in EAMv2 is
439 substantially higher in all months, and the simulated mean cloud thickness is thinner than the
440 observations except in late austral summer. The high CBH bias and low THK bias primarily
441 result in the overestimated probabilities for cloud bases higher than 2 km and cloud layers
442 thinner than 1 km at the AWR site. By comparing the monthly statistics of cloud macrophysical
443 properties between the two sites, the model well simulates the hemispheric difference in
444 observed cloud macrophysical properties in individual months. These features include colder

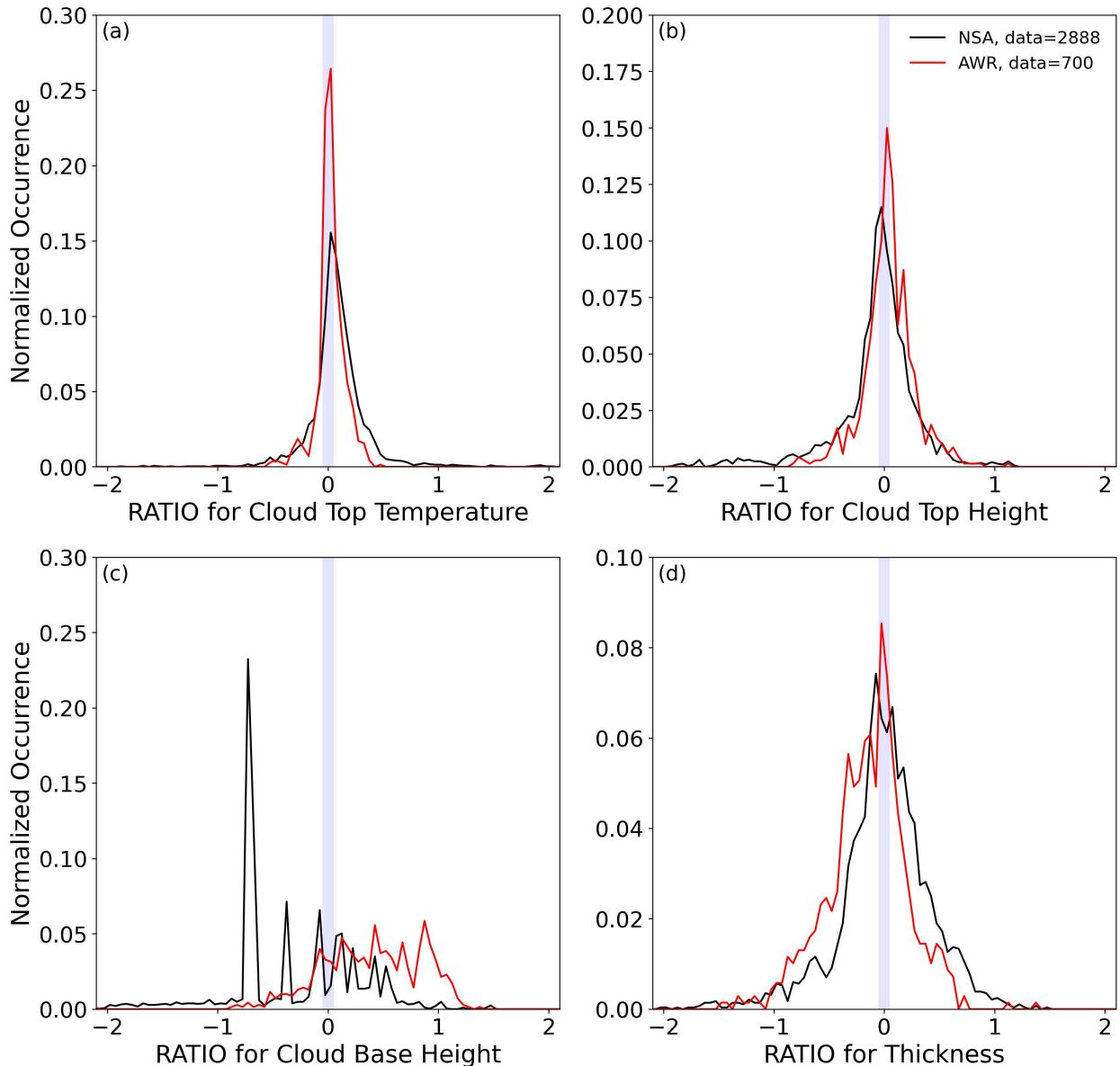
445 CTT, higher CTH, higher CBH, and thicker THK in the Antarctic SMPC compared to the Arctic
 446 clouds.

447 To better quantify model biases in the representation of SMPC properties, we perform
 448 case-by-case comparisons of collocated SMPCs between EAMv2 and DZ19. The case-by-case
 449 evaluation provides details of individual SMPCs that are simultaneously present in the model
 450 and observation under comparable atmospheric conditions with nudged circulation and
 451 temperature in the model. We use “RATIO,” which is the common logarithm of the ratio of an
 452 EAMv2 simulated cloud property over an observed cloud property for each pair of the collocated
 453 data (Equation 1), to describe the errors in simulated SMPC properties. The RATIO value of 0
 454 indicates that the simulated cloud property is the same as the observed value. $RATIO > 0$ (< 0)
 455 suggests that the simulated cloud property is overestimated (underestimated) compared to the
 456 observation. We consider the RATIO range within ± 0.05 as a reasonable model performance,
 457 which represents approximately $\pm 10\%$ differences from the observations.

$$458 \quad RATIO_{Property} = \log_{10} \frac{Property_{EAMv2}}{Property_{ARM}} \quad (1)$$

459 The normalized occurrences of RATIO for CTT, CTH, CBH, and THK are shown in
 460 Figure 4. Normalized occurrence is calculated by dividing the amount of data in each cloud
 461 property bin by the total amount of data. $RATIO_{CTT}$ exhibits a normal distribution pattern at both
 462 NSA and AWR sites with the largest occurrences near 0, indicating that the majority of
 463 simulated CTT is comparable to observed CTT when evaluating SMPCs with the case-by-case
 464 comparison. However, EAMv2 tends to simulate more occurrences of colder CTT than warmer
 465 CTT against the observations, indicated by the long tails on $RATIO_{CTT} > 0$. Normal distribution-
 466 like patterns are also shown for $RATIO_{CTH}$ and $RATIO_{THK}$ at the NSA site. Despite the PDF
 467 peaks around 0, the occurrences of $RATIO_{CTH}$ and $RATIO_{THK}$ beyond ± 0.05 (outside blue boxes)

468 are also relatively large at both sites, suggesting biases in simulated cloud boundaries. Consistent
 469 with earlier discussion, secondary peaks are shown at about 0.2 for $RATIO_{CTH}$ and below 0 for
 470 $RATIO_{THK}$ at AWR, which indicates the too-high CTH and too-thin THK in simulated SMPCs.
 471 Interestingly, even with fewer collocated data, the SMPCs at AWR have larger normalized
 472 occurrences within the ± 0.05 range as compared with the SMPCs at NSA for $RATIO_{CTT}$,
 473 $RATIO_{CTH}$, and $RATIO_{THK}$.
 474



475

476 Figure 4. Normalized occurrence of the RATIO metrics for CTT (a), CTH (b), CBH (c), and
 477 THK (d) at the NSA (black) and AWR (red) sites. RATIO is defined as the common logarithm of
 478 the ratio of EAMv2 modeled cloud properties divided by the observed cloud properties for
 479 collocated stratiform mixed-phase clouds. The blue shaded area shows the region where RATIOS
 480 are between -0.05 and 0.05, which represents approximately $\pm 10\%$ differences from the
 481 observations. Note that the cloud top temperature is in the unit of $^{\circ}\text{C}$.

482

483 $\text{RATIO}_{\text{CBH}}$ differs significantly between the NSA and AWR sites (Figure 4c). There is a
 484 peak occurrence at approximately -0.8 at NSA, and the normalized occurrence shows a
 485 decreasing trend from -0.8 to 0.5. The high occurrence of negative values of $\text{RATIO}_{\text{CBH}}$ is
 486 mostly associated with the early spring cases as shown in Figure 3c, in which the model largely
 487 underestimates cloud bases of SMPC at the NSA. Unlike the NSA site, $\text{RATIO}_{\text{CBH}}$ for SMPCs at
 488 the AWR site is primarily positive. The high occurrence of positive values of $\text{RATIO}_{\text{CBH}}$ is
 489 consistent with the annual and monthly statistical analysis shown in Figures 2 and 3. It is worth
 490 noting that a substantial hemispheric difference is identified in the CBH bias, while biases of
 491 other cloud microphysical properties generally share similar normalized distributions at both
 492 hemispheres.

493

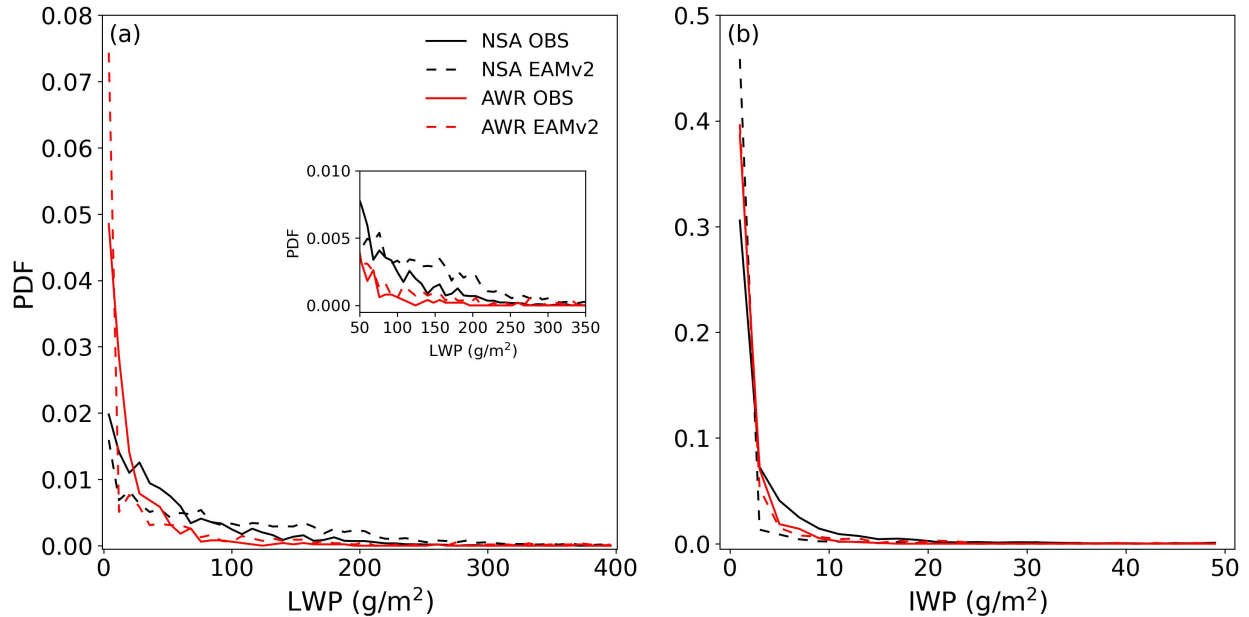
494 **5.3. Cloud Microphysical Properties**

495 In this section, cloud microphysical properties (i.e., LWP and IWP) of collocated SMPCs
 496 in EAMv2 are evaluated against the ARM measurements at the NSA and AWR sites. The PDFs
 497 of LWP and IWP annual statistics are shown in Figure 5. Rain and snow water are included in
 498 the calculation of LWP and IWP in EAMv2 because ground-based remote sensing cannot

499 distinguish them from cloud liquid and ice water. The PDFs of observed LWP and IWP both
500 show the monotonic decreasing features with increasing LWP and IWP. The largest probabilities
501 are at LWP lower than 20 g/m^2 and IWP lower than 5 g/m^2 , respectively. More occurrences of
502 large LWP ($> 20 \text{ g/m}^2$) and IWP ($> 5 \text{ g/m}^2$) are found at the NSA site than at the AWR site in the
503 observation. Compared with DZ19, the probabilities of EAMv2 simulated LWP are larger when
504 LWP is greater than 100 g/m^2 at both NSA and AWR sites. At the same time, lower probabilities
505 of LWP smaller than 50 g/m^2 are simulated at NSA, while simulated Antarctic SMPCs have
506 significantly larger probabilities of LWP close to 0 g/m^2 than the observation. The overestimated
507 occurrences of large LWP in EAMv2 are consistent with M. Zhang et al. (2022) in both
508 hemispheres, in which the CALIPSO simulator-derived cloud liquid covers are substantially
509 overestimated against the CALIPSO-GOCCP data over high-latitude regions. However,
510 inconsistent results are shown in the ice phase evaluation. Although M. Zhang et al. (2022)
511 illustrated that the low bias in cloud ice cover is much improved in Arctic clouds in EAMv2
512 compared to EAMv1, the probabilities of IWP larger than 5 g/m^2 are still underestimated in
513 EAMv2 for the collocated SMPCs at the NSA site (Figure 5b). Meanwhile, even though the
514 simulated IWP PDF is generally comparable to DZ19 at the AWR site, a substantial low bias
515 was shown in ice cloud cover in M. Zhang et al. (2022) in the Antarctic. The different outcome
516 in the ice phase evaluation against DZ19 and CALIPSO-GOCCP is probably a mixed result from
517 differences in the observations (ground-based versus space-borne remote sensing measurements),
518 model simulations (nudged runs vs. climate free runs), and data sampling (collocated cases vs.
519 climatology). For instance, for the Arctic SMPCs, the precipitating ice below supercooled liquid
520 layer is often missed by the CALIPSO lidar due to the strong attenuation of lidar beam by the
521 optically thick liquid water at cloud top. On the other hand, the ground-based radar and lidar

522 combined measurements can more accurately detect these precipitating hydrometeors, leading to
 523 larger amounts of cloud ice water in DZ19.

524



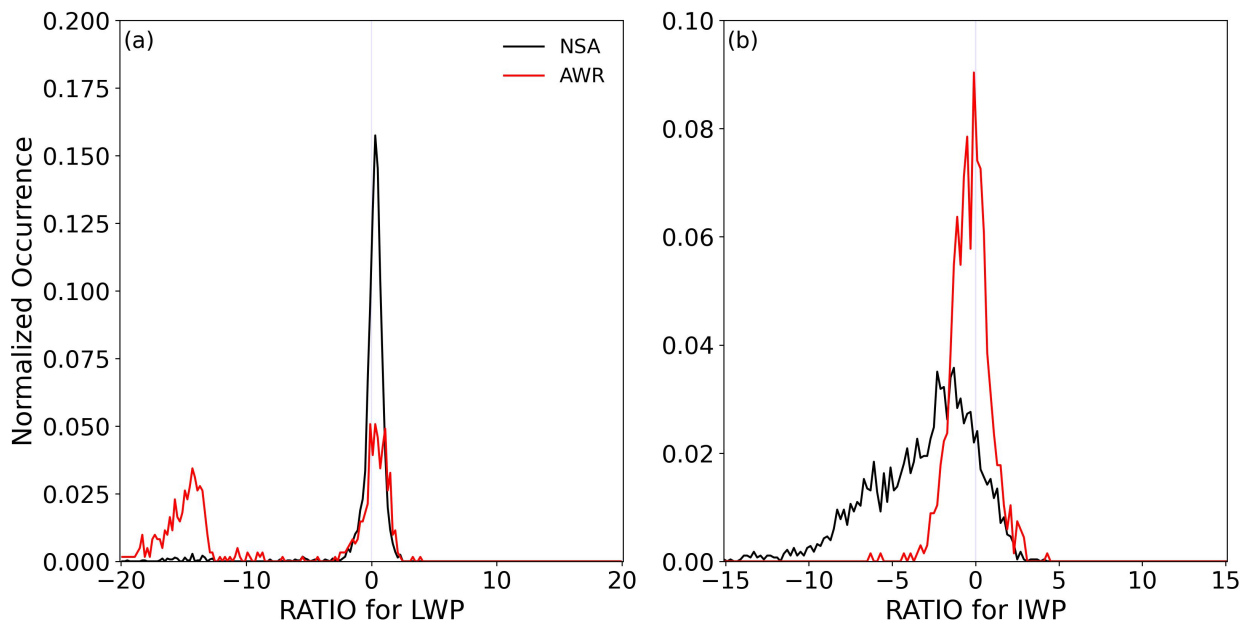
525

526 Figure 5. PDFs of observed and modeled liquid water path (LWP, a) and ice water path (IWP, b)
 527 for collocated stratiform mixed-phase clouds between EAMv2 (dashed line) and ARM retrievals
 528 (solid line). Black color represents the NSA site and red color represents the AWR site. The inlet
 529 figure in (a) is the PDF for LWP ranging from 50 to 350 g/m^2 .

530

531 By evaluating $\text{RATIO}_{\text{LWP}}$ and $\text{RATIO}_{\text{IWP}}$ through case-by-case comparisons of collocated
 532 SMPCs, biases in simulated LWP and IWP are identified under comparable large-scale
 533 conditions. Figure 6 shows that EAMv2 frequently overestimates LWP in collocated SMPCs at
 534 both sites, consistent with the PDF analysis in Figure 5. The distribution of $\text{RATIO}_{\text{LWP}}$ peaks
 535 close to 0.5 at the NSA site. The overestimation of LWP is found in all seasons at the NSA, and
 536 the overestimation is the most substantial in austral summer when analyzing their monthly

537 statistics (not shown). At the AWR site, the highest peak of $RATIO_{LWP}$ is found around 0, but
 538 $RATIO_{LWP}$ also peaks at about -15. We note that the large occurrences of $RATIO_{LWP}$ smaller
 539 than -10 at AWR are associated with simulated clouds dominated by ice water. The dominance
 540 of ice water in simulated SMPC in the Antarctic is probably because of the cold temperature that
 541 effectively favors ice phase microphysical processes. This feature is further suggested by the
 542 large amounts of data located at $RATIO_{IWP}$ between ± 0.5 at the AWR site. On the other hand,
 543 most data are associated with negative $RATIO_{IWP}$ at NSA, with a negative peak close to -2. This
 544 negative peak again indicates insufficient ice water formation in SMPCs at the NSA site. The
 545 underestimation of IWP is found throughout the year at the NSA site (not shown). Negative
 546 biases in IWP compared to the ARM long-term measurements are consistent with M. Zhang et
 547 al. (2020), where EAMv1 was evaluated against the observational data from the ARM M-PACE
 548 field campaign in October 2004. Similar negative ice phase biases in EAMv2 imply that ice-
 549 related microphysics needs further improvements in the future E3SM model development.
 550



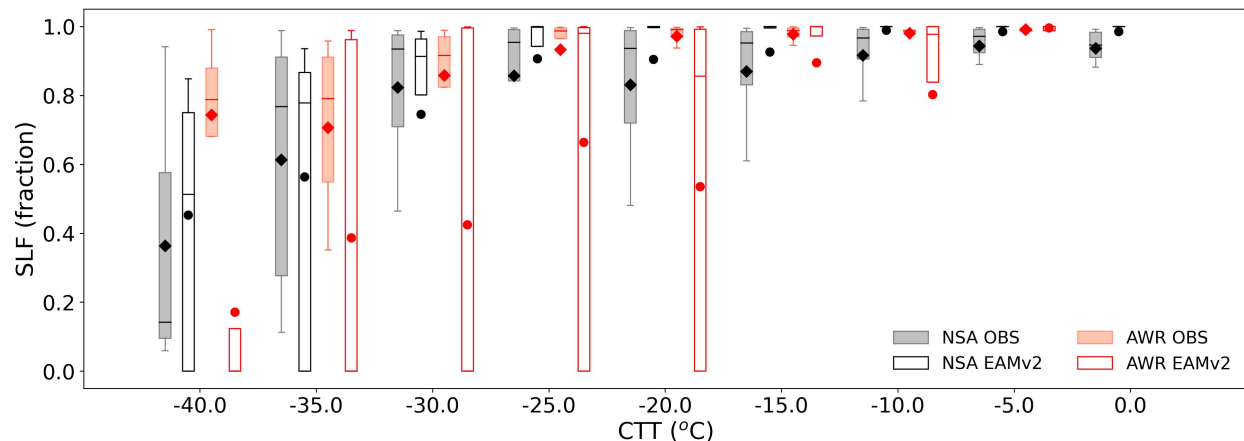
551

552 Figure 6. Normalized occurrence of the RATIO metrics for LWP (a) and IWP (b) at the NSA
553 (black) and AWR (red) sites. The blue shaded area shows the region where RATIOS are between
554 -0.05 and 0.05, which represents approximately $\pm 10\%$ differences from the observations.

555

556 Several studies showed that measured SLF in mixed-phase clouds in the Northern
557 Hemisphere is substantially smaller than in the Southern Hemisphere at a given temperature (Tan
558 et al., 2014; D. Zhang et al., 2019). By examining the SLF statistics of collocated SMPCs in
559 different CTT bins, lower SLF is also observed in collocated SMPCs at the NSA site compared
560 with clouds at the AWR site (Figure 7). However, such a hemispheric difference in SLF is poorly
561 simulated for collocated SMPCs at the two ARM locations in EAMv2. At individual CTT bins
562 from -40°C to -10°C , simulated SLF at the NSA site is consistently larger than at the AWR site.
563 The biased LWP and IWP at both sites together contribute to the biased hemispheric difference
564 of SLF. For example, EAMv2 frequently underestimates IWP while LWP is reasonable at NSA,
565 making simulated SLF too large in most CTT bins compared with DZ19. Meanwhile, simulated
566 LWP in collocated SMPCs is frequently underestimated at the AWR site, but the IWP in these
567 SMPCs is overall comparable to the observation. The biased cloud water in liquid and ice phases
568 at the AWR site results in a much lower SLF than the observation and even lower than that at the
569 NSA, especially at CTT colder than -10°C .

570



571
 572 Figure 7. The box-and-whisker plots of supercooled liquid fraction (SLF) as a function of cloud
 573 top temperature in collocated stratiform mixed-phase clouds at the NSA (black) and AWR (red)
 574 sites. The box-and-whisker plots provide the 10th, 25th, 50th, 75th, and 90th percentiles of the SLF
 575 in each temperature bin. Shaded boxes represent the observations and clear boxes represent the
 576 EAMv2 simulation. The mean SLF for each temperature bin is shown by the diamond and circle
 577 for the observation and model, respectively.

578

579

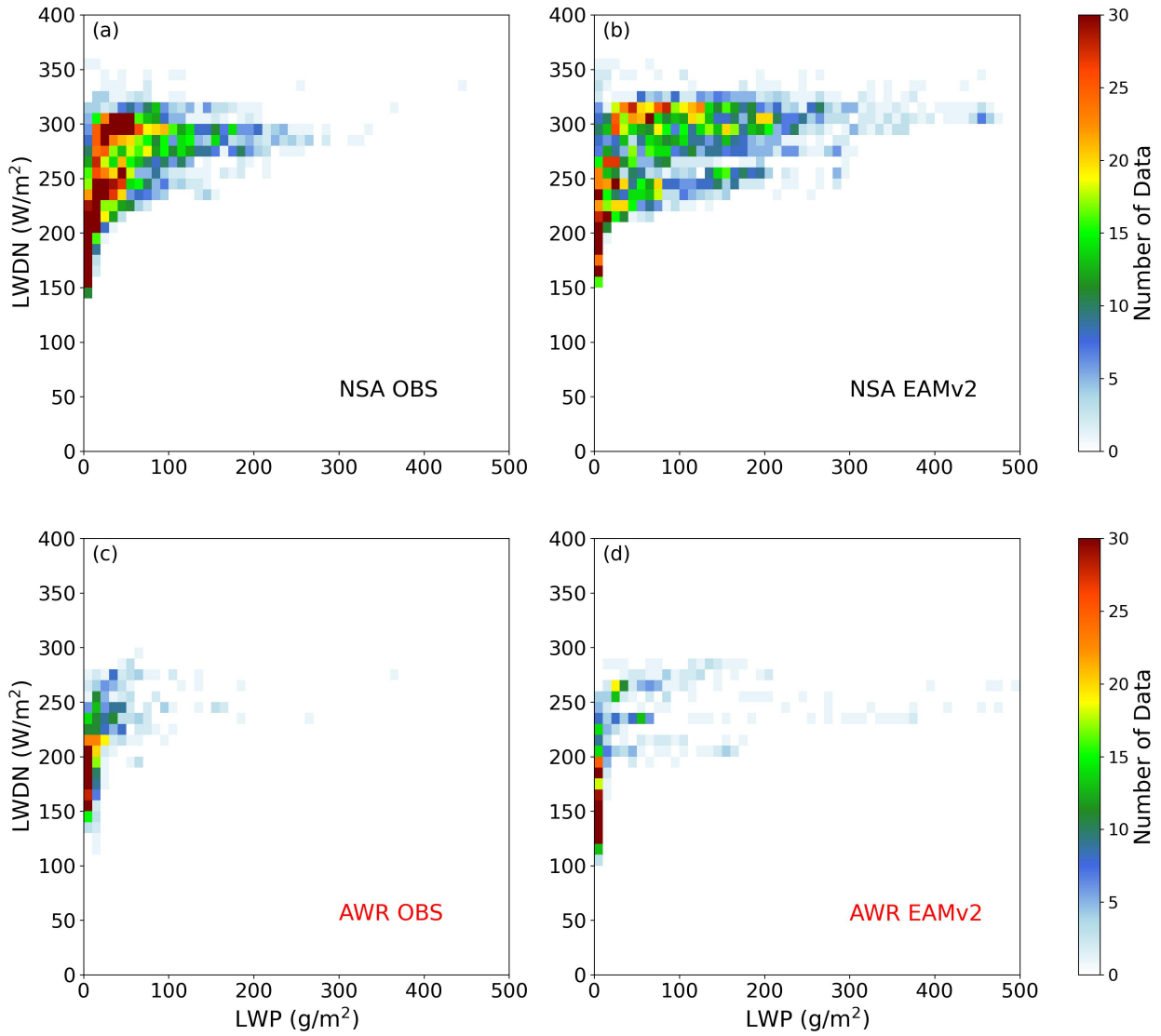
580 **5.4. Cloud Radiative Properties**

581 It is well-known that LWP plays a more critical role in cloud radiative effects than IWP
 582 in mixed-phase clouds (Bennartz et al., 2013; Nicolas et al., 2017). To understand how the model
 583 simulated LWP influences the surface radiation at the NSA and AWR sites, we compare the
 584 surface downwelling longwave (LWDN) radiative fluxes between EAMv2 and ARMBE data for
 585 all collocated SMPCs. The reason for examining LWDN at the surface is because it can directly
 586 reflect the impact of cloud properties on cloud radiative effects. To exclude the effect of multiple
 587 scattering between the bright underneath surface and the low-level SMPCs in high latitude
 588 regions (Xie et al., 2006), surface downwelling shortwave radiation is thus not shown. The two-

589 dimensional histograms between LWP and LWDN are shown in Figure 8. In terms of the
 590 relations between LWP and LWDN, the majority of observed SMPCs have LWP below 130
 591 g/m^2 (90th percentile) at the NSA site. The associated LWDN is observed to range between 150
 592 and 350 W/m^2 for the collocated SMPC samples. At the AWR site, most observed LWP is less
 593 than 50 g/m^2 (90th percentile), and the emitted LWDN is mostly below 280 W/m^2 , both of which
 594 are much lower than those at the NSA site. The colder temperature and lower LWP in observed
 595 SMPCs at AWR can largely explain this hemispheric difference in LWDN. Compared to the
 596 observations, regardless of the large amounts of data with small LWP values ($\text{RATIO}_{\text{LWP}} < -10$)
 597 at the AWR site, the model overestimation of LWP is shown at both sites. The occurrences of
 598 modeled LWP greater than 130 g/m^2 at the NSA and the occurrences of LWP greater than 50
 599 g/m^2 at the AWR are approximately 3.1 times and 2.4 times higher than the observations,
 600 respectively. As expected, this larger LWP in simulated SMPCs leads to stronger LWDN at the
 601 surface. At the NSA in EAMv2, nearly 34% of the collocated SMPCs with LWP greater than
 602 130 g/m^2 have LWDN stronger than 305 W/m^2 (90th percentile of observed LWDN). The
 603 occurrences of these SMPCs with large LWP and LWDN are substantially (6.5 times) more than
 604 the observation. At the AWR site, almost all the collocated SMPCs with LWP larger than 50
 605 g/m^2 have LWDN larger than 200 W/m^2 in EAMv2, contributing to about 63% of the
 606 occurrences of large LWDN ($> 260 \text{ W/m}^2$, 90th percentile of observed LWDN at AWR) in the
 607 model. The occurrence of simulated strong LWDN is thus larger than the observed radiative flux
 608 by a factor of 3.2. Nicolas et al. (2016) suggested that mixed-phase clouds with LWP greater
 609 than 40 g/m^2 can be optically thick enough to attenuate shortwave radiation and emit longwave
 610 radiation as the blackbody. These clouds can remarkably influence the surface energy budget and
 611 lead to extensive melting events over West Antarctica. Therefore, EAMv2 simulated too strong

612 LWDN fluxes at the surface will potentially also result in a biased prediction of the surface
613 energy budget and then impact the model simulation of surface melting events and regional and
614 global climate prediction.

615



616

617 Figure 8. 2-D Histograms of longwave downward radiative flux (LWDN) at the surface and
618 LWP at the NSA (a-b) and AWR (c-d) sites from EAMv2 and ARM observations.

619

620

621 **6. Summary and discussion**

622 This study evaluates the cloud properties of high-latitude SMPCs simulated by EAMv2
623 against the U.S. DOE ARM ground-based remote sensing retrievals at the NSA and AWR sites
624 in 2016. To improve the model-observation comparison, the horizontal wind (U, V) and
625 temperature (T) fields are nudged toward ERA-Interim reanalysis data for 2016 with a nudging
626 relaxation time scale of 6 hours. Simulated clouds are selected with similar characteristics to
627 observed clouds by using the consistent definitions used in the ARM retrievals. In general, the
628 model reproduces the seasonal variation of the frequency of occurrence of observed SMPCs at
629 both sites. The larger SMPC frequency of occurrence at the NSA site than at the AWR site is
630 also well simulated. However, EAMv2 tends to overestimate cloud frequency of occurrence from
631 boreal mid-summer to spring at the NSA while underestimating the frequency of occurrence
632 throughout the year at the AWR, which is consistent with the CALIPSO-GOCCP evaluation by
633 M. Zhang et al. (2022).

634 Under constrained large-scale environments in the nudging simulations, a collocation
635 method is applied to the SMPCs from the model and observations to merit case-by-case
636 comparisons. Collocated evaluation indicates that EAMv2 simulated SMPCs well capture the
637 observed annual statistics in the PDFs of cloud macrophysical properties at the NSA site.
638 Through monthly and case-by-case evaluations, the largest model biases are found in early
639 boreal spring, when the model largely underestimates CTH, CBH, and THK at the NSA. At the
640 AWR site, larger biases are shown in simulated SMPC properties. In particular, simulated CTH
641 and CBH are much higher than observations across the year. The larger magnitude of
642 overestimation in CBH leads to the underestimated THK in the Antarctic clouds. Regardless of
643 the biases in the statistical comparison of cloud macrophysical properties, our collocated SMPCs

644 in EAMv2 well resemble the observed hemispheric differences such as the higher CTH and
645 CBH, larger THK, and colder CTT at the AWR site than those clouds at the NSA site.

646 Model biases in cloud microphysical properties are more noticeable than cloud
647 geometrical properties. At the NSA site, there are substantially more simulated SMPCs with
648 LWP greater than 100 g/m^2 compared with the observation. The frequent overestimated LWP
649 results in positive biases in the simulation of longwave downward radiative fluxes at the surface.
650 By analyzing case-by-case comparisons, we found that EAMv2 tends to simulate SMPCs with
651 significantly underestimated LWP at the AWR site. These extreme SMPC cases are ice water
652 dominated and are primarily associated with the cold environment in the Antarctic region that
653 effectively favors ice microphysical processes. For simulated IWP, although M. Zhang et al.
654 (2022) shows a much-improved ice phase cloud cover in EAMv2 compared to EAMv1, the
655 evaluation in this study still indicates that EAMv2 underestimates cloud ice water as compared
656 with ground-based remote sensing retrievals at the NSA site. Such a discrepancy suggests that
657 different instrument limitations must be considered in the model evaluation. The different
658 capability of instruments to detect precipitating ice below supercooled liquid layers, which is a
659 common feature in high-latitude mixed-phase clouds, probably explains the cloud ice difference
660 in space- and ground-based remote sensing retrievals. In addition, the different types of model
661 simulations (nudged runs vs. climate free runs) and different data sampling methods (collocated
662 cases vs. climatology) also attribute to the discrepancy. The biased cloud water path simulation
663 makes the observed hemispheric difference in SLF poorly simulated in EAMv2, which becomes
664 opposite to the observation.

665 In recent model development studies, secondary ice production (SIP) has received more
666 attention due to its essential role in bridging the gap of orders of magnitude differences between

667 cloud ice number concentration and ice nucleating particle concentrations in high-latitude mixed-
668 phase clouds (Zhao & Liu, 2021, 2022; Zhao et al., 2021). In the current MG2 cloud
669 microphysics, SIP is only represented by the Hallett-Mossop process within the narrow
670 temperature range from -3 to -8°C. Other SIP mechanisms, such as frozen raindrop shattering and
671 ice-ice collisional breakup, are still missing in E3SMv2. By including these mechanisms, Zhao et
672 al. (2021) demonstrated that SIP is the dominant source of ice crystals for Arctic mixed-phase
673 clouds, especially when clouds are formed in a relatively warm temperature range. Meanwhile,
674 enhancing ice phase cloud microphysical processes could alleviate the issue of overestimated
675 liquid cloud water in Arctic mixed-phase clouds. This could also eventually improve the model
676 representation of anthropogenic aerosol forcing, as overestimated LWP was found to lead to
677 larger anthropogenic aerosol effects through aerosol-cloud interactions in the Arctic region (K.
678 Zhang et al., 2022).

679 In conclusion, this study illustrates that the EAMv2 model has the capability to
680 reasonably simulate the annual statistics of SMPC cloud macrophysical property differences
681 between two polar locations. The reproduction of hemispheric differences in cloud structure in
682 the state-of-the-art GCM will be helpful to better understand the formation mechanisms in high-
683 latitude mixed-phase clouds in both hemispheres. However, further efforts are needed in the
684 development of cloud microphysical parameterizations to achieve a reasonable representation of
685 cloud phase over two high-latitude regions.

686

687

688

689 **Acknowledgment:** This research was supported as part of the Energy Exascale Earth System
690 Model (E3SM) project, funded by the U.S. Department of Energy, Office of Science, Office of
691 Biological and Environmental Research. Work at LLNL was performed under the auspices of the
692 U.S. DOE by Lawrence Livermore National Laboratory under contract No. DE-AC52-
693 07NA27344. Xiaohong Liu acknowledges the funding support by the DOE Atmospheric System
694 Research (ASR) Program (grant DE-SC0020510) and the DOE Regional and Global Model
695 Analysis (RGMA) Program (grant DE-SC0022065). The Pacific Northwest National Laboratory
696 (PNNL) is operated for the DOE by the Battelle Memorial Institute under contract DE-AC06-
697 76RLO 1830. This research used resources of the National Energy Research Scientific
698 Computing Center (NERSC), a U.S. Department of Energy Office of Science User Facility
699 located at Lawrence Berkeley National Laboratory, operated under Contract No. DE-AC02-
700 05CH11231.

701
702 **Data Availability Statement:** The U.S. DOE E3SMv2 (E3SM Project, DOE, 2021, September
703 29) model was used in the creation of this manuscript. The model data used in this study can be
704 accessible at [https://portal.nersc.gov/archive/home/m/mengz/www/Zhang-E3SMv2-](https://portal.nersc.gov/archive/home/m/mengz/www/Zhang-E3SMv2-MixedPhaseClouds-ARM)
705 [MixedPhaseClouds-ARM](https://portal.nersc.gov/archive/home/m/mengz/www/Zhang-E3SMv2-MixedPhaseClouds-ARM). The ARM observational data are available online at
706 <https://www.arm.gov/data>.

707 **References**

708 Bennartz, R., Shupe, M. D., Turner, D. D., Walden, V. P., Steffen, K., Cox, C. J., et al. (2013).

709 July 2012 Greenland melt extent enhanced by low-level liquid clouds. *Nature*, 496, 83–86.

710 <https://doi.org/10.1038/nature12002>

711

712 Bradley, A. M., Bosler, P. A., & Guba, O. (2021). Islet: Interpolation semi-Lagrangian element-

713 based transport, *Geoscientific Model Development Discussion*. <https://doi.org/10.5194/gmd->

714 2021-296

715

716 Clothiaux, E. E., Ackerman, T. P., Mace, G. G., Moran, K. P., Marchand, R. T., Miller, M. A., &

717 Martner, B. E. (2000). Objective Determination of Cloud Heights and Radar Reflectivities Using

718 a Combination of Active Remote Sensors at the ARM CART Sites, *Journal of Applied*

719 *Meteorology*, 39(5), 645–665. <https://doi.org/10.1175/1520->

720 [0450\(2000\)039<0645:ODOCHA>2.0.CO;2](https://doi.org/10.1175/1520-0450(2000)039<0645:ODOCHA>2.0.CO;2)

721

722 Curry, J. A., Schramm, J. L., Rossow, W. B., & Randall, D. (1996). Overview of Arctic Cloud

723 and Radiation Characteristics. *Journal of Climate*, 9(8), 1731–1764.

724 [https://doi.org/10.1175/1520-0442\(1996\)009<1731:OOACAR>2.0.CO;2](https://doi.org/10.1175/1520-0442(1996)009<1731:OOACAR>2.0.CO;2)

725

726 Gettelman, A., Hannay, C., Bacmeister, J. T., Neale, R. B., Pendergrass, A. G., Danabasoglu, G.,

727 et al. (2019). High climate sensitivity in the Community Earth System Model Version 2

728 (CESM2). *Geophysical Research Letters*, 46, 8329–8337.

729 <https://doi.org/10.1029/2019GL083978>

730

731 Gettelman, A., & Morrison, H. (2014). Advanced two-moment bulk microphysics for global
732 models. Part I: Off-line tests and comparison with other schemes. *Journal of Climate*, 28(3),
733 1268–1287. <https://doi.org/10.1175/JCLI-D-14-00102.1>

734

735 Golaz, J.-C., Larson, V. E., & Cotton, W. R. (2002). A PDF-based model for boundary layer
736 clouds. Part I: Method and model description. *Journal of the Atmospheric Sciences*, 59(24),
737 3540–3551. [https://doi.org/10.1175/1520-0469\(2002\)059<3540:APBMFB>2.0.CO;2](https://doi.org/10.1175/1520-0469(2002)059<3540:APBMFB>2.0.CO;2)

738

739 Golaz, J.-C., Van Roekel, P. L., Zheng, X., Roberts, A., Wolfe, D. J., Lin, W., et al. (2022). The
740 DOE E3SM Model Version 2: Overview of the physical model. *Earth and Space Science Open*
741 *Archive*. <https://doi.org/10.1002/essoar.10511174.1>

742

743 Gregory, D., & Morris, D. (1996). The sensitivity of climate simulations to the specification of
744 mixed phase clouds. *Climate Dynamics*, 12, 641–651. <https://doi.org/10.1007/BF00216271>

745

746 Hannah, W. M., Bradley, A. M., Guba, O., Tang, Q., Golaz, J.-C., & Wolfe, J. (2021).
747 Separating physics and dynamics grids for improved computational efficiency in spectral
748 element earth system models. *Journal of Advances in Modeling Earth Systems*, 13,
749 e2020MS002419. <https://doi.org/10.1029/2020MS002419>

750

751 Harrop, B. E., Ma, P.-L., Rasch, P. J., Neale, R. B., & Hannay, C. (2018). The role of convective
752 gustiness in reducing seasonal precipitation biases in the tropical west pacific. *Journal of*
753 *Advances in Modeling Earth Systems*, 10 (4), 961–970. <https://doi.org/10.1002/2017MS001157>
754

755 Hogan, R. J., Mittermaier, M. P., & Illingworth, A. J. (2006). The retrieval of ice water content
756 from radar reflectivity factor and temperature and its use in evaluating a mesoscale model.
757 *Journal of Applied Meteorology and Climatology*. 45(2), 301–317. [https://doi.org/10.1175/](https://doi.org/10.1175/JAM2340.1)
758 JAM2340.1
759

760 Hoose, C., Kristjánsson, J. E., Chen, J. P., & Hazra, A. (2010). A classical-theory-based
761 parameterization of heterogeneous ice nucleation by mineral dust, soot, and biological particles
762 in a global climate model. *Journal of the Atmospheric Sciences*, 67(8), 2483–2503. [https://doi.](https://doi.org/10.1175/2010JAS3425.1)
763 [org/10.1175/2010JAS3425.1](https://doi.org/10.1175/2010JAS3425.1)
764

765 Klein, S. A., McCoy, R. B., Morrison, H., Ackerman, A. S., Avramov, A., Boer, G. d., et al.
766 (2009). Intercomparison of model simulations of mixed-phase clouds observed during the ARM
767 Mixed-Phase Arctic Cloud Experiment. I: single-layer cloud. *Quarterly Journal of the Royal*
768 *Meteorological Society*, 135, 979–1002. <https://doi.org/10.1002/qj.416>
769

770 Korolev, A., McFarquhar, G., Field, P. R., Franklin, C., Lawson, P., Wang, Z., et al. (2017).
771 Mixed-Phase Clouds: Progress and Challenges. *Meteorological Monographs*. 58, 5.1-5.50.
772 <https://doi.org/10.1175/AMSMONOGRAPHS-D-17-0001.1>
773

- 774 Larson, V. E. (2017). CLUBB-SILHS: A parameterization of subgrid variability in the
775 atmosphere. arXiv preprint arXiv:1711.03675v2
776
- 777 Liu, X., Easter, R. C., Ghan, S. J., Zaveri, R., Rasch, P., Shi, X., et al. (2012). Toward a minimal
778 representation of aerosols in climate models: description and evaluation in the Community
779 Atmosphere Model CAM5, *Geoscientific Model Development*, 5, 709–739.
780 <https://doi.org/10.5194/gmd-5-709-2012>
781
- 782 Liu, X., Ma, P.-L., Wang, H., Tilmes, S., Singh, B., Easter, R. C., et al. (2016). Description and
783 evaluation of a new four-mode version of the Modal Aerosol Module (MAM4) within version
784 5.3 of the Community Atmosphere Model. *Geoscientific Model Development*, 9(2), 505–522.
785 <https://doi.org/10.5194/gmd-9-505-2016>
786
- 787 Liu, Y., Shupe, M. D., Wang, Z., & Mace, G. (2017). Cloud vertical distribution from combined
788 surface and space radar–lidar observations at two Arctic atmospheric observatories. *Atmospheric*
789 *Chemistry and Physics*, 17, 5973–5989, <https://doi.org/10.5194/acp-17-5973-2017>
790
- 791 Lohmann, U. & Neubauer, D. (2018). The importance of mixed-phase and ice clouds for climate
792 sensitivity in the global aerosol–climate model ECHAM6-HAM2. *Atmospheric Chemistry and*
793 *Physics*, 18, 8807–8828. <https://doi.org/10.5194/acp-18-8807-2018>
794
- 795 Lubin, D., Zhang, D., Silber, I., Scott, R. C., Kalogeras, P., Battaglia, A., et al. (2020). AWARE:
796 The Atmospheric Radiation Measurement (ARM) West Antarctic Radiation Experiment, *Bulletin*

797 *of the American Meteorological Society*, 101(7), E1069-E1091. <https://doi.org/10.1175/BAMS->
798 D-18-0278.1

799

800 Ma, P.-L., Harrop, B. E., Larson, V. E., Neale, R., Gettelman, A., Morrison, H., et al. (2022).

801 Better calibration of cloud parameterizations and subgrid effects increases the fidelity of E3SM
802 Atmosphere Model version 1, *Geoscientific Model Development*. 15(7), 2881–2916.

803 <https://doi.org/10.5194/gmd-15-2881-2022>

804

805 McCoy, D. T., Hartmann, D. L., Zelinka, M. D., Ceppi, P., & Grosvenor, D. P. (2015). Mixed-
806 phase cloud physics and Southern Ocean cloud feedback in climate models. *Journal of*

807 *Geophysical Research: Atmospheres*, 120, 9539–9554, <https://doi.org/10.1002/2015JD023603>

808

809 McCoy, D. T., Tan, I., Hartmann, D. L., Zelinka, M. D., & Storelvmo, T. (2016). On the
810 relationships among cloud cover, mixed-phase partitioning, and planetary albedo in GCMs.

811 *Journal of Advances in Modeling Earth Systems*, 8, 650–668.

812 <https://doi.org/10.1002/2015MS000589>

813

814 McErlich, C., McDonald, A., Schuddeboom, A., & Silber, I. (2021). Comparing satellite- and
815 ground-based observations of cloud occurrence over high southern latitude. *Journal of*

816 *Geophysical Research: Atmospheres*, 126, e2020JD033607.

817 <https://doi.org/10.1029/2020JD033607>

818

- 819 McFarquhar, G. M., Bretherton, C. S., Marchand, R., Protat, A., DeMott, P. J., Alexander, S. P.,
820 et al. (2021). Observations of Clouds, Aerosols, Precipitation, and Surface Radiation over the
821 Southern Ocean: An Overview of CAPRICORN, MARCUS, MICRE, and SOCRATES. *Bulletin*
822 *of the American Meteorological Society*, 102(4), E894–E928. [https://doi.org/10.1175/BAMS-D-](https://doi.org/10.1175/BAMS-D-20-0132.1)
823 20-0132.1
- 824
- 825 Middlemas, E. A., Kay, J. E., Medeiros, B. M., & Maroon, E. A. (2020). Quantifying the
826 influence of cloud radiative feedbacks on Arctic surface warming using cloud locking in an Earth
827 system model. *Geophysical Research Letters*, 47, e2020GL089207.
828 <https://doi.org/10.1029/2020GL089207>
- 829
- 830 Morrison, H., de Boer, G., Feingold, G., Harrington, J., Shupe, M. D. & Sulia, K. (2012).
831 Resilience of persistent Arctic mixed-phase clouds. *Nature Geoscience*, 5, 11–17.
832 <https://doi.org/10.1038/ngeo1332>
- 833
- 834 Morrison, H., van Lier-Walqui, M., Fridlind, A. M., Grabowski, W. W., Harrington, J. Y.,
835 Hoose, C., et al. (2020). Confronting the challenge of modeling cloud and precipitation
836 microphysics. *Journal of Advances in Modeling Earth Systems*, 12, e2019MS001689.
837 <https://doi.org/10.1029/2019MS001689>
- 838
- 839 Nicolas, J. P., Vogelmann, A. M., Scott, R. C., Wilson, A. B., Cadeddu, M. P., Bromwich, D. H.,
840 et al. (2017). January 2016 extensive summer melt in West Antarctica favoured by strong El
841 Niño. *Nature Communications*, 8(1), 15,799. <https://doi.org/10.1038/ncomms15799>

842

843 Ovchinnikov, M., Ackerman, A. S., Avramov, A., Cheng, A., Fan, J., Fridlind, A. M., et al.
844 (2014). Intercomparison of large-eddy simulations of Arctic mixed-phase clouds: Importance of
845 ice size distribution assumptions. *Journal of Advances in Modeling Earth Systems*, 6, 223–248.
846 <https://doi.org/10.1002/2013MS000282>

847

848 Rasch, P. J., Xie, S., Ma, P.-L., Lin, W., Wang, H., Tang, Q., et al. (2019). An overview of the
849 atmospheric component of the Energy Exascale Earth System Model. *Journal of Advances in*
850 *Modeling Earth Systems*, 11, 2377–2411. <https://doi.org/10.1029/2019MS001629>

851

852 Shupe, M. D., Walden, V. P., Eloranta, E., Uttal, T., Campbell, J. R., Starkweather, S. M., &
853 Shiobara, M. (2011). Clouds at Arctic Atmospheric Observatories. Part I: Occurrence and
854 Macrophysical Properties. *Journal of Applied Meteorology and Climatology*, 50(3), 626–644.
855 <https://doi.org/10.1175/2010JAMC2467.1>

856

857 Silber, I., Verlinde, J., Eloranta, E. W., & Cadetdu, M. (2018). Antarctic cloud macrophysical,
858 thermodynamic phase, and atmospheric inversion coupling properties at McMurdo Station: I.
859 Principal data processing and climatology. *Journal of Geophysical Research: Atmospheres*, 123,
860 6099–6121. <https://doi.org/10.1029/2018JD028279>

861

862 Sun, J., Zhang, K., Wan, H., Ma, P.-L., Tang, Q., & Zhang, S. (2019). Impact of nudging
863 strategy on the climate representativeness and hindcast skill of constrained EAMv1 simulations.

864 *Journal of Advances in Modeling Earth Systems*, 11, 3911– 3933.

865 <https://doi.org/10.1029/2019MS001831>

866

867 Sun, Z. & Shine, K. P. (1994). Studies of the radiative properties of ice and mixed-phase clouds.

868 *Quarterly Journal of the Royal Meteorological Society*, 120, 111–137.

869 <https://doi.org/10.1002/qj.49712051508>

870

871 Sun, Z., & Shine, K. P. (1995). Parameterization of Ice Cloud Radiative Properties and Its

872 Application to the Potential Climatic Importance of Mixed-Phase Clouds. *Journal of Climate*,

873 8(7), 1874-1888. [https://doi.org/10.1175/1520-0442\(1995\)008<1874:POICRP>2.0.CO;2](https://doi.org/10.1175/1520-0442(1995)008<1874:POICRP>2.0.CO;2)

874

875 Tan, I., Barahona, D., & Coopman, Q. (2022). Potential link between ice nucleation and climate

876 model spread in Arctic amplification. *Geophysical Research Letters*, 49, e2021GL097373.

877 <https://doi.org/10.1029/2021GL097373>

878

879 Tan, I., & Storelvmo, T. (2019). Evidence of strong contributions from mixed-phase clouds to

880 Arctic climate change. *Geophysical Research Letters*, 46, 2894–2902.

881 <https://doi.org/10.1029/2018GL081871>

882

883 Tan, I., Storelvmo, T., & Choi, Y.-S. (2014). Spaceborne lidar observations of the ice-nucleating

884 potential of dust, polluted dust and smoke aerosols in mixed-phase clouds. *Journal of*

885 *Geophysical Research: Atmospheres*, 119, 6653–6665, <https://doi.org/10.1002/2013JD021333>

886

887 Tan, I., Storelvmo, T., & Zelinka, M. D. (2016). Observational constraints on mixed-phase
888 clouds imply higher climate sensitivity. *Science*, 352, 224–227.

889 <https://doi.org/10.1126/science.aad5300>

890

891 Tang, Q., Prather, M. J., Hsu, J., Ruiz, D. J., Cameron-Smith, P. J., Xie, S., & Golaz, J.-C.

892 (2021). Evaluation of the interactive stratospheric ozone (O3v2) module in the E3SM version 1

893 Earth system model, *Geoscientific Model Development*, 14, 1219–1236.

894 <https://doi.org/10.5194/gmd-14-1219-2021>

895

896 Verlinde, J., Zak, B. D., Shupe, M. D., Ivey, M. D., & Stamnes, K. (2016). The ARM North

897 Slope of Alaska (NSA) Sites. *Meteorological Monographs*, 57, 8.1-

898 8.13. <https://doi.org/10.1175/AMSMONOGRAPHS-D-15-0023.1>

899

900 Villanueva, D., Senf, F., & Tegen, I. (2021). Hemispheric and seasonal contrast in cloud

901 thermodynamic phase from A-Train spaceborne instruments. *Journal of Geophysical Research:*

902 *Atmospheres*, 126, e2020JD034322. <https://doi.org/10.1029/2020JD034322>

903

904 Wang, H., Easter, R. C., Zhang, R., Ma, P.-L., Singh, B., Zhang, K., et al. (2020). Aerosols in the

905 E3SM Version 1: New developments and their impacts on radiative forcing. *Journal of Advances*

906 *in Modeling Earth Systems*, 12, e2019MS001851. <https://doi.org/10.1029/2019MS001851>

907

- 908 Wang, Y., Liu, X., Hoose, C., & Wang, B. (2014). Different contact angle distributions for
909 heterogeneous ice nucleation in the Community Atmospheric Model version 5. *Atmospheric*
910 *Chemistry and Physics*, 14, 10411–10430. <https://doi.org/10.5194/acp-14-10411-2014>
911
- 912 Xie, S., Klein, S. A., Yio, J. J., Beljaars, A. C. M., Long, C. N., & Zhang, M. (2006). An
913 assessment of ECMWF analyses and model forecasts over the North Slope of Alaska using
914 observations from the ARM Mixed-Phase Arctic Cloud Experiment. *Journal of Geophysical*
915 *Research: Atmospheres*. 111, D05107. <https://doi.org/10.1029/2005JD006509>
916
- 917 Xie, S., Lin, W., Rasch, P. J., Ma, P.-L., Neale, R., Larson, V. E., et al. (2018). Understanding
918 cloud and convective characteristics in version 1 of the E3SM atmosphere model. *Journal of*
919 *Advances in Modeling Earth Systems*, 10, 2618–2644. <https://doi.org/10.1029/2018MS001350>
920
- 921 Xie, S., McCoy, R. B., Klein, S. A., Cederwall, R. T., Wiscombe, W. J., Jensen, M. P., et al.
922 (2010). CLOUDS AND MORE: ARM Climate Modeling Best Estimate Data. *Bulletin of the*
923 *American Meteorological Society*, 91(1), 13–20. <https://doi.org/10.1175/2009BAMS2891.1>
924
- 925 Xie, S., Wang, Y.-C., Lin, W., Ma, H.-Y., Tang, Q., Tang, S., et al. (2019). Improved diurnal
926 cycle of precipitation in E3SM with a revised convective triggering function. *Journal of*
927 *Advances in Modeling Earth Systems*, 11. <https://doi.org/10.1029/2019MS001702>
928
- 929 Yang, C. A., Diao, M., Gettelman, A., Zhang, K., Sun, J., McFarquhar, G., & Wu, W. (2021). Ice
930 and supercooled liquid water distributions over the Southern Ocean based on in situ observations

931 and climate model simulations. *Journal of Geophysical Research: Atmospheres*, 126,
932 e2021JD036045. <https://doi.org/10.1029/2021JD036045>
933
934 Yip, J., Diao, M., Barone, T., Silber, I., & Gettelman, A. (2021). Evaluation of the CAM6
935 climate model using cloud observations at McMurdo Station, Antarctica. *Journal of Geophysical*
936 *Research: Atmospheres*, 126, e2021JD034653. <https://doi.org/10.1029/2021JD034653>
937
938 Zelinka, M. D., Myers, T. A., McCoy, D. T., Po-Chedley, S., Caldwell, P. M., Ceppi, P., et al.
939 (2020). Causes of higher climate sensitivity in CMIP6 models. *Geophysical Research Letters*,
940 47, e2019GL085782. <https://doi.org/10.1029/2019GL085782>
941
942 Zhang, C., Xie, S., Tao, C., Tang, S., Emmenegger, T., Neelin, J. D., et al. (2020). The ARM
943 Data-Oriented Metrics and Diagnostics Package for Climate Models: A New Tool for Evaluating
944 Climate Models with Field Data, *Bulletin of the American Meteorological Society*, 101(10),
945 E1619-E1627. <https://doi.org/10.1175/BAMS-D-19-0282.1>
946
947 Zhang, D., Wang, Z., Kollias, P., Vogelmann, A. M., Yang, K., & Luo, T. (2018). Ice particle
948 production in mid-level stratiform mixed-phase clouds observed with collocated A-Train
949 measurements. *Atmospheric Chemistry and Physics*, 18, 4317–4327. [https://doi.org/10.5194/acp-](https://doi.org/10.5194/acp-18-4317-2018)
950 [18-4317-2018](https://doi.org/10.5194/acp-18-4317-2018)
951
952 Zhang, D., Vogelmann, A., Kollias, P., Luke, E., Yang, F., Lubin, D., & Wang, Z. (2019).
953 Comparison of Antarctic and Arctic single-layer stratiform mixed-phase cloud properties using

954 ground-based remote sensing measurements. *Journal of Geophysical Research: Atmospheres*,
955 124. <https://doi.org/10.1029/2019JD030673>

956

957 Zhang, G. J., & McFarlane, N. A. (1995). Sensitivity of climate simulations to the
958 parameterization of cumulus convection in the Canadian climate centre general circulation
959 model. *Atmosphere-Ocean*, 33(3), 407–446. <https://doi.org/10.1080/07055900.1995.9649539>

960

961 Zhang, K., Wan, H., Liu, X., Ghan, S. J., Kooperman, G. J., Ma, P.-L., et al. (2014). Technical
962 Note: On the use of nudging for aerosol–climate model intercomparison studies. *Atmospheric*
963 *Chemistry and Physics*, 14, 8631–8645. <https://doi.org/10.5194/acp-14-8631-2014>

964

965 Zhang, K., Zhang, W., Wan, H., Rasch, P. J., Ghan, S. J., Easter, R. C., et al. (2022). Effective
966 radiative forcing of anthropogenic aerosols in E3SM version 1: historical changes, causality,
967 decomposition, and parameterization sensitivities. *Atmospheric Chemistry and Physics*, 22,
968 9129–9160. <https://doi.org/10.5194/acp-22-9129-2022>

969

970 Zhang, M., Xie, S., Liu, X., Lin, W., Zhang, K., Ma, H.-Y., et al. (2020). Toward understanding
971 the simulated phase partitioning of arctic single-layer mixed-phase clouds in E3SM. *Earth and*
972 *Space Science*, 7, e2020EA001125. <https://doi.org/10.1029/2020EA001125>

973

974 Zhang, M., Xie, S., Liu, X., Lin, W., Zheng, X., Golaz, J.-C., & Zhang, Y. (2022). Cloud Phase
975 Simulation at High Latitudes in EAMv2: Evaluation using CALIPSO Observations and

976 Comparison with EAMv1. *Journal of Geophysical Research: Atmospheres*, 127,
977 e2022JD037100. <https://doi.org/10.1029/2022JD037100>

978

979 Zhang, Y., Xie, S., Lin, W., Klein, S. A., Zelinka, M., Ma, P.-L., et al. (2019). Evaluation of
980 clouds in version 1 of the E3SM atmosphere model with satellite simulators. *Journal of*
981 *Advances in Modeling Earth Systems*, 11. <https://doi.org/10.1029/2018MS001562>

982

983 Zhao, C., Xie, S., Klein, S. A., Protat, A., Shupe, M. D., McFarlane, S. A., et al. (2012). Toward
984 understanding of differences in current cloud retrievals of ARM ground-based measurements.
985 *Journal of Geophysical Research: Atmospheres*, 117, D10206.

986 <https://doi.org/10.1029/2011JD016792>

987

988 Zhao, X., & Liu, X. (2021). Global importance of secondary ice production. *Geophysical*
989 *Research Letters*, 48, e2021GL092581. <https://doi.org/10.1029/2021GL092581>

990

991 Zhao, X., & Liu, X. (2022). Primary and secondary ice production: interactions and their relative
992 importance. *Atmospheric Chemistry and Physics*, 22, 2585–2600. [https://doi.org/10.5194/acp-22-](https://doi.org/10.5194/acp-22-2585-2022)
993 [2585-2022](https://doi.org/10.5194/acp-22-2585-2022)

994

995 Zhao, X., Liu, X., Phillips, V. T. J., & Patade, S. (2021). Impacts of secondary ice production on
996 Arctic mixed-phase clouds based on ARM observations and CAM6 single-column model
997 simulations. *Atmospheric Chemistry and Physics*, 21, 5685–5703. [https://doi.org/10.5194/acp-](https://doi.org/10.5194/acp-21-5685-2021)
998 [21-5685-2021](https://doi.org/10.5194/acp-21-5685-2021)

